Department of Physics and Astronomy
University of Heidelberg

Master Thesis in Physics
submitted by

Sebastian Pres

born in Fritzlar

2014

BKT - phase transition in a strongly interacting 2d Bose gas

This Master Thesis has been carried out by Sebastian Pres at the
Physikalisches Institut Heidelberg
under the supervision of
Prof. Selim Jochim

Abstract

In this thesis we probe the transition from a normal to a quasi-condensate phase in a two dimensional gas of ultracold bosonic dimers in the regime of strong interactions.
We prepare a quantum degenerate sample of deeply bound molecules consisting of two ^{6}Li fermions in the two lowest hyperfine sublevels by performing evaporative cooling in a 3d optical dipole trap and subsequently transferring the cloud into a standing wave optical dipole trap. The standing wave trap creates a stack of highly anisotropic potentials with a tight vertical confinement. By tomographic radio-frequency spectroscopy we resolve the population in the individual layers of the standing wave trap. By precise control of the Fermi energy and the temperature we freeze out the vertical degree of freedom and prepare a quasi-2d system in a single standing wave trap.
By investigating the density distribution after short time-of-flight we observe density fluctuations in the quasi-condensate part which we relate to an in-situ phase fluctuation. This is a significant indication for an initial quasi long range order in the sample predicted for the BKT phase. After long time-of-flight we directly obtain the in-situ radial momentum distribution by using a matter wave focusing technique. Due to the clear bimodal profile of the momentum distribution we successfully isolated the normal and the quasi-condensate part. This allows us to determine the critical temperature of the phase transition by extracting the quasi-condensate fraction at different temperatures.

Zusammenfassung

In dieser Arbeit untersuchen wir den Phasenübergang zwischen einer normalen Phase und einer quasi-kondensierten Phase in einem zwei-dimensionalen Gas bestehend aus ultrakalten, stark wechselwirkenden, bosonischen Dimeren.
Durch evaporatives Kühlen in einer 3d optischen Dipolfalle preparieren wir hierbei ein quantenentartetes System von tief gebundenen Molekülen, die aus zwei ^{6}Li Fermionen in den untersten zwei Hyperfineunterzuständen bestehen. Dieses System transferieren wir direkt in eine weitere vertikale Anordnung mehrerer optischer Dipolfallen, welche durch eine stehenden Welle erzeugt werden. Die besonders anisotropen optischen Potentiale erlauben es die Moleküle in vertikaler Richtung besonders stark einzuschränken. Die Besetzungsverteilung in den einzelnen optischen Potentialen können wir durch eine tomographische Radio-Frequenz-Spektroskopie bestimmen. Das Ausfrieren des vertikalen Freiheitsgrades gelingt uns durch eine präzise Einstellung der Fermi Energie und der Temperatur und erlaubt uns ein quasi-zwei dimensionales System in einem einzigen optischen Dipolpotential zu generieren.
Bei der Messung der Dichteverteilung nach kurzer Expansion der Wolke beobachten wir Dichtefluktuationen im quasi-kondensierten Teil, welche wir auf in-situ Phasenfluktuationen zurückführen. Dieses ist ein starker Hinweis für eine ursprüngliche quasi-langreichweitige Ordnung in dem System, die für die BKT-Phase vorausgesagt wird. Nach langer Expansion der Wolke gelingt es uns die in-situ Impulsverteilung der Moleküle zu bestimmen, indem wir eine Materiewellen Fokussiertechnik anwenden. Durch das eindeutig bimodale Profil der Impulsverteilung, können wir erfolgreich den quasi-kondensierten Anteil vom normalen Anteil isolieren. Dies erlaubt uns eine Bestimmung der kritischen Temperatur des Phasenübergangs, indem wir den quasi-kondensierten Anteil bei unterschiedlichen Temperaturen messen.

Contents

1. Introduction

The physical properties of a many-body-system are strongly influenced by its ordering. During a phase transition the ordering of the many-body system is changed qualitatively which can be observed in typical phase transitions in our three dimensional world like freezing of water or ferromagnetism. All these phase transitions can be characterized by a spontaneously breaking of some continuous symmetry of the Hamiltonian. Frozen water for instance can be characterized by a spontaneously broken translational symmetry due to crystallization.
The phase transition from a thermal phase to a Bose-Einstein condensate is indicated by the emergence of a true long range order in the system. Reducing the dimensions of the many-body-system from 3d to 2d affects the nature of the phase transition. The Mermin-Wagner theorem states that continuous symmetries cannot be spontaneously broken in two or one dimensional systems at finite temperature. As a consequence true long range order does not exist except for zero temperature [Mer66].
Thus, the observed phase transitions in two dimensional systems like for instance the appearance of superfluidity in thin ^{4}He films [Bis78], has to be related to a different class of phase transitions. The most famous example of a continuous but not symmetry breaking phase transition is the Berezinksii-Kosterlitz Thouless (BKT) transition [Ber71, Kos73], which only exists in 2d and is also believed to be relevant in high-T_c superconductivity [Squ11].
The BKT phase is characterized by a topological order of the system due to pairing of vortices with opposite circulations, which leads to a quasi long range order. Since quasi long range order can be established in two dimensions for sufficiently low temperatures, this enables the possibility of a superfluid phase transition.
A convenient system to study the BKT-transition are quantum gases of ultracold atoms since they are completely decoupled from the environment, allow to control the internal and external states of the trapped particles and provide a convenient accessibility by imaging techniques. By confining ultracold quantum gases to highly anisotropic optical dipole potentials [Gri00], the dimensionality of the trapped system can be reduced. This enables the investigation of the length scale of the order in two or one dimensional systems and opens the possibility to study the underlying concept of superfluidity in reduced dimensions.
Ultracold quantum gases have been available since the first realization of a BEC in 1995 [And95, Dav95] and the first preparation of a degenerate Fermi gas in 1999 [DeM99]. Due to the existence of Feshbach resonances [Ino98, Chi10], the interactions in the sample can be tuned and thus a highly correlated many-body-system can be realized. Besides that, the tuneability of interactions during the evaporative cooling allows the

formation of bosonic dimers formed by two strongly repulsive interacting fermionic atoms.
In 3d these Feshbach molecules can perform a phase transition into a molecular BEC which was shown in [Joc03, Gre03, Zwi03]. By changing the repulsive interaction of the condensed molecules to the regime of attractive interactions a superfluid consisting of Cooper pairs can be formed as described by BCS theory. The repulsive interacting regime (BEC side) and the weakly attractive interacting Fermi gas regime (BCS side) are continuously connected by a strongly interacting regime known as the BEC-BCS crossover. The first observation of a phase transition from a normal to a superfluid phase of fermionic pairs on the BCS side was achieved by [Gre03, Zwi03] and could be extended to the BEC-BCS crossover in [Zwi05].
Since in two dimensional systems Bose-Einstein condensation is strongly suppressed, we study in this thesis the emergence of the BKT transition in the bosonic regime.
The first experimental observation of the BKT transition in ultracold quantum gases was achieved by probing the coherence of a 2d bosonic system of ^{87}Rb by [Had06] using matter wave heterodyning and the validation of the superfluid character of a 2d Bose gas was obtained by a stirring experiment in [Des12].
Probing of a strongly interacting quasi-2d Fermi gas was achieved by different experimental methods. The interaction energy and the confinement induced resonance were measured by radio frequency spectroscopy [Frö11b]. Further investigations have been obtained concerning the pairing properties during the phase transition by momentum resolved photo-emission spectroscopy [Fel11]. However, so far all quasi-2d Fermi gas experiments could observe neither the superfluid behavior nor the BKT phase.
In this thesis we investigate the nature of this phase transition for a quasi-2d two component Fermi gas in the strongly interacting bosonic regime.

Outline

This master thesis is structured as follows: In the second chapter we introduce the basic theoretical background of ultracold fermionic and bosonic quantum gases in three dimensions. Therefore we briefly discuss their collective behavior in a harmonic trap and the concept of tuning the interactions via Feshbach resonances. Further we give an overview over the basic properties of our species ^{6}Li and close this chapter summarizing the different regimes of the 3d BEC-BCS crossover.
The third chapter presents a brief theoretical introduction to quantum gases in two dimensions. We focus on the differences of the quantum statistics and the scattering properties compared to the three dimensional case and close this chapter with a description of the mechanisms and characteristics of the Berezinskii-Kosterlitz-Thouless (BKT) transition.
Chapter 4 describes the different components of our experimental setup to prepare a quasi-2d strongly interacting Fermi gas and gives a short introduction to the theoretical description of optical dipole trapping. Further we discuss the preparation of the quasi-2d sample and will describe the techniques and achievements to validate the 2d-ness of

the system in Chapter 5.
In Chapter 6 we present our obtained measurement results of a quasi-2d Fermi gas in the bosonic strongly interacting regime. We investigated the density distribution of a sample after short time-of-flight and developed a matter wave focusing technique to image the in-situ momentum distribution of the quasi-2d system. From both measurements we achieved significant evidence of the occurrence of a phase transition and strong indications that this phase transition is described by the BKT theory.
We close this thesis by a summary of the most important results and give a short outlook on the future projects we hope to achieve.

2. Theory of ultracold quantum gases in 3d

This chapter provides a brief introduction to the theoretical background of ultracold quantum gases in three dimensions. In Section 2.1 we explain the different quantum statistics of bosonic and fermionic particles. Since the information we extract from our measurements are mainly based on the density distribution of ultracold atomic samples, we will examine in Section 2.2 the density distribution in a harmonic trap for a non-interacting gas and study the effect of temperature and interaction. Furthermore, Section 2.3 introduces the concept of ultracold scattering which can be described by a single effective parameter, the s-wave scattering length. In addition the concept of tuning the interaction via a magnetic Feshbach resonance and its implications for the special case of ^{6}Li will be discussed. Finally, in Section 2.4 we focus on interacting fermions and the BEC-BCS crossover respectively.

2.1. Quantum Statistics of Fermions and Bosons

The fundamental difference between fermions and bosons becomes first visible by entering the quantum regime. This transition takes place at the point where the distinguishability of particles is not longer guaranteed. Due to the wave-particle duality one can associate a wavelength to each particle $\lambda_{dB} = h/p$ [Bro23] ,where h is Planck's constant and p the particle momentum. Since we investigate particles in a gas at a given temperature T we obtain the thermal de Broglie wavelength

$$\lambda_{th} = \frac{h}{\sqrt{2\pi m k_B T}}, \tag{2.1}$$

with m equal to the mass of the particle and k_B corresponds to the Boltzmann constant. If λ_{th}, which can be related to the width of the wave function, gets comparable to the inter-particle spacing $d \sim n^{-1/3}$ at a fixed density n, the wave function between different particles start to overlap and they become indistinguishable. The transition can be either reached by decreasing the temperature or increasing the density of the system and as we will see later, we will focus on cooling the quantum gas down to the mK - nK regime.
One consequence of indistinguishabilty is, that the probability density, i.e. the modulus square of the many-particle wave function $|\Psi(x_1, \ldots, x_N)|^2$ has to be invariant under particle exchange, where N is the number of indistinguishable particles and the

x_i represent each spatial coordinate and the discrete quantum numbers. This leads to two possibilities for the many-particle wave function. It has to transform either symmetrically or anti-symmetrically under particle exchange. The spin-statistics-theorem connects the symmetry of the wave function to the spin of the particle and so bosons (integer spin) are defined as having a symmetric wave function and fermions (half integer spin) are defined as having an anti-symmetric wave function.
One crucial effect for fermions is that, due to the anti-symmetry of the wave function, two particles cannot occupy the same single-particle quantum state, since $\Psi(x_i, x_i) = -\Psi(x_i, x_i)$ has only a solution for a vanishing wave function. This is know as Pauli's exclusion principle [Pau25]. In contrast, bosons are allowed to occupy the same single-particle state, which leads to a completely different formation of the many-particle ground state in a harmonic trap as seen in Figure 2.1.
For a non-interacting system at $T = 0$ the bosonic many-particle ground state is the single-particle ground state of the harmonic oscillator and the particles form a Bose-Einstein-Condensate (BEC), which is a special quantum state, since all particles can be described by just one macroscopic wave function. Moreover, even for $T_c > T > 0$ the probability of finding a particle in the single-particle ground state is significantly enhanced compared with the probability of finding a particle in one of the excited single-particle states.
On the other hand, fermions will form a so-called Fermi sea which describes the fermionic many-particle ground state at $T = 0$, due to Pauli's exclusion principle each fermion has to occupy a different single-particle state up to a characteristic energy called Fermi energy E_F. As we will see later in this thesis we are dealing with about $10^4 - 10^5$ particles in our experiments. This leads to a statistical description of our system and opens the door to thermodynamic quantities. We will use the grand canonical ensemble to describe our ultracold system, where the macroscopic variables are given by the temperature T, the chemical potential μ, which corresponds to the energy necessary to add a particle to the system and the volume V.
A detailed derivation of the grand canonical partition function Z_G for non-interacting fermions and bosons can be found in [Pet02] and the result is given by

$$Z_{\text{bosonic}} = \prod_i \frac{1}{1 - e^{-\beta(E_i - \mu)}} \quad \text{and} \quad Z_{\text{fermionic}} = \prod_i \left(1 + e^{-\beta(E_i - \mu)}\right), \tag{2.2}$$

with $\beta = 1/(k_B T)$. The relation of the total atom number N to the grand canonical potential $\Omega(T, V, \mu) = -k_B T \ln Z_G$ can be written as

$$N = \sum_i \langle n_i \rangle = -\left(\frac{\partial \Omega}{\partial \mu}\right)_{T,V}. \tag{2.3}$$

This leads to the well known Bose-Einstein and Fermi-Dirac distributions, which describe the mean occupation number of a non-interacting system of particles in the i-th

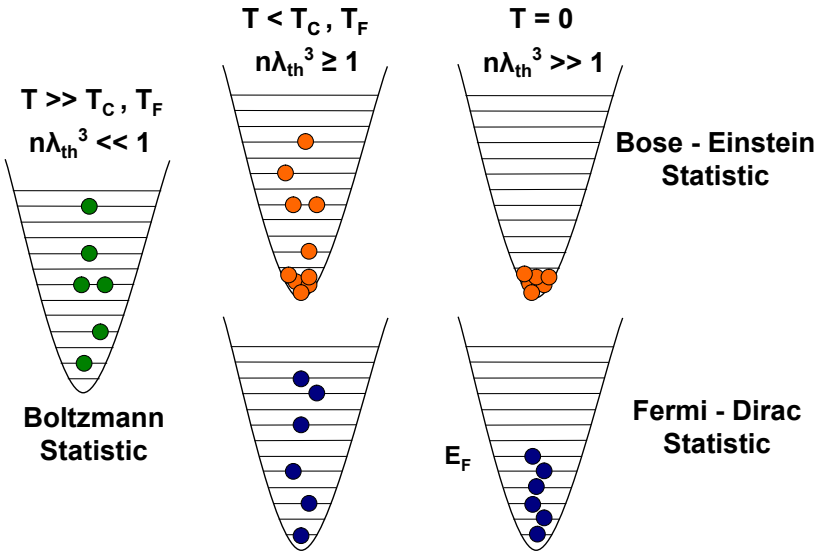

Figure 2.1.: **Illustration of the occupation difference of fermions and bosons in the corresponding temperature regimes.** For $T = 0$ bosons occupy the single-particle ground state macroscopically whereas fermions due to Pauli's principle fill up the potential up to the Fermi energy E_F which leads to the Fermi pressure and to incompressibility of a fermionic quantum gas. Furthermore is the phase space density $D_{3D} = n\lambda_{th}^3$ for each regime depicted. The picture is adapted from [Dyk10].

quantum state and are given by[1]

$$n_{\text{bosonic}}(\epsilon) = \langle n_i \rangle_{\text{bosonic}} = \frac{1}{e^{\beta(E_i-\mu)} - 1} \tag{2.4}$$

$$n_{\text{fermionic}}(\epsilon) = \langle n_i \rangle_{\text{fermionic}} = \frac{1}{e^{\beta(E_i-\mu)} + 1}. \tag{2.5}$$

Based on this equations we can now proceed to calculate the density distribution of the atomic gas.

2.2. Density distribution in a harmonic trap

During the experiments discussed in this work we will trap the atoms in optical potentials which can be well approximated to be harmonic as long as the atoms populate only the low energy levels of the potential. Hence, we can define our 3D trapping potential

[1] $\epsilon = E_i$ just for simplicity.

as

$$V(x,y,z) = \sum_{i=x,y,z} \left(\frac{1}{2} m\omega_i^2 i^2 \right), \tag{2.6}$$

where m is the atomic mass and ω_i is the trapping frequency along the corresponding axis.
The density of states in a d-dimensional trap is defined by the confining potential and can be written in the general form [Dyk10]

$$g(\epsilon) = \frac{\epsilon^{d-1}}{(d-1)! \prod_{i=1}^{d} \hbar\omega_i}, \tag{2.7}$$

which leads for the three dimensional harmonic oscillator to

$$g(\epsilon) = \frac{\epsilon^2}{2(\hbar\bar{\omega})^3}, \tag{2.8}$$

with $\bar{\omega} = (\omega_x\omega_y\omega_z)^{1/3}$. The total number of atoms is given by the summation over all energy states

$$N = \sum_{\epsilon} n(\epsilon)\, g(\epsilon). \tag{2.9}$$

To calculate N we assume further that $k_B T \gg \hbar\omega_i$ so that the sum over the discrete energy states can be written as an integral. A more elaborate calculation by explicit integration over the phase space can be found in [Wen13].

2.2.1. Non-interacting degenerate Fermi gas

The calculation follows the one in [Dyk10]. The Fermi energy E_F of a system of N identical, non-interacting trapped fermions is given by the chemical potential μ at $T = 0$. At this point Equation 2.5 becomes a step function which is one for $E < E_F$ and zero else. Performing the integration of Equation 2.9 up to E_F leads to

$$E_F = \hbar\bar{\omega}(6N)^{1/3} = k_B T_F, \tag{2.10}$$

where T_F is the Fermi temperature. To calculate the density distribution at $T = 0$ we use the local density approximation (LDA) $E_F(\mathbf{r}) = E_F - V(\mathbf{r})$ which assumes, that the sample can be approximated by a uniform gas at any location $\mathbf{r}$. Now we can define a local Fermi wave vector $k_F(\mathbf{r})$ via

$$E_F(\mathbf{r}) = \frac{\hbar^2 k_F(\mathbf{r})^2}{2m}. \tag{2.11}$$

The local density is now given as the number of atoms that fill up the momentum sphere with radius $\hbar k_F(\mathbf{r})$

$$n_F(\mathbf{r}) = \frac{4}{3}\pi \left(\hbar k_F(\mathbf{r})\right)^3 \frac{1}{(2\pi\hbar)^2}, \tag{2.12}$$

and finally we end up with

$$n_F(\mathbf{r}, T=0) = \frac{1}{6\pi^2}\left(\frac{2m}{\hbar^2}\left(E_F - V(\mathbf{r})\right)\right)^{3/2}. \tag{2.13}$$

The maximum cloud size $r_{i,F}$, called the Fermi radius, is given at $V(r_{i,F}) = E_F$ with $i = x, y, z$ which leads for a harmonic potential to

$$r_{i,F} = \sqrt{\frac{2k_B T_F}{m\omega_i^2}} \quad \text{and} \quad r_{i,F} = \sqrt{\frac{\hbar}{m\bar{\omega}_i}}\,(48N)^{1/6}\,\frac{\bar{\omega}}{\omega_i}. \tag{2.14}$$

Hence the density distribution for $T = 0$ becomes

$$n_F(\mathbf{r}, T=0) = \frac{8\,N}{\pi^2 x_F y_F z_F}\left(1 - \sum_{i=x,y,z}\frac{i^2}{r_{i,F}^2}\right)^{3/2}. \tag{2.15}$$

2.2.2. Non-interacting degenerate Fermi gas at non-zero temperature

The problem of finding the density distribution for a non-interacting Fermi gas at $T > 0$ is, that the chemical potential μ cannot be expressed explicitly. Nevertheless, one can express the density in terms of the polylogarithmic function $\mathrm{Li}_\nu(\mathbf{z})$ defined in [Wei09] and by fulfilling the normalization condition in Equation 2.9 one can find an implicit definition of μ in terms of T/T_F. In [Wen13] this equation has been solved numerically and compared to a Gaussian fit. For $T/T_F \gtrsim 0.5$ the Gaussian fit gives still reasonable results whereas for $T/T_F \ll 0.5$ the density distribution peak is more flattened. Than the Gaussian distribution and the wings are steeper. So the Gaussian fit is not longer sufficient and one has to use the numerical Fermi fit.

2.2.3. Non-interacting degenerate Bose gas

Since for bosons the mean occupation distribution is given by Equation 2.4 and the 3D density of states is well known, we can calculate the mean atom number using Equation 2.9. The mean occupation distribution cannot be negative for each i which implies $E_i - \mu > 0$ and by setting the ground state energy $E_0 = 0$ we can follow that $\mu \leq 0$. We already know, that for $T = 0$ the ground state is macroscopically populated, a phenomenon called Bose-Einstein condensation, so it makes sense to treat the ground state separately in the sum. By transforming the sum to an integral we

obtain the following equation for the number of particles [Pet02]

$$N - N_c = \left(\frac{k_B T}{\hbar\bar{\omega}}\right)^3 \mathrm{Li}_3\left(\exp\left\{\frac{\mu}{k_B T}\right\}\right), \tag{2.16}$$

where N corresponds to the total number of particles and N_c describes the particles condensed in the ground state. The transition temperature T_c can be calculated by setting μ and N_c to zero which results in

$$k_B T_c = \hbar\bar{\omega}\left(\frac{N}{\mathrm{Li}_3(1)}\right)^{1/3} \approx 0.94\,\hbar\bar{\omega}\,N^{1/3}, \tag{2.17}$$

where $\mathrm{Li}_3(1) \approx 1.202$ was used. With Equation 2.16 and the fact that $\mu = 0$ below T_c one gains the fraction of condensed particles at a given temperature T as

$$\frac{N_c}{N} = 1 - \left(\frac{T}{T_c}\right)^3. \tag{2.18}$$

The density distribution of the condensed part can then be approximated by the ground state wave function of a three dimensional harmonic oscillator [Dyk10]

$$\psi_0(r) = \left(\frac{m\bar{\omega}}{\pi\hbar}\right) \exp\left(-\frac{m}{2\hbar}\sum_{i=x,y,z}\omega_i i^2\right). \tag{2.19}$$

From here we can see that the density $n(r) = N|\psi(r)|^2$ will increase with N whereas the condensate size is fixed by the harmonic oscillator length

$$l_{ho} = \sqrt{\frac{\hbar}{m\bar{\omega}}} \tag{2.20}$$

For $T > T_c$ the width of the density distribution can be obtained from classical gas statistics [Pet02]

$$r_{i,thermal} = \sqrt{\frac{2k_B T}{m\omega_i^2}}. \tag{2.21}$$

Since $r_{i,thermal} \gg l_{ho}$ the BEC will be visible as a narrow peak in the spatial and momentum distribution if $T < T_c$. In contrast to fermionic quantum gases, where the formation of the Fermi sea is continuous, the behavior of a bosonic gas is changed abruptly when reaching quantum degeneracy.

2.2.4. Interacting Bose gas

A detailed theoretical description of an interacting bosonic gas can be found e.g. in [Dal99]. Thus, we will just discuss the most important steps to derive the density

profile of interacting bosons in a harmonic trap.
Starting from the well known stationary Gross-Pitaevskii equation [Gro61, Pit61]

$$\mu\psi(\mathbf{r},t) = \left(-\frac{\hbar^2}{2m}\nabla^2 + V_{trap}(\mathbf{r}) + Ng|\psi(\mathbf{r})|^2\right)\psi(\mathbf{r},t), \tag{2.22}$$

one can calculate the density distribution given by $n(\mathbf{r},t) = N|\psi(\mathbf{r},t)|^2$. Since $N \gg 1$ and by assuming just repulsive interactions $g > 0$, we can neglect the kinetic energy term and the stationary Gross-Pitaevskii equation becomes a simple algebraic equation. This approximation is known as the Thomas-Fermi limit and we obtain the following inverted parabola equation for the density in a 3D harmonic potential

$$n(r) = \frac{\mu - m\bar{\omega}^2 r^2}{g}, \tag{2.23}$$

which maximum value is μ/g at $r = 0$ and which vanishes for $r \geq r_{TF} = (2\mu/m\bar{\omega}^2)^{1/2}$ where r_{TF} is the so-called Thomas-Fermi radius. From the normalization condition in Equation 2.9 one finds

$$\mu(N) = \frac{\hbar\bar{\omega}}{2}\left(\frac{15Na}{l_{ho}}\right)^{2/5}. \tag{2.24}$$

Since μ is now a function of N, r_{TF} depends on N as well and we can follow

$$r_{i,TF}(N) = l_{ho}\frac{\bar{\omega}}{\omega_i}\left(\frac{15Na}{l_{ho}}\right)^{1/5} \tag{2.25}$$

where $i = x, y, z$. Comparing this result to the non-interacting case for a cylindrically-symmetric harmonic trap

$$V(z,r) = \frac{1}{2}m(\omega_z^2 z^2 + \omega_\perp^2 r^2), \tag{2.26}$$

one finds the limitation of the density profile in axial direction by $m\omega_z^2 z_{max}^2 = 2\mu$ and radially $m\omega_\perp^2 r_{max}^2 = 2\mu$. Thus, the aspect ration of the condensate is given by $z_{max}/r_{max} = \omega_\perp/\omega_z$, whereas in the non-interacting case this ratio is equal to the ratio of the corresponding harmonic oscillator lengths in each axis which are just $\sim \sqrt{\omega_{z,\perp}}$. So one can deduce, that the interaction results in a magnification of the aspect ratio of the condensate.

2.3. Ultracold Interactions

The purpose of this section is to give a brief introduction to the necessary concepts to describe the interactions in a dilute atomic gas. Typical densities of ultracold atomic

systems are on the order of $n = (10^{12}-10^{15})\text{cm}^{-3}$ since at lower densities elastic collision rates are to small to cool efficiently and at higher densities atomic losses increase due to the dominance of three body loss processes [Ket99]. In general the length scale on which interactions between neutral atoms take place is given by the short-ranged van-der-Waals potential, which scales as r^{-6} and has a finite range known as the van-der-Waals radius r_{vdW}. As pointed out in Section 2.1, to reach quantum degeneracy one has to fulfill $n\lambda_{dB}^3 \gtrsim 1$ which is typically achieved at temperatures between $100\text{nK} - 50\mu\text{K}$. Thus, as λ_{dB} is on the order of 1μm and the range of interaction r_0 is given by the van-der-Waals radius $r_{vdW,Li} \sim 0.2$nm [Bon64], the inequality $\lambda_{dB}, n^{-1/3} \gg r_{vdW}$ holds and the particles only interact via two-body collisions which are well described by a single parameter the s-wave scattering length a. Here $n^{-1/3}$ corresponds to the interparticle spacing. In Section 2.3.3 we will show, that this single parameter a can be tuned by a magnetic offset field and thus allows us to tune the interaction between the particles over a wide range.

2.3.1. Ultracold scattering in 3d

The derivation of the s-wave scattering length has been discussed in many textbooks on quantum mechanics and quantum collisions e.g. [Sak94, Bra03]. The next section will thus summarize the most important steps and results of the derivation.
In quantum mechanics elastic two-body scattering can be described by the time-independent Schrödinger equation

$$\left[-\frac{\hbar^2}{2m}\nabla^2 + V(\mathbf{r})\right]\psi(\mathbf{r}) = E\psi(\mathbf{r}), \tag{2.27}$$

with the relative coordinates $\mathbf{r} = \mathbf{r}_1 - \mathbf{r}_2$ and the reduced mass of the particles $m = \frac{m_1 m_2}{m_1+m_2}$. $V(\mathbf{r})$ is the two-particle interaction potential which is assumed to be spherically symmetric and decreasing with $1/r^i$, $i > 1$. In the long-distance limit $r \to \infty$ the wave function $\psi(\mathbf{r})$ satisfies the free-particle Schrödinger equation and can be written as a sum of an incoming plane wave e^{ikz} and an outgoing spherical wave $\frac{e^{ikr}}{r}$ with momentum k along the z-axis as follows

$$\psi_k(\mathbf{r}) \propto e^{ikz} + f(k,\theta)\frac{e^{ikr}}{r}. \tag{2.28}$$

$f(k,\theta)$ corresponds to the scattering amplitude and is due to symmetry reasons independent of φ. Since the relative distance $|\mathbf{r}|$ given by $n^{-1/3}$ in the experiment is much larger than r_{vdW} the large distance limit reflects the condition in ultracold gases quite well. The differential and total cross-section are related to the scattering amplitude by the following equations

$$\frac{d\sigma}{d\Omega} = |f(k,\theta)|^2 \quad \text{and} \quad \sigma_{\text{tot}} = \int_\Omega |f(k,\theta)|^2 \, d\Omega, \quad \text{where} \quad 0 \le \theta < \pi. \tag{2.29}$$

All the relevant information is contained in the scattering amplitude which can be calculated by expanding the ingoing and outgoing parts of the wave function into the spherical-wave basis with angular momenta l

$$\psi(\mathbf{r}) = \sum_{l=0}^{\infty} \sum_{m=-l}^{m=l} Y_l^m(\theta, \varphi) \frac{\chi_{k,l,m}(r)}{r}. \tag{2.30}$$

Due to the spherical symmetry of the system m turns out to be equal to zero and the spherical harmonics can be written in terms of Legendre polynomials $Y_l^0(\theta, \varphi) \rightarrow P_l(cos(\theta))$ which are just dependent on θ. Inserting this expansion into the Schrödinger equation leads to an effective one-dimensional Schrödinger equation for each radial wave function $\chi_{k,l,m}(r)$

$$\left[\frac{d^2}{dr^2} - \frac{2m}{\hbar^2}\left(V(r) + \frac{\hbar^2 l(l+1)}{2m_{red}r^2}\right) + k^2\right] \chi_{k,l}(r) = 0. \tag{2.31}$$

The term depending on the angular momentum l in Equation 2.31 can be related to the centrifugal barrier, which inhibits scattering for $l > 0$ in the regime of small scattering energies $k \rightarrow 0$. Thus, a particle with a relative energy less than the barrier height does not feel the short distance details of the interacting potential since it is just reflected by the centrifugal barrier. As the centrifugal barrier for ^{6}Li is on the order of 7mK [Fuc09], collisions in the temperature regime $T \ll 7$mK only occur due to isotropic s-wave scattering ($l = 0$).
By investigating the asymptotic behavior of the ingoing and outgoing wave in the large distance limit one can deduce, that the only effect of an elastic collisions on the wave function is a phase δ_l in each spherical wave. Hence, the scattering amplitude can be written in terms of these phase shifts [Sak94]. For low momenta ($k \rightarrow 0$) only the phase δ_0 contributes, which can be well seen in a classical example. Let us assume a particle with momentum p and impact parameter α is interacting with a potential with interaction range r_0. The angular momentum can be written as $|\mathbf{r} \times \mathbf{p}| = p\alpha$ with a partial wave number $l = p\alpha/\hbar$. If the closest distance α is smaller than r_0 the interaction has a significant effect on the particle trajectory. From this we can follow

$$\alpha \ll r_0 \rightarrow l \ll l_{max} = \frac{pr_0}{\hbar} = \frac{2\pi r_0}{\lambda_{dB}}, \tag{2.32}$$

and we see that it exists an upper bound for the number of partial waves that has to be taken into account in the partial wave expansion. Since $\lambda_{dB} \gg r_0$, $l_{max} \rightarrow 0$ in Equation 2.32 and we can write the scattering amplitude as

$$f(k \rightarrow 0) = \frac{1}{2ik}\left(e^{2i\delta_0} - 1\right). \tag{2.33}$$

The total cross-section is then obtained by integrating the differential cross-section over the full solid angle

$$\sigma_{\text{tot}}(k) = \sum_l \sigma_l(k) = \frac{4\pi}{k^2} \sum_{l=0}^{\infty} (2l+1) \sin^2(\delta_l(k)), \quad \text{with} \quad \delta_l(k) \propto k^{2l+1}, \tag{2.34}$$

which simplifies since $l = 0$ to

$$\sigma_{tot}(k) = \frac{4\pi}{k^2} \sin^2(\delta_0(k)) \to 4\pi a^2 \quad \text{for} \quad k \to 0. \tag{2.35}$$

The universal parameter describing the scattering at low temperatures is the scattering length a which is defined by

$$a = -\lim_{k \to 0} \frac{\tan \delta_0(k)}{k}. \tag{2.36}$$

This can be related to the maximum distance the free particle solution of the Schrödinger equation is affected by the interaction potential. For alkali atoms a is on the order of 10 to $100a_0$ where a_0 corresponds to the Bohr radius. Hence, we can write the s-wave scattering amplitude in terms of the scattering length a [Zwi06]

$$f(k) = -\frac{1}{a^{-1} + ik}, \tag{2.37}$$

and the total cross-section for distinguishable particles in the low temperature regime takes the form

$$\sigma_{dist} = \frac{4\pi a^2}{1 + k^2 a^2}. \tag{2.38}$$

Here we have already approximated the interaction potential by a point-like contact potential $V(r) \sim a\delta(r)$. In the limit of weak interaction $ka \ll 1$ the total cross-section becomes energy independent

$$\sigma_{dist} = 4\pi a^2. \tag{2.39}$$

In the regime where $ka \gg 1$, known as the regime of resonantly enhanced interactions or unitarity limit, where a diverges, the total cross-section is only energy dependent

$$\sigma_{dist} = \frac{4\pi}{k^2}. \tag{2.40}$$

Since we are in the ultracold temperature regime the particles become indistinguishable which means that one cannot discern between the two scattering processes seen in Figure 2.2. Thus, to determine the scattering amplitude both possibilities have to be taken into account. This leads to the following modification of the differential cross-section

$$\frac{d\sigma_{indist}}{d\Omega} = |f(k,\theta) \pm f(k,\pi-\theta)|^2. \tag{2.41}$$

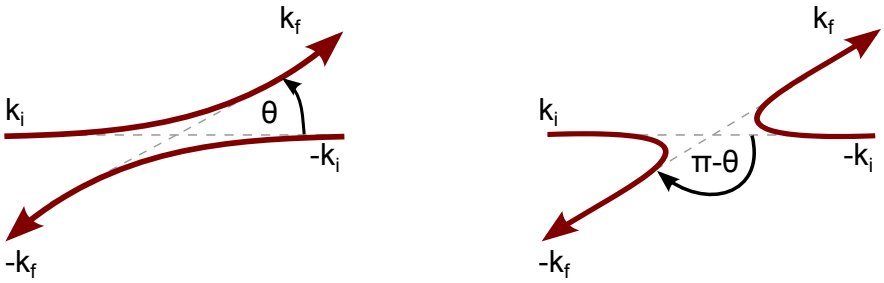

Figure 2.2.: **Scattering events for indistinguishable particles.** Since both processes cannot be distinguished, one has to take both into account in the total scattering amplitude. This leads to a modification of the cross section. The picture is adapted from [Dal98]

Here the plus sign (symmetric wave function) labels the bosonic case and the minus sign (anti-symmetric wave function) corresponds to fermionic particles. The difference between both scattering cases are just the different angles in the amplitude and since s-wave scattering is isotropic we end up with an enhancement in the bosonic total cross-section whereas the total cross-section for identical fermions vanishes.

$$\sigma_{bosonic} = 8\pi a^2 \quad \text{and} \quad \sigma_{fermionic} = 0. \tag{2.42}$$

Thus, identical fermions do not interact at low temperatures and can be well described as an ideal Fermi gas.

2.3.2. Mean field interaction energy

As mentioned before due to the fact that the details of the interaction potential are not resolved for low temperature scattering, the effective interaction potential can be well approximated by a point-like contact potential [CCT11]

$$V_{int}(\mathbf{r}) = \frac{2\pi\hbar^2 a}{m}\delta(\mathbf{r}). \tag{2.43}$$

With this pseudo-potential ($m = m/2$ for identical particles) it is possible to calculate the mean-field interaction energy in the weakly interacting regime $ka \ll 1$. This has been done in [Joc04] and the mean-field interaction energy of a many-body system of N particles due to a single test particle placed at $\mathbf{r}$ in a volume V at a density $n = N/V$

is given by

$$E_{int} = \lim_{V\to 0} \frac{1}{V} \sum_{i=1}^{N} \int g\delta(\mathbf{r} - \mathbf{r}_i) d\mathbf{r} = gn \quad \text{with} \quad g = \frac{4\pi\hbar^2}{m} a. \tag{2.44}$$

Since the mean-field interaction energy depends linearly on the scattering length a, the sign of a also determines the sign of the interaction energy. So for $a > 0$ the interaction energy will be positive and increase the total energy of the system. Hence the single particle will sense a repulsion by the mean-field whereas if $a < 0$ the contribution of the mean-field interaction energy will be negative and the single particle will be attracted by the mean-field. But this does not mean that the microscopic interparticle interaction for $a > 0$ is repulsive. The microscopic scattering is still described by van-der-Waals interaction which is attractive and independent of the sign of the scattering length a. So the mean-field interaction energy argumentation just holds on a macroscopic scale.

2.3.3. Controlling interactions via Feshbach resonances

Tuning the interactions via Feshbach Resonances has already been investigated both in experimental [Ino98, Chi10] and theoretical publications [Fes58, Moe95, Pet02, Pit03]. We will therefore only give a qualitative overview of this effect.

In Figure 2.3 (a) two effective interaction potentials of a s-wave scattering process between two particles are depicted (black and red curve). The difference between both interaction potentials stems from the electronic spin configuration (e.g singlet or triplet) of the participating particles which results in the different continuum energy. A single scattering channel is given by a complete set of quantum numbers describing the internal state of the two participating particles. Since the experiments presented in this thesis are based on ultracold ^{6}Li atoms this different spin configuration corresponds in our case to different hyperfine states in ^{6}Li (for details see Section 2.3.4). The energy of the scattering particles corresponds to the incident energy in Figure 2.3 (a) and is set to the continuum energy of the open channel since the kinetic energy can be neglected for ultracold scattering. The interaction potentials are labeled as closed (red) and open channel (black) respectively its accessibility by the incident energy in the long distance limit. In quantum mechanics one can show that the scattering length depends on the distance between a bound state and the continuum [Lan81]. For example, if we consider just scattering in the open channel, the scattering length is fixed and depends on the distance between the last bound state of the open channel to the continuum.
Since the two interaction potentials depend on the hyperfine states of our participating particles, their magnetic momenta differ and thus the difference in their continuum energy is given by $\Delta E = \Delta\mu B$. This means, that one can tune a bound state of the closed channel with a homogeneous magnetic offset field close to the continuum of the open channel and even above if the difference between the magnetic moments is nonzero. As mentioned before, the scattering length is very sensitive to the distance between bound state and continuum. If the tuned bound state is closely above or below the

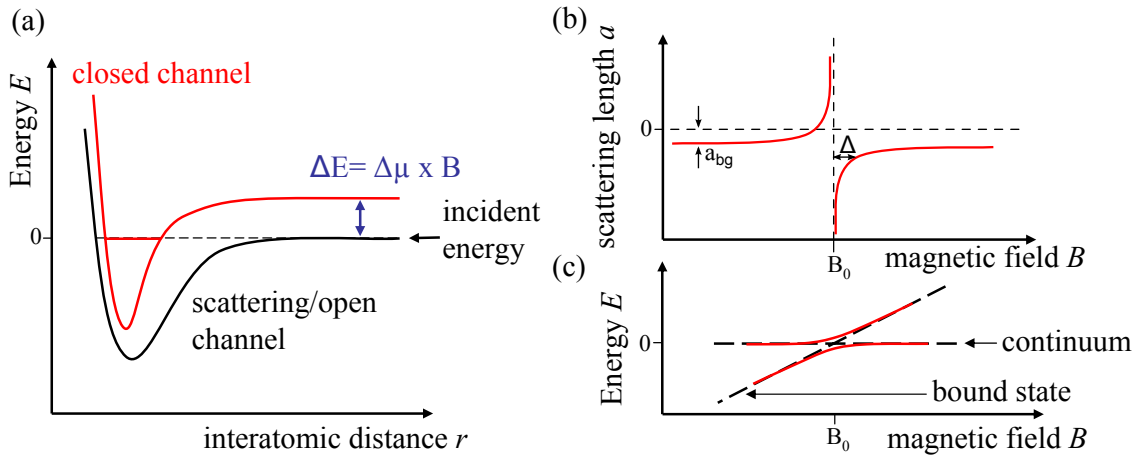

Figure 2.3.: **Two-channel model of a Feshbach resonance.** In (a) the interaction potentials are depicted where the open channel is energetically accessible for the incoming particles in contrast to the closed channel. The tuning of the coupling between one bound state of the closed channel with a continuum of the open channel leads to the divergence of the scattering length a shown in (b). In (c) the avoided crossing of the new eigenstates of the system (red) is illustrated and the crossover from a free particle state in the continuum to a bound molecular state by adiabatically tuning of the magnetic field B and vice versa can be seen. The picture is adapted from [Wen08].

continuum the scattering length is resonantly enhanced and diverges to large negative or large positive values at the resonance position B_0 as seen in Figure 2.3 (b). Thus, to tune the scattering length over a wide range with accessible magnetic fields one has to use atomic species with a bound state close to the continuum.
Such a resonant enhancement of the scattering length a due to a coupling of two scattering channels is called a Feshbach resonance. The dependence of a on the magnetic field can be calculated as [Bar05]

$$a(B) = a_{bg}\left(1 - \frac{\Delta}{B - B_0}\right)(1 + \alpha(B - B_0))\,, \tag{2.45}$$

where a_{bg} corresponds to the background scattering length of the open channel, B_0 describes the resonance position and Δ is the width of the resonance which depends on the coupling g and the difference of magnetic moments $\Delta\mu$ of the channels. The second term corresponds to a leading-order correction parametrized by α. Due to the coupling between the closed channel and the open channel the energy of the particles get dressed and the new eigenstates of the system are formed by a superposition of the bound state of the closed channel and the continuum state of the open channel. These new eigenstates (red) are shown in Figure 2.3 (c) where the dashed black lines

are the bound state of the closed channel and the continuum state of the open channel respectively. The superposition leads to an avoided crossing of the new eigenstates at resonance which offers the opportunity to go adiabatically from a high vibrational molecular bound state (left) to a free particle continuum state just by tuning the magnetic offset field slowly across the resonance and vice versa.
As we pointed out earlier, ultracold gases are a very dilute system so the interparticle distance is much larger than the range of interaction r_0. Feshbach resonances allow us now to tune the interparticle interaction to values on the order of the interparticle spacing which means that the system becomes a highly correlated many-body state [Lom11]. Since r_0 remains smaller than the interparticle spacing the interactions can still be described as point-like.

2.3.4. Basic properties of Lithium

Since we are using ^{6}Li in our experiments, we want to give in this section a short summary of the spectral and collisional properties of ^{6}Li based on [Chi10, Geh03].

Spectral properties

Lithium has only one valence electron and thus it is an alkali atom with spin $S = 1/2$. The fermionic isotope ^{6}Li we operate with has a nuclear spin $I = 1$. In low magnetic fields the total angular momentum is given by the Russell-Saunders coupling as $\mathbf{J} = \mathbf{L} + \mathbf{S}$ and J couples due to the non-zero nuclear momentum I as $\mathbf{F} = \mathbf{J} + \mathbf{I}$ to the total angular momentum of the system, which is a good quantum number for low magnetic fields. This leads to a large hyperfine splitting into $F = 1/2$ and $F = 3/2$ of the ground state $2^2S_{1/2}$ which can be seen in Figure 2.4 where the level scheme of the three lowest fine structure levels (left) and the corresponding hyperfine levels (right) are depicted.

For cooling and trapping we use the electronic D_2 transition between the ground state $2^2S_{1/2}$ and the excited state $2^2P_{3/2}$ which is characterized by a transition wavelength of 670.977 nm and a natural linewidth $\Gamma = 5.87$ MHz. The difference between the D_2 transition and the D_1 transition, which is likewise in the visible range of the electromagnetic spectrum and has the same linewidth Γ, is that the excited $2^2P_{3/2}$ state due to the hyperfine splitting of 4.4 MHz can not be resolved and the excited electron can decay back into both hyperfine states of the ground state $2^2S_{1/2}$. Thus, to create a closed cycle between the ground state and the excited state one needs to drive two transitions separated by 228.2 MHz which we call cooler and repumper transition.

So far we discussed the level scheme in the absence of any magnetic field where the degeneracy of the hyperfine states is given by the magnetic quantum number $m_F = -F, ..., F$ of the total angular momentum. Since we will later just use hyperfine states of the ground state, we will now focus on the effect of a non-zero magnetic field on the degeneracy of the ground state $2^2S_{1/2}$. As seen in Figure 2.5 the degeneracy is abolished for a nonzero magnetic field. Due to the exceptional small hyperfine constant

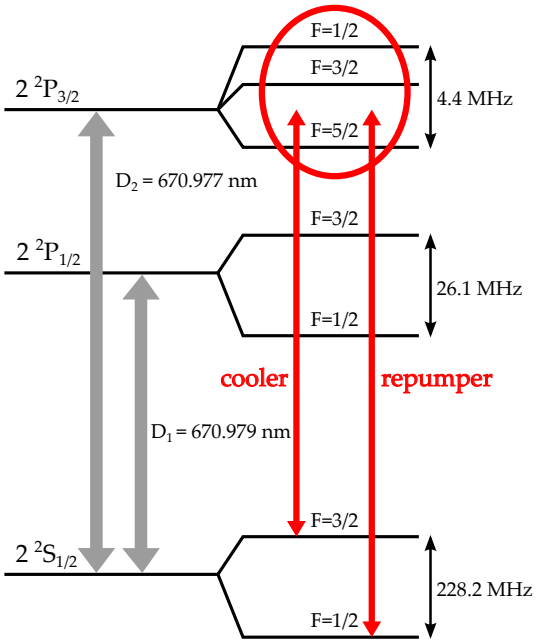

Figure 2.4.: **Level scheme of ^{6}Li.** The D_2 transition is used for cooling and trapping of the atoms. Due to the hyperfine splitting of the ground state we need to drive a cooler and repumper transition to achieve a closed cycle. The picture is adapted from [Boh12]

of ^{6}Li the angular momentum J (here S because $L = 0$) and the nuclear spin I decouple for magnetic fields larger than $B = 30$G and F is not a good quantum number anymore. Thus, we have to characterize the states by a new set of quantum numbers given by $|S = 1/2, I = 1, m_S, m_I\rangle$. This leads to two types of states: $|m_S = -1/2, m_I = 0, \pm 1\rangle$ labeled by $|1\rangle - |3\rangle$ which minimize their internal energy at high magnetic fields and are therefore called high-field seeking states and states with $|m_S = +1/2, m_I = 0, \pm 1\rangle$ labeled as $|4\rangle - |6\rangle$ corresponding to low-field seeking states because they minimize their internal energy at low magnetic fields. Typical fields in the experiment are on the order of $B > 100$G and therefore we operate deeply in the decoupled regime. The almost parallel tuning of the energy states with same m_S for high magnetic fields results from the fact that the coupling of the electron spin to the magnetic field is much larger than the coupling of the nuclear spin.

Collisional properties

Since identical fermions do not interact with each other as discussed in Section 2.3.1 we always need two different hyperfine states to have interaction in the system. In our experiments we use binary mixtures of the high-field seeking states $|1\rangle - |3\rangle$ because the low-field seeking states $|4\rangle - |6\rangle$ are not stable due to decay via spin-changing collisions into the high-field seeking states and the released energy will lead to atom loss. The

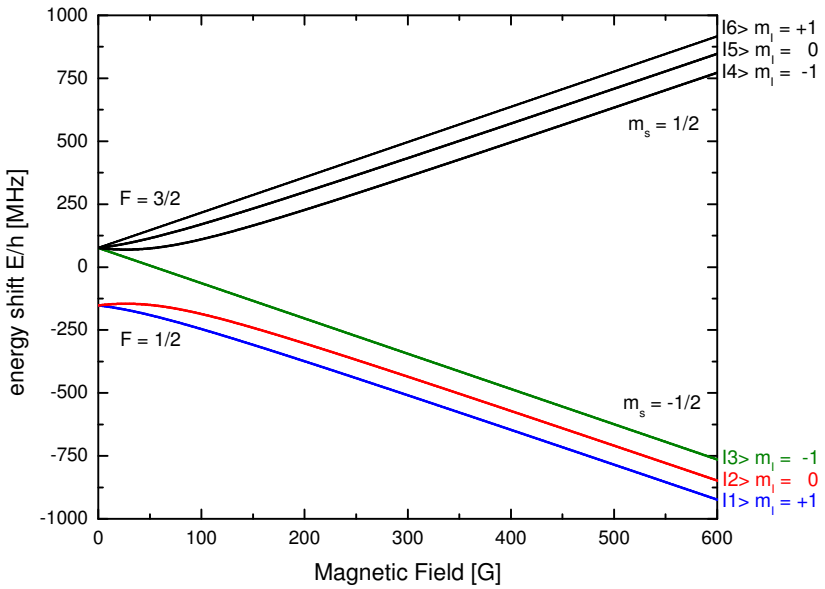

Figure 2.5.: **Magnetic field dependency of the ground state energy splitting of ^{6}Li.** For magnetic fields larger than $B = 30$G we are in the Paschen-Back regime, S and I decouple and become good quantum numbers, which leads to the displayed splitting.

states $|1\rangle - |3\rangle$ are stable on the timescales of our experiment and since the separation between the single states is on the order of ~ 80 MHz we can apply radio frequency pulses to drive transitions between them. It is also possible to drive transitions to the low-field seeking states using microwave pulses in the GHz range.
As discussed in Section 2.3.3, the interaction of each combination of the high-field seeking states can be related to a corresponding scattering length a_{12}, a_{13} and a_{23}. In Figure 2.6 the different Feshbach resonances are shown and in Table 2.1 the position B_0, width Δ and background scattering length a_{bg} for each scattering channel are given. These values have been determined in our group using very precise radio-frequency dissociation spectroscopy of weakly bound $^6Li_2$ molecules and a coupled channel calculation which optimized the exact potential shape and allowed us to determine the pole position with an accuracy better than 7×10^{-4} of the resonance widths[Zür13].
If one compares the actual characteristics of the scattering length to the schematic picture given in Figure 2.3 (b), one might recognize a certain asymmetry. As mentioned in Section 2.3.3 the effective interaction potential depends on the relative orientation of the electronic spins of the participating particles. They can be orientated either in a singlet ($\uparrow\downarrow$) or triplet ($\uparrow\uparrow$) meaning $S^2 = 1, M_S = 0$ for singlets and $S^2 = 1, M_S = \pm 1, 0$ for triplets. Since m_S is not a good quantum number in the low field regime, the

Scattering channel	B_0 [Gauss]	Δ [Gauss]	a_{bg} $[a_0]$
$\|1\rangle\|2\rangle$	832.2	262.3	-1582
$\|1\rangle\|3\rangle$	689.7	166.6	-1770
$\|2\rangle\|3\rangle$	809.8	200.2	-1642

Table 2.1.: **Characteristic values of the s-wave Feshbach resonances for the three lowest hyperfine states.** A more detailed description can be found in [Zür13].

background scattering length will be a linear combination of the singlet background scattering length a_s and the triplet background scattering length a_{tr} which differ quite significantly in their value e.g. for the $|1\rangle - |2\rangle$ mixture one obtains $a_s \approx 39a_0$ and $a_{tr} \approx -2240a_0$ [Lom11]. However, the value of the superimposed background scattering length remains small. Since the value of the scattering length can be related to

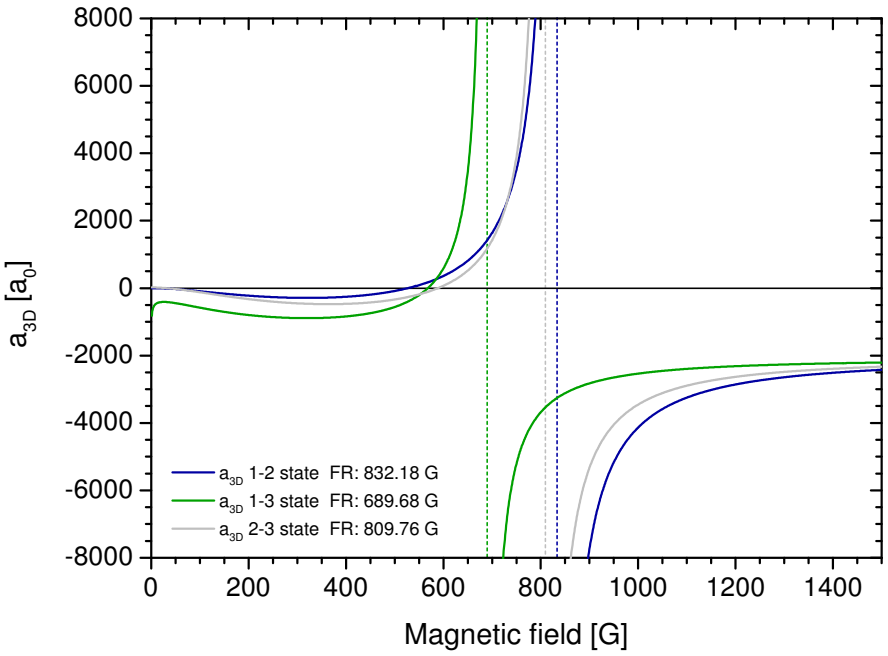

Figure 2.6.: **Feshbach resonances for the three lowest hyperfine states of ^{6}Li.** All three mixtures of the high-field seeking hyperfine states have a particular broad and overlapping Feshbach resonance, which allows a precise control of the interactions. Plot was adapted from [Zür12]

the distance between a bound state of the closed channel and the continuum of the open channel, it follows that this distance has to be really small in case of the triplet scattering length. In fact the virtual bound state sits so close above the continuum of the triplet potential that a change less than 10^{-3} of the potential depth would already lead to a sign change in a_{tr} [Joc04].

The magnetic moment depends on the electronic spin and thus allows us to tune the energy of the triplet channel ($M_S = -1/2 + (-1/2) = -1$) with $2\mu_{Bohr} \sim h \times 3$ MHz/G while the singlet state stays unchanged ($M_S = 0$). By increasing the magnetic field B one tunes on the one hand the contribution of the singlet and triplet background scattering length and on the other hand the distance between the triplet continuum and the highest vibrational singlet bound state ($\nu = 38$). This leads to the zero crossing of the scattering length on the left side of the resonances depicted in Figure 2.6.
Thus the Feshbach resonances are obtained by tuning the continuum of the triplet interaction potential resonantly with the highest vibrational level of the singlet channel from below. When S and I decouple and thus become good quantum numbers, the scattering becomes triplet dominated which leads to a large negative background scattering length $\sim -2000a_0$ on the right side and therefore to a range of $-1000a_0$ to $-2000a_0$ which cannot be accessed. Furthermore, a second very narrow resonance can be localized at 543 G which we so far do not incorporate in our experiments.

2.4. Interacting Fermions

In this section we focus on the different interaction regimes which can be accessed in a two component Fermi gas due to the possibility of tuning the interparticle interactions over a wide range via a Feshbach resonance as introduced in the section before. Since a spin polarized Fermi gas can be well described by a non-interacting Fermi gas due to the absence of s-wave collisions, we consider here a balanced spin mixture of the lowest two hyperfine states of ^{6}Li labeled by $|1\rangle$ and $|2\rangle$. The strength of interaction is quantified by the dimensionless interaction parameter $1/k_F a$ which relates the interparticle spacing $\sim 1/k_F$ to the scattering length a. By tuning the scattering length we are able to access three different interaction regimes depicted in Figure 2.7. $1/k_F a \to +\infty$ which corresponds to the BEC regime and formation of molecules occurs and $1/k_F a \to -\infty$ the so-called BCS regime where in spite of the absence of a molecular bound state correlation in momentum space takes place and so-called Cooper pairs can be formed. These two limiting cases are continuously connected by the Unitary regime which is called the BEC-BCS crossover. The Unitary regime is characterized by the divergence of the scattering length and hence $1/k_F a \to 0$.

2.4.1. Formation of Feshbach molecules in the BEC regime

Tuning the interaction close to the Feshbach resonance on the repulsive side with $a > 0$ leads to the formation of weakly bound molecules by three-body recombination where the excess momentum is carried away by the third particle. One can associate a universal binding energy $E_B = \hbar^2/ma^2$ for $a \gg r_0$ to this molecular bound state [Pet04b]. When the temperature of the ultracold gas is smaller than E_B two fermions with different spin can occupy this bound state and create a composite bosonic molecule as seen in Figure 2.8. The size of the weakly bound molecules is on the order of the scattering

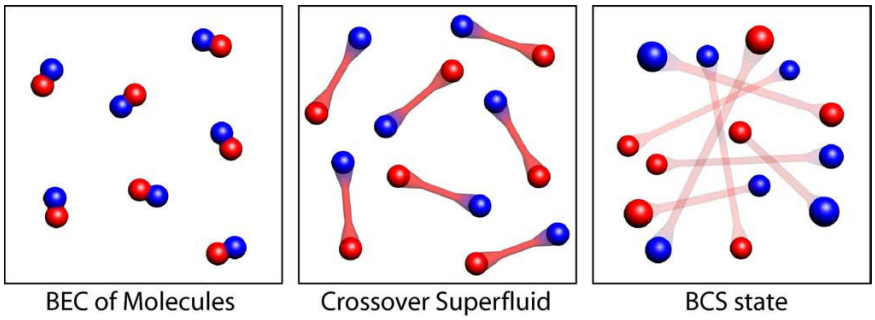

Figure 2.7.: **Pairing in the different interaction regimes.** In the BEC regime pairing occurs via deeply bound molecules which are smaller than the interparticle spacing. In contrast, on the BCS side of the resonance Cooper-pairs are formed by two fermions with opposite momentum on the Fermi sphere so they exhibit an extend larger than the interparticle spacing. Since the two regimes are continuously connected by the region of unitarity the size of the strongly correlated pairs in the crossover regime is on the order of the interparticle spacing. Picture is taken from [Ket08]

.

length a and since the bound molecular state is still in a high vibrational energy state, the molecules can undergo further three-body inelastic collisions with the ultracold background gas which would transfer them into deep molecular bound states on the order of the range of interaction $r_0 \ll a$ [CCT11]. During this relaxation process a lot of binding energy is released, which results in a loss of atoms in the trap if the gained kinetic energy is larger than the trapping potential depths.
Due to the Pauli principle it turns out that Feshbach molecules formed from two fermionic atoms in two different spin states are less sensitive to these inelastic processes than those formed by bosonic atoms. Since in a two-component Fermi gas a three-body collision process involves necessarily two atoms in the same spin state the inelastic collision rate is suppressed. The dependency of the loss coefficient α of the inelastic collision rates for atom-molecule scattering and molecule-molecule scattering on the scattering length has been calculated in [Pet04b]

$$\alpha_{dd} \propto a^{-2.55} \quad \text{and} \quad \alpha_{ad} \propto a^{-3.33}, \tag{2.46}$$

and the collisions have been described in terms of the atomic scattering length a with [Pet05]

$$a_{dd} = 0.6a \quad \text{and} \quad a_{ad} = 1.2a. \tag{2.47}$$

Thus, the inelastic collision rate decreases for increasing a which leads to long lifetimes of the Feshbach molecules close to the Feshbach resonance. Hence one can further

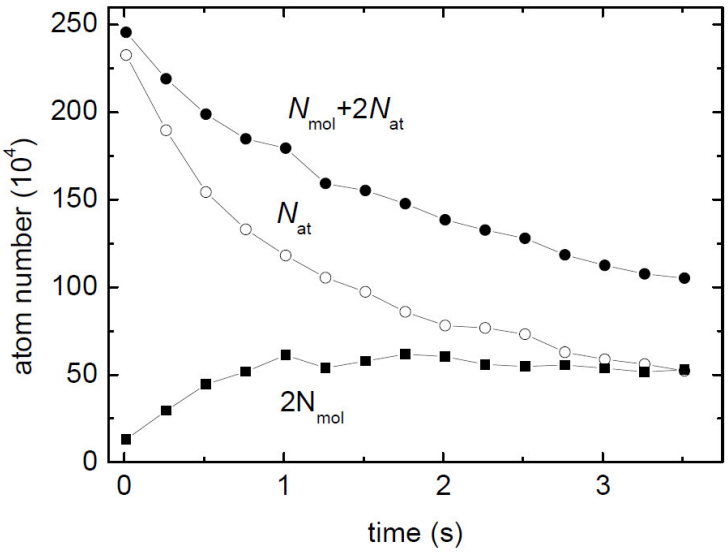

Figure 2.8.: **Formation of $^6Li_2$ molecules at 690G.** Evaporative cooling was performed at 1200G, then the magnetic field was ramped down quickly to 690G for optimum production rates. Taken from [Joc04]

condense them into a molecular BEC (mBEC) by decreasing the temperature [Joc03, Gre03, Zwi03].
Furthermore, the trap depth is increased by a factor two for molecules because of the two times larger polarizability which suppresses the loss of molecules in contrast to the loss of atoms [Joc04]. Since we are dealing with bosonic molecules, one can apply the theory of interacting bosons in the limit $1/k_F a \to +\infty$ as discussed in Section 2.2.4. Thus, e.g. the 3D density distribution in the Thomas-Fermi limit is given by [Dyk10]

$$n(\mathbf{r}, T=0) = \frac{15N}{16\pi^2 r_x r_y r_z}\left[1 - \left(\frac{x}{r_x}\right) - \left(\frac{y}{r_y}\right) - \left(\frac{z}{r_z}\right)\right], \tag{2.48}$$

$$r_i = r_{i,TF} = l_{ho}\frac{\bar{\omega}}{\omega_i}\left(\frac{15N_d a_d}{l_{ho}}\right)^{1/5}, \tag{2.49}$$

where one had to substitute the number of dimers $N_d = N_a/2$ with mass $m_d = 2m_a$ and the molecular scattering length $a_d = 0.6a$.

2.4.2. Cooper pairing in the BCS regime

For $1/k_F a \to -\infty$ we reach the weakly attractive interaction regime. Since the molecular bound state only exists for $a > 0$, a pairing process for $a < 0$ seems unphysical at first sight. Indeed, the pairing mechanism is completely different. Since in the BEC limit pairing is only a two-body phenomenon, Cooper pairs are called many-body pairs because the filled Fermi sea up to the Fermi surface is necessary for the formation pro-

cess. Thus, pairing is therefore not generated by the attraction to the other particle but is rather connected to the collective interaction with all particles around the Fermi surface. In 1957 Bardeen, Cooper and Schrieffer [Bar57] showed that the ground state of a balanced, non-interacting two-component Fermi gas at zero temperature with energy $E_0 = N \cdot \frac{3}{5} E_F$ is unstable against attractive interactions and that pairing in momentum space reduces the energy of the system in the following way [CCT11]

$$E_{BCS} = E_0 - \frac{1}{2}\rho(E_F)\Delta_0^2. \tag{2.50}$$

Here, E_{BCS} describes the energy of the attractively interacting BCS state, $\rho(E_F)$ corresponds to the density of states at the Fermi level and the Δ_0 is related to an energy gap in the excitation spectrum at the Fermi surface. Thus, the formation of so-called Cooper pairs, which consist of two particles of opposite momentum and spin, minimizes the energy of the system. The zero temperature pairing gap can be related to the energy which is required to break a pair [Dyk10] and depends exponentially on the absolute value of the scattering length a [Gio08]

$$\Delta_0 \sim \left(\frac{2}{e}\right)^{7/3} E_F \exp\left(-\frac{\pi}{2k_F|a|}\right). \tag{2.51}$$

Moreover, this pairing gap leads to superfluid behavior and one can calculate a critical temperature T_C for which the Cooper pairs become superfluid in a finite temperature system [Gio08]

$$k_B T_C = \frac{e^\gamma}{\pi}\Delta_0 \approx 0.28 E_F \exp\left(-\frac{\pi}{2k_F|a|}\right), \tag{2.52}$$

where $e^\gamma \sim 1.78$. In Figure 2.9 a) this behavior is depicted and further one can see that the critical temperature to create Cooper pairs T^* and the superfluid transition temperature T_C coincide in the limit of weakly attractive interaction meaning that the Cooper pairs only exist in the superfluid phase. The range between T^* and T^C for $a < 0$ is called the pseudogap regime. Moreover, the transition temperature T_C is very low compared to the transition temperature at the BEC side making the transition from a weakly interacting Fermi gas to the superfluid phase rather hard to realize.

2.4.3. The Unitary regime

The two limiting cases introduced before are connected around the Feshbach resonance by the unitary regime where $1/k_F a \to 0$ because the scattering length a diverges. From Section 2.3.1 we know that the total cross section $\sigma = 4\pi/k^2$ becomes then independent of a, leaving the interparticle spacing $\sim 1/k_F$ or $\sim n^{1/3}$ as the only relevant length scale in the system. That is the reason why this regime is called universal because all thermodynamic quantities only depend on the natural energy scale E_F. In Figure 2.9 (a) a schematic view of the whole BEC-BCS crossover is depicted. The BEC limit is

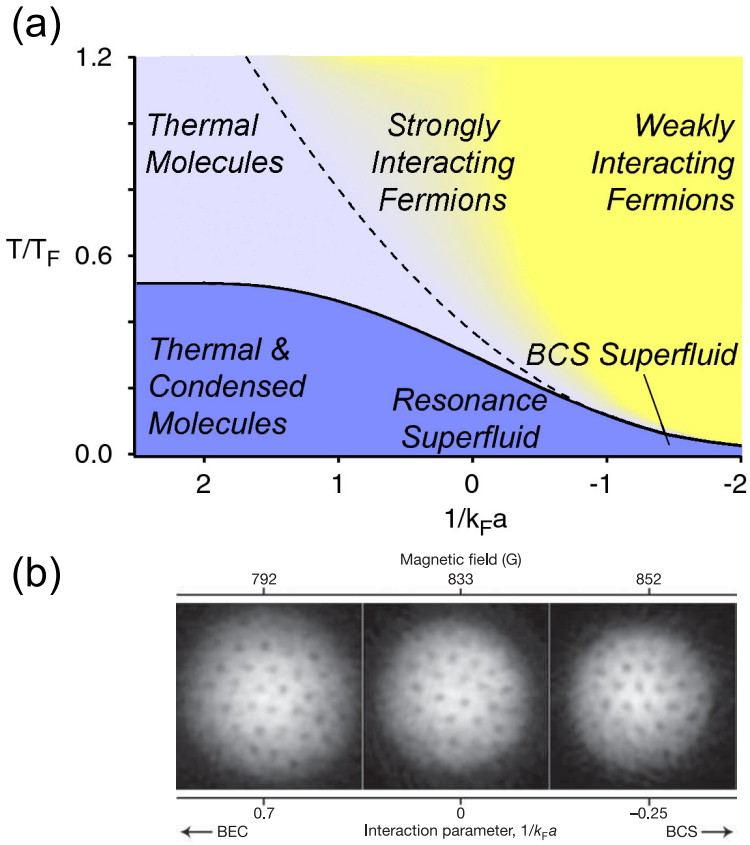

Figure 2.9.: **BEC-BCS Crossover.** In (a) a schematic phase diagram of the crossover region is shown. The dashed line corresponds to the pair creation temperature T^* and the solid line represents the behavior of the superfluid transition temperature T_C. (b) depicts the experimental data which validated the stability of a Fermi gas and the existence of the superfluid phase during the crossover. Both pictures are taken from [Zwi05]

shown on the left side and below a critical pairing temperature T^* (dashed line) weakly bound molecules can be formed which then can condense into a mBEC (become a superfluid) for $T < T_C$ (solid line). By reaching the unitary regime we see that T^* and T_C decrease but still leave a gap in between which vanishes for $1/k_F a \to -\infty$.
Experimentally the stability of a two-component Fermi gas while crossing the resonance has been observed by the group of Wolfgang Ketterle at MIT [Zwi05]. This was a remarkable observation since one expected the same result as for a BEC which becomes highly unstable for an abrupt change from repulsive to attractive interaction [Don01]. In a fermionic system the many-body physics combined with the Fermi pressure turns out to stabilize the gas during the change of interaction [CCT11]. Figure 2.9 (b) shows the observation of quantized vortices in a rotated Fermi gas along the strongly interacting regime ($1/k_F|a| \ll 1$) of the BEC-BCS crossover which are an indicator of

superfluidity. They demonstrated the existence of these vortices for several magnetic fields around the unitary limit and thus argued, that the Fermi gas stays superfluid along the whole BEC-BCS crossover.

3. Quantum degenerate gases in a quasi-2d confinement

As pointed out in the introduction, systems with reduced dimensionality exhibit new and interesting physics and allow further a deeper understanding of phenomenons like high-temperature superconductivity or superfluidity. Ultracold gases allow to study the physics of such lower-dimensional systems by confining a cloud of atoms in a strongly anisotropic trapping potential.
In this chapter we introduce in Section 3.1 the relevant energy scales and the two-body bound state of a quasi-2d system. Further we briefly discuss the changes in the quantum statistics and the scattering properties due to the reduced dimensionality in Section 3.2 and Section 3.3 respectively. In the last part of the chapter we motivate the mechanisms and characteristics of the Berezinskii-Kosterlitz-Thouless (BKT) transition predicted for two dimensional systems.

3.1. Characterization of a quasi-2d confinement

In our experiment the realization of a quasi-two dimensional quantum gas is achieved by confining the atomic cloud to an optical three dimensional harmonic potential, where the confinement in the axial direction is much stronger than in the radial directions. Due to the high trap anisotropy we achieve a population in just two dimensions at sufficiently low temperatures of the quantum gas where thermally excited particles can not occupy the third dimension. Hence we satisfy the conditions characterizing a two dimensional quantum system

$$k_B T, \mu, E_F \ll \hbar\omega_z, \tag{3.1}$$

where μ is the chemical potential and E_F corresponds to the Fermi energy. The transversal degree of freedom is thus frozen out and the atoms occupy the lowest transverse harmonic oscillator state and can only populate the levels of the radial confinement $\hbar\omega_r$. The different energy scales in the harmonic potential are schematically shown in Figure 3.1.

As we will discuss later in more detail, the reduced dimensionality affects the scattering properties of the system. This leads for a two dimensional Fermi gas to the existence of a confinement induced two-body bound state $E_{B,2D}$ for every magnetic

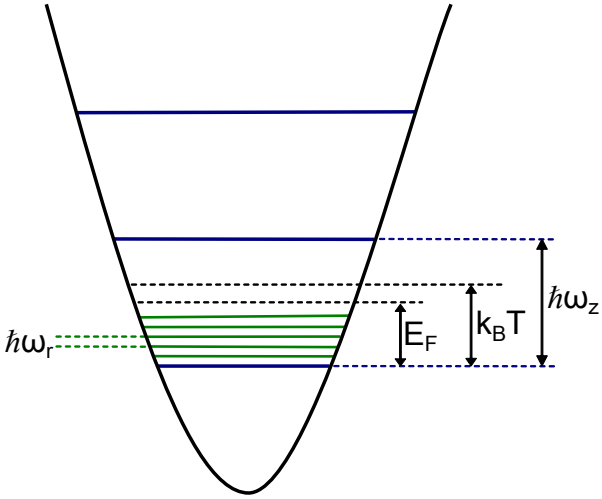

Figure 3.1.: **Sketch of the two dimensional harmonic confinement.** The radial harmonic oscillator levels defined by $\hbar\omega_r$ are populated whereas the gas just occupies the ground state of the axial confinement because E_F (or μ) is much smaller than $\hbar\omega_z$. This degree of freedom is thus frozen out and the system becomes quasi-two dimensional. The picture is adapted from [Frö11a].

field, which can be related to a 2d scattering length a_{2D} by the universal equation

$$E_{B,2D} = \frac{\hbar^2}{m a_{2D}^2}, \tag{3.2}$$

where m is the mass of the particles. The 2d scattering length a_{2D} and thus the binding energy depend on the trap geometry and can be connected to the three dimensional scattering length a via the transcendental equation [Blo08, Pet01]

$$\frac{l_z}{a} = \int_0^\infty \frac{du}{\sqrt{4\pi u^3}} \left(1 - \frac{\exp(-E_{B,2D}u/\hbar\omega_z)}{\sqrt{\frac{1}{2u}\left(1-\exp(-2u)\right)}}\right), \tag{3.3}$$

where $l_z = \sqrt{\hbar/m\omega_z}$ is the harmonic oscillator length characterizing the tight confinement in z-direction. In Figure 3.2 both the binding energy for a two-dimensional molecular state at $\omega_z = 2\pi \times 5.879$ kHz and the three dimensional molecular state as a function of the magnetic field are depicted. For weak attractive interaction and thus negative scattering length a and $|a| < l_z$, the molecular binding energy can be well approximated by [Blo08]

$$E_{B,2D} = 0.905(\hbar\omega_z/\pi)\exp(-\sqrt{2\pi}l_z/|a|), \tag{3.4}$$

which is shown in Figure 3.2 as well. Close to the 3d Feshbach resonance for diverg-

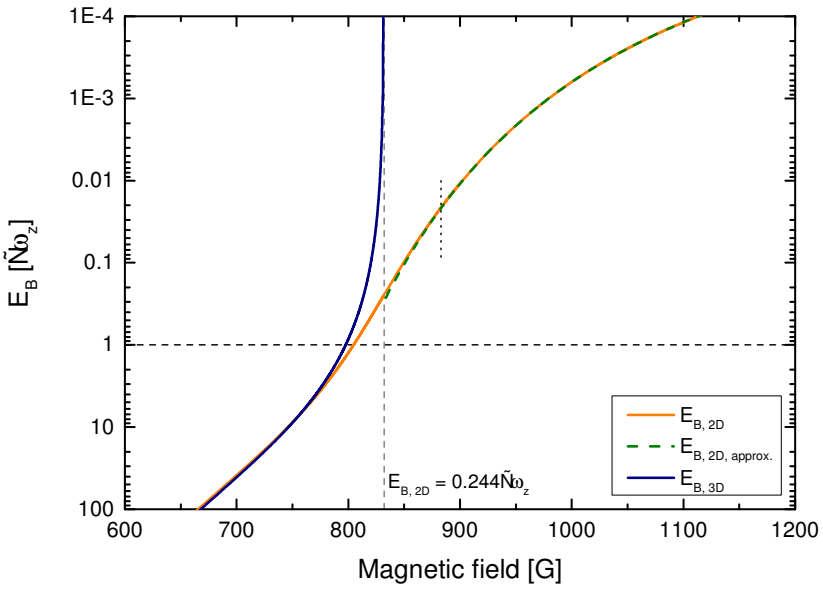

Figure 3.2.: **Molecular bound state in two and three dimensions as a function of the magnetic field.** The blue curve represents the three dimensional binding energy of a $|1\rangle - |2\rangle$ ^{6}Li dimer, which is 0 at the 3d Feshbach resonance (gray dashed vertical line). The two dimensional confinement induced binding energy (orange curve) stays non-zero even across the resonance. The green dashed plot describes the two dimensional binding energy approximated by Equation 3.4. It is valid for $|a| < l_z$, so from the black dotted line up to higher magnetic fields. In addition the small deviations from $E_{B,2D}$ are shown up to the Feshbach resonance. At the Feshbach resonance E_B is given by a universal constant $E_B = 0.244\hbar\omega_z$. The calculation has been done assuming $\omega_z = 2\pi \times 5.879$ kHz.

ing a, Equation 3.4 no longer holds and it can be replaced by the universal constant $E_B(a = \infty) = 0.244\hbar\omega_z$ [Blo08]. For a repulsive three dimensional scattering length $a > 0$ the two dimensional molecular state $E_{B,2D}$ approaches the three dimensional one $E_{B,3D}$. Then the size of the molecule given by $a_{2D} = \hbar/\sqrt{mE_B}$ becomes smaller than the characteristic length of the confinement l_z and so the binding energy is not longer affected by the confinement.
As seen in Figure 3.2, $E_{B,2D}$ is larger than $\hbar\omega_z$ for magnetic fields up to 800G (horizontal black dashed line), which means that the deeply bound molecules in this regime can be described as a quasi two dimensional Bose gas. The fermionic constituents do not become relevant until $E_{B,2D} \sim E_F$, which has to be smaller than $\hbar\omega_z$ in a quasi two dimensional system.
For two dimensional Bose gases it has been shown [Mer66, Had11, Hoh67, Bog60] that

for any finite temperature $T > 0$ thermal fluctuations destroy the true long range order (LRO) in the system. Since familiar phase transitions in three dimensional systems like freezing of water or Bose-Einstein condensation can be related to the emergence of true long-range order below some non-zero critical temperature, these phase transitions do not exist in two dimensional systems. The order of a system is characterized by a spatially uniform order parameter like the macroscopic wave function $\Psi = \sqrt{n}\exp(i\theta)$ in the case of a BEC. Besides that, the existence of true LRO can be connected to a spontaneous breaking of a continuous symmetry of the Hamiltonian, e.g. in the case of freezing water translational symmetry is spontaneously broken and in the case of Bose-Einstein condensation an arbitrary phase θ of Ψ is spontaneously chosen at the transition point.
The most general formulation is given by the Mermin-Wagner theorem which states that in all one- or two dimensional systems with short ranged interactions and a continuous symmetry in the Hamiltonian the symmetry is always restored by low energy, long wavelength thermal fluctuations called Goldstone modes. We will see in Section 3.4.2 that in case of an interacting Bose gas the Goldstone modes correspond to phonons [Mer66]. Nevertheless, this does not mean that any kind of phase transition is forbidden in low dimensional systems. So far we have discussed symmetry breaking phase transitions, but phase transitions which are characterized by the emergence of a topological order are still possible.
For low temperatures exists a phase transition to a superfluid 'quasi condensate' phase which is described by the Berezinskii-Kosterlitz-Thouless theory (BKT) [Ber71, Kos73] and is characterized by a topological order. In BKT theory, below a critical temperature T_{BKT} this topological order results from pairing of vortices with opposite circulations, whereas for temperatures above T_{BKT} proliferation of free vortices is expected. In [Had06] a BKT-type crossover has been observed in a bosonic system confined to a quasi two dimensional geometry and in [Cho13] the pairing of vortices was detected.

3.2. Quantum Statistics in two dimensions

The absence of Bose-Einstein condensation in homogeneous two dimensional systems can be seen in more detail from a quantum statistical argumentation. Thus, we will briefly compare the quantum statistics of an ideal bosonic system in two and three dimensions and then calculate several quantities for the trapped non-interacting 2d Bose and Fermi gas, which will become important in the experimental part of this thesis. We follow here the argumentation from [Had11].

3.2.1. Absence of Bose-Einstein condensation in ideal 2d systems

From Einstein's argumentation one obtains that condensation is related to a saturation of the excited single particle states at some non-zero temperature. In the following

calculation we assume an ideal, spinless two dimensional Bose gas.
The density of states is then given by $g_{2D} = mL^2/(2\pi\hbar^2)$ with $L \to \infty$ describing the size of the system. The crucial difference between the density of states of a free 2d system and the corresponding density of states in 3d is, that in 2d the density of states is independent of the energy ϵ because $g(\epsilon) \sim \epsilon^{d/2-1}$ holds, where d labels the dimension of the system. In absence of condensation and using Equation 2.9 the total number of particles can be derived as

$$N_{2D} = \frac{mL^2}{2\pi\hbar^2} \int_0^\infty \frac{d\epsilon}{\exp(\beta(\epsilon - \mu)) - 1}. \tag{3.5}$$

Here we defined $\beta = 1/(k_B T)$ and the chemical potential $\mu \leq 0$.
The two dimensional phase-space density D_{2D} is defined as $D_{2D} = n\lambda_{thermal}^2$ where $n = N_{2D}/L^2$ corresponds to the two dimensional number density[1]. Hence, due to the energy independence of the density of states g_{2D}, we obtain the following relation for ${D_{2D}}^2$ in terms of the fugacity $Z = e^{\beta\mu}$

$$D_{2D} = \int_0^\infty \frac{dx}{Z^{-1}\exp(x) - 1} = -\ln(1 - Z). \tag{3.6}$$

In 3d the density of states is given by $g_{3D}(\epsilon) = Vm^{3/2}\sqrt{\epsilon}/(\sqrt{2}\pi^2\hbar^3)$ and thus the phase-space density can be written as

$$D_{3D} = n_{3D}\lambda^3 = \frac{\beta}{\sqrt{2}\pi^2} \int_0^\infty \frac{\sqrt{x}dx}{Z^{-1}\exp(x) - 1} = \beta Li_{3/2}(Z), \tag{3.7}$$

where $Li_{3/2}(z)$ is the polylogarithmic function. Since $\mu \leq 0$, D_{3D} has no solution for Z when the phase-space density is larger than $n_{3D}\lambda^3 \approx 2.612$ which means that for $T < T_c$ and $\mu = 0$, the phase-space density of excited single particles saturates at ~ 2.612.
On the other hand, D_{2D} always has a solution for Z given by

$$e^{\beta\mu} = 1 - \exp(-n\lambda^2). \tag{3.8}$$

Hence, for any non-infinite phase-space density it exists a negative value μ which allows normalization of the thermal distribution of excited single particles to the total number of particles N. Thus, BEC does not occur in the ideal infinite uniform Bose gas [Had11].

The interesting fact that BEC does not occur in an ideal infinite 2d systems can be further seen by characterizing the long range order of the system. A measure of long range order can be achieved by the first-order correlation function $g_1(\mathbf{r})$ which is shown in Figure 3.3 for both the three dimensional case a) and the two dimensional case[3] b).

[1] In further calculations we relabel $\lambda_{thermal}$ as λ just for simplicity.
[2] Here we substituted $x = \beta\epsilon$.
[3] The functional form of the depicted curves is given by equations for a weakly interacting bosonic

$g_1(\mathbf{r})$ is defined independently of the dimensionality of the system by

$$g_1(\mathbf{r}) = \left\langle \hat{\Psi}^\dagger(\mathbf{r})\hat{\Psi}(0) \right\rangle, \tag{3.9}$$

where $\hat{\Psi}(\mathbf{r})$ corresponds to the field operator annihilating a single particle at position $\mathbf{r}$. True long range order (LRO), necessary for Bose-Einstein condensation, is achieved if the first-order correlation function converges to a finite value for $r \to \infty$, whereas if true long range order is destroyed in the system, $g_1(r)$ always tends to zero for increasing r. As seen in Figure 3.3 b) the first order correlation function in two dimensions at a temperature T equal or smaller than the transition temperature T_{BKT} decays slowly, which enables only a quasi long range order dependent on the length scale of the system. To introduce this really important phenomenon in 2d systems we start investigating the first-order correlation function in a non-interacting system.
In the case of an ideal two dimensional uniform Bose gas, $g_1(r)$ is given by the Fourier transform of the momentum space distribution function $n_k = \frac{1}{\exp(\beta(\epsilon_k-\mu))-1)}$ with $\epsilon_k = (\hbar k)^2/(2m)$

$$g_1(r) = \frac{1}{(2\pi)^2}\int_0^\infty \frac{\exp(i\mathbf{kr})}{\exp(\beta(\epsilon_k-\mu))-1} d^2k, \tag{3.10}$$

which shows a different behavior for a degenerate and non-degenerate gas.
For a non-degenerate gas $Z \approx n\lambda^2 \ll 1$ (see Equation 3.8) and with $|\mu| \gg k_BT$ the momentum distribution is given by

$$n_k \approx Z\exp(-\beta\epsilon_k) \approx n\lambda^2 \exp\left(\frac{-(k\lambda)^2}{4\pi}\right) \ll 1 \quad \text{for all } k. \tag{3.11}$$

Thus, all momentum states are weakly occupied and $g_1(r)$ becomes Gaussian with short range correlation decaying on a length scale $l = \lambda/\sqrt{\pi}$

$$g_1(r) \approx n\exp\left(\frac{-\pi r^2}{\lambda^2}\right). \tag{3.12}$$

In a degenerate gas ($n\lambda^2 > 1$) we obtain $Z \approx 1$ and the mean occupation for large momenta $\beta\epsilon_k \gg 1$ is decreased given by [Had11]

$$n_k \approx \exp(-\beta\epsilon_k) = \exp\left(-\frac{(k\lambda)^2}{4\pi}\right), \tag{3.13}$$

which is smaller than 1 for $k^2 \gg 4\pi/\lambda^2$ whereas the mean occupation for low momentum states $\beta\epsilon_k \ll 1$ since $Z \approx 1$ can be written as

$$n_k \approx \frac{k_BT}{\epsilon_k + |\mu|} = \frac{4\pi}{\lambda^2}\frac{1}{k^2+k_c^2}, \tag{3.14}$$

system obtained from L. Mathey by private communications.

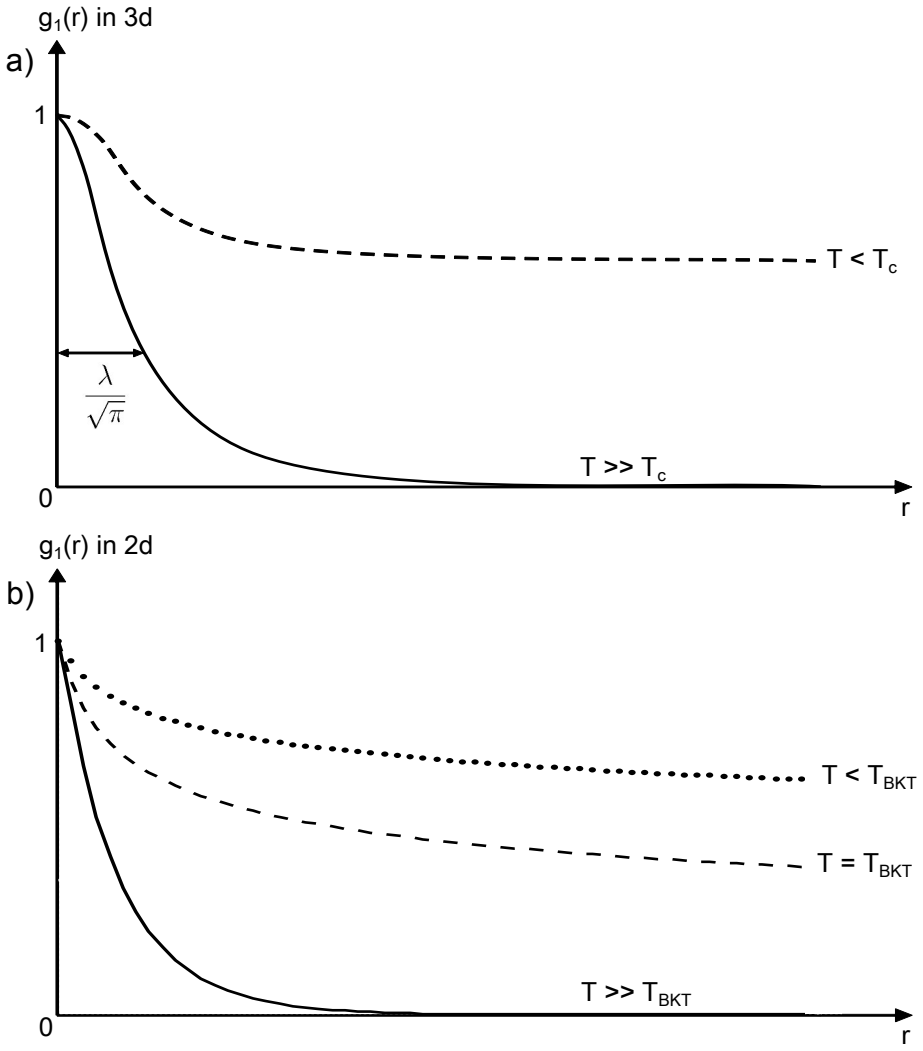

Figure 3.3.: **Normalized first order correlation function of a homogeneous Bose gas.** In the 3d case depicted in a) the coherence length l is infinite reflecting the true long range order in the system for $T < T_c$ (dashed line). $g_1(r)$ approaches a constant value for $r \to \infty$ which corresponds by the definition of Penrose-Onsager [Pen56] to the condensate density. In a non-degenerate system (solid line), thus at $T \gg T_c$ the coherence length l is given by $\lambda/\sqrt{\pi}$ so that no true LRO is established. The difference in the 2d system b) is, that here even for $T << T_{BKT}$ $g_1(\mathbf{r})$ does not converge to a constant value for $r \to \infty$ and hence no true long range order can be established. Due to the slow but continuous decay of $g_1(\mathbf{r})$ only a quasi-long range order dependent on the size of the system can be arranged.

which is larger than 1 for $k^2 \ll 4\pi/\lambda^2$ and $k_c = \sqrt{2m|\mu|}/\hbar$. Thus, the first order correlation function $g_1(r)$ becomes bimodal for an ideal degenerate gas. The Lorentzian form of Equation 3.14 leads to the following decay of $g_1(r)$

$$g_1(r) \approx \exp\left(-\frac{r}{l}\right) \quad \text{where} \quad l = 1/k_c \approx \frac{\lambda}{\sqrt{4\pi}} \exp(n\lambda^2/2), \tag{3.15}$$

for $r \gg \lambda$ whereas for distances $r \sim \lambda$ the correlations are still Gaussian like in Equation 3.12. From this we can conclude that the first order correlation function of an ideal Bose gas changes from a short range correlated Gaussian in the non-degenerate case to an exponential decay in the degenerate regime even without a phase transition. We further see, that if $n\lambda^2$ increases, the correlation length $l \propto \exp(n\lambda^2/2)$ will grow exponentially. This is important, since in finite size systems for any large fixed system size L the correlation length l can be larger than L for a low enough non-zero temperature meaning that quasi long range order will be established in the whole system.

3.2.2. Harmonically trapped non-interacting bosonic quantum gases

Since we already introduced Bose gases in a harmonic 3d confinement in Section 2.2, we just summarize in this section the most important quantities for the description of a 2d quantum degenerate Bose gas at $T = 0$.
From Equation 2.7 we obtain the density of states for a harmonically trapped system in $d = 2$ dimensions

$$g(\epsilon) = \frac{\epsilon}{(\hbar\omega_r)^2}, \tag{3.16}$$

where $\omega_r = \sqrt{\omega_x \omega_y}$ corresponds to the radial trap frequency. By substituting the density of states in the normalization condition given by Equation 2.9, setting $\mu = 0$ and using the following definite integral[4]

$$\int_0^\infty \frac{x}{\exp(x) - 1} dx = \frac{\pi^2}{6}, \tag{3.17}$$

we obtain for the total atom number N

$$N - N_c = \frac{\pi^2}{6} \left(\frac{k_B T}{\hbar\omega_r}\right)^2, \tag{3.18}$$

where N_c describes the number of particles which are condensed in the single-particle ground state. As mentioned in the previous section, due to the harmonic potential the system becomes finite and a macroscopic occupation of the ground state for $N >$

[4]Here we substituted again $x = \beta\epsilon$.

$N_c^{(id)} = \frac{\pi^2}{6}\left(\frac{k_B T}{\hbar\omega_r}\right)^2$ takes place. Here $N_c^{(id)}$ corresponds to the critical atom number for a fixed temperature T. The same argumentation holds for a fixed atom number N in the trap and decreasing the temperature $T < T_c$. Here the critical temperature T_c in two dimension can be obtained by [Dyk10]

$$T_c = \sqrt{6N}\frac{\hbar\omega_r}{\pi k_B}, \tag{3.19}$$

and thus the condensate fraction can be written similar to the 3d case as

$$\frac{N_c}{N} = 1 - \left(\frac{T}{T_c}\right)^2. \tag{3.20}$$

Nevertheless, condensation in 2d differs from the condensation in 3d and it is in general a more complicated process.

3.2.3. Harmonically trapped interacting bosonic quantum gases

To see when either the BKT phase transition or the BEC transition occurs in an interacting Bose gas, we will use here first a mean-field approach to motivate the curves depicted in Figure 3.4. Since the mean-field approach is only valid in the low density regime we present further numerical results from a more accurate Monte Carlo analysis.
As shown in [Pit03, Pet02], repulsive interactions can be introduced in a mean-field Hartree-Fock approach by adding $2gn(r)$ to the external potential V(r). Using the local density approximation (LDA) we can write the local chemical potential as

$$\mu(r) = \mu - (V(r) + 2gn(r)). \tag{3.21}$$

Since we know the form of the global density $n = -\lambda^{-2}\ln(1-\exp(\beta\mu))$ from Equation 3.8, we obtain the local density $n(r)$ by substituting $\mu(r)$. The total atom number N can be calculated by integrating over the local density n(r)

$$N = \int n(r)d^2r = -\lambda^{-2}\int \ln(1 - Z\exp(-\beta V(r) - \tilde{g}D(r)/\pi))2\pi r dr, \tag{3.22}$$

where we used the fugacity $Z = e^{\beta\mu}$ and the phase space density $D(r) = n(r)\lambda^2$. Choosing the harmonic trapping potential $V(r) = \frac{1}{2}m\omega^2 r^2$ and substituting $R = r/r_T$ with $r_T^2 = k_B T/m\omega^2$ leads to

$$\frac{N}{N_c^{(id)}} = \frac{6}{\pi^2}\int_0^{+\infty} D(R)RdR, \tag{3.23}$$

which was related to the critical atom number for a BEC in an ideal gas $N_c^{(id)}$ from Equation 3.19 at a fixed temperature T. The phase space density $D(R)$ is the solution of

$$D(R) = -\ln(1 - Z\exp(-R^2/2 - \tilde{g}D(R)/\pi)), \tag{3.24}$$

which depends only on the interaction strength $\tilde{g}$ and the fugacity Z. Since the phase transition will occur first at the point of highest density in the trap, we will focus now on the phase-space density at $R = 0$. Figure 3.4 a) shows the mean-field prediction for the phase space density $D(0)$ in the center of the trapping potential for various interaction strength $\tilde{g}$ as a function of total atom number $N/N_c^{(id)}$. As can be seen in Figure 3.4, $D(0)$ increases monotonically for larger N and further increases slower for larger repulsive interaction. We assume that the BKT transition will occur when the

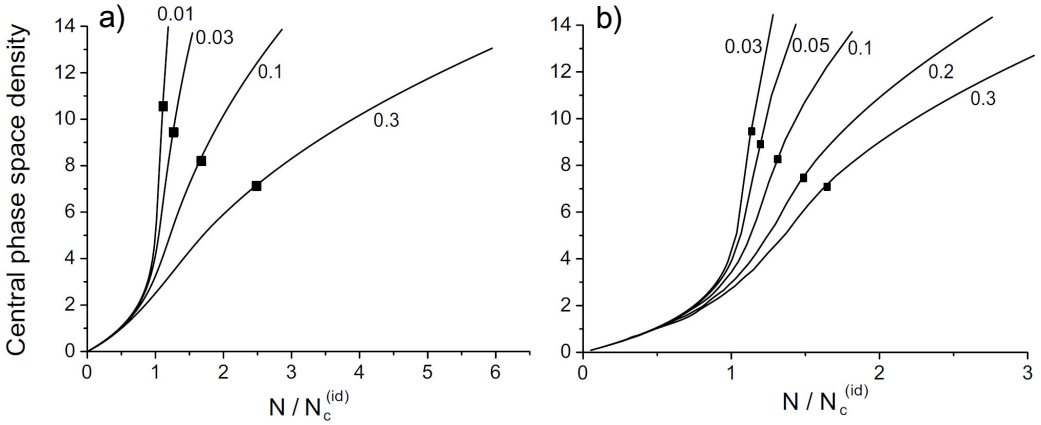

Figure 3.4.: **Phase space density D(0) in the center of a harmonic trap.** Here D(0) is depicted as a function of the total atom number N normalized by the critical atom number $N_c^{(id)}$ for a BEC transition in an ideal gas. Further the interaction strength $\tilde{g}$ was tuned and is given for each curve. The black squares label the points of the BKT transition, thus where $D(0) = D_{BKT}$. In a) the results of a mean-field Hartree-Fock approach are shown and the curves in b) result from a numerical Monte Carlo analysis. The plots are taken from [Had11].

phase space density exceeds the critical value D_{BKT} at the trap center predicted for a uniform system to be

$$D_{BKT} = (n\lambda^2)_{BKT} = \ln(C/\tilde{g}), \tag{3.25}$$

with $C = 380 \pm 3$ [Pro01]. In Figure 3.4 the point where $D(0)$ is equal to D_{BKT} is label by the black squares. The definition of the critical phase space density D_{BKT} allows further to estimate the number of atoms which has to be placed in the trap to reach the BKT regime. It can be approximated by [Hol08]

$$\frac{N_{BKT}}{N_c^{(id)}} = 1 + \frac{3\tilde{g}}{\pi^3} D_{BKT}^2, \tag{3.26}$$

which shows, that for a fixed trap and fixed temperature one needs to place a larger atom number in the trap the reach the BKT regime than the regime of ideal gas Bose-Einstein condensation.
As mentioned in the beginning of this section, the mean-field description is only valid in the low density regime where density fluctuations are still dominant. As we will show in Section 3.4.1 these fluctuations will be suppressed in the degenerate regime. Thus, a more accurate description of $D(0)$ is given by the numerical results from a classical field Monte Carlo analysis [Pro02] shown in Figure 3.4 b). This analysis has been shown to be valid even in the regime of relatively large interactions [Hol10]. The obtained curves are qualitatively similar to the results of the mean-field description, but lead to a reduction of the critical atom number $N_{BKT}/N_c^{(id)}$ as seen on the x-axis. This raises the question if the ideal BEC transition or the BKT-driven condensation comes first when increasing the phase space density at fixed interaction strength $\tilde{g}$. Due to the inhomogeneous density profile this question is hard to answer. It depends on the critical phase space density for an ideal BEC transition D_{BEC}, which can in principle be lower than D_{BKT} for some particular interaction $\tilde{g}$. In this case the ideal gas BEC transition would come first and BKT transition would not occur at all. However, D_{BEC} is not universal and depends on the parameters of the trapping potential. Please notice the fact, that Figure 3.4 could be interpreted in the way that at $N/N_c^{(id)} = 1$ the phase transition into a BEC occurs and thus the necessary phase space density for the BKT-transition would never be reached in this regime. This is misconstrued since due to the repulsive interaction the phase space density in the center of a harmonic trap for an interacting system is lower as the phase space density of an ideal gas. This leads to the fact, that the critical atom number $N_c^{(int)}$ for an interacting system is in general higher than $N_c^{(id)}$.

3.2.4. Harmonically trapped non-interacting fermionic quantum gases

In this section the most important parameter for a quasi-2d non-interacting Fermi gas are summarized and the critical atom number to conform $E_F < \hbar\omega_z$ is estimated.
Using the two dimensional density of states given in Equation 3.16 and performing the integration as in Section 2.2.1 leads to the following relation of the Fermi energy

$$E_{F,2D} = \sqrt{2N}\hbar\omega_r. \tag{3.27}$$

Substituting $E_F = k_B T_F$ in terms of the Fermi radius given by $r_{i,F} = \sqrt{(2k_B T_F)/(m\omega_i^2)}$, we obtain

$$r_{i,F,2D} = (8N)^{1/4}\sqrt{\frac{\hbar}{m\omega_r}}\frac{\omega_r}{\omega_i}. \tag{3.28}$$

Since fermions obey the Pauli principle, the critical atom number to fulfill the 2d-ness condition $E_F < \hbar\omega_z$ for a non-interacting Fermi gas can be calculated by counting

the number of microstates in a harmonic oscillator up to the energy level of the first transverse excited state. The quantized energy spectrum of the lowest 2d harmonic oscillator state is defined by

$$E_{gs} = \left(n_x + \frac{1}{2}\right)\hbar\omega_x + \left(n_y + \frac{1}{2}\right)\hbar\omega_y + \frac{1}{2}\hbar\omega_z, \tag{3.29}$$

where $n_z = 0$. Since our optical potential providing the two dimensional confinement is planed with an aspect ration of $1 : 1 : 300$ we can assume $\omega_x = \omega_y = \omega_r$ and the ground state can be written as

$$E_{gs} = (n_r + 1)\,\hbar\omega_r + \frac{1}{2}\hbar\omega_z, \tag{3.30}$$

with $n_x + n_y = n_r$. Analogous we can evaluate the energy of the first transverse excited state E_{ex} with $n_r = 0$ and $n_z = 1$. With the assumption $E_{ex} > E_{gs}$ we can write further

$$\hbar\omega_r + \frac{3}{2}\hbar\omega_z > (n_r + 1)\,\hbar\omega_r + \frac{1}{2}\hbar\omega_z, \tag{3.31}$$

which simplifies to

$$\omega_z > \omega_r n_r. \tag{3.32}$$

Introducing the trap aspect ratio $\lambda = \omega_z/\omega_r$ leads to the equation

$$\lambda > n_r. \tag{3.33}$$

Based on this equation and including degeneracies we can count the microstates in the radial direction and thus obtain the critical number of atoms N_{2D} by [Dyk11]

$$N_{2D} = \sum_{n_r=0}^{\lambda-1}(n_r + 1) = \left(\frac{\lambda^2 + \lambda}{2}\right) \tag{3.34}$$

Hence, for our characteristic trap parameters (trap depth = 2.5V see Figure 4.11) $\omega_z = 2\pi \times 5972\text{Hz}$ and $\omega_r = 2\pi \times 18.7\text{Hz}$, the maximum atom number we can load into our optical potential and fulfill the 2d-ness condition is about $N_{2D} = 51200$ per spin state.

3.3. Scattering in 2d

In this section we briefly discuss the influence of the reduced dimensionality on the scattering properties of our system and then focus on how the interactions differ from a three dimensional system.
Similar to scattering in three dimensions one can describe the scattering between two identical bosons with relative wave vector $\mathbf{k}$ starting from a slightly modified ansatz

for the wave function [Adh86]

$$\psi_{\mathbf{k}}(\mathbf{r}) \propto e^{i\mathbf{kr}} - \sqrt{\frac{i}{8\pi}} f(k) \frac{e^{ikr}}{\sqrt{kr}}. \tag{3.35}$$

For the scattering amplitude of a pure 2d system at low energies one further obtains

$$f(k) = \frac{4\pi}{\ln(1/(ka_{2D})^2) + i\pi}, \tag{3.36}$$

where the 2d scattering length a_{2D} is introduced. In contrast to the tree dimensional scattering amplitude (see Equation 2.37) the scattering amplitude in 2d exhibits always a logarithmic energy dependence.
The range of interaction is characterized by $r_0 = r_{vdW,Li} \sim 0.2$nm and is much smaller than the length scale of the axial confinement given by $l_z = \sqrt{\hbar/m\omega_z}$ which is either about 375nm for molecules or about 530nm for unbound atoms in our experiments. Hence, the relative motion of the particles is not influenced by the axial confinement and the scattering process can still be described by a modified 3d scattering amplitude. This modification has been calculated in [Pet01] and in the low energy limit $E \ll \hbar\omega_z$ the scattering amplitude of this so called quasi-2d system is given by

$$f(k) = \frac{4\pi}{\sqrt{2\pi}\frac{l_z}{a} + \ln(\frac{\alpha}{\pi(kl_z)^2}) + i\pi}, \tag{3.37}$$

with $\alpha \approx 0.915$ [Pet01] or $\alpha = 0.905$ [Vog13]. Based on that, one can conclude that the maximum of the scattering amplitude is not reached when a diverges as it is the case in three dimensions. The real part of the denominator has to become zero, which depends on the energy of the system k and the ratio between l_z and a. Thus the resonance position gets shifted with respect to the 3d Feshbach resonance, which is called a confinement-induced resonance.
In the regime of weak attractive interactions where in addition $|a| < l_z$, the form of the pure 2d scattering amplitude from Equation 3.36 can be recovered. For this purpose we rewrite the 2d scattering length defined by the universal equation $a_{2D} = \sqrt{\hbar^2/mE_{B,2D}}$ in terms of the approximated binding energy from Equation 3.4

$$a_{2D} = l_z\sqrt{0.905}\exp\left(-\sqrt{\pi/2}\frac{l_z}{a}\right), \tag{3.38}$$

which grows exponentially for $a \to -\infty$ and obtain further

$$f(k) = \frac{4\pi}{\ln(E_{B,2D}/E) + i\pi} = \frac{4\pi}{\ln(1/(ka_{2D})^2) + i\pi}, \tag{3.39}$$

where we used $E = \hbar^2 k^2/m$. Thus, the strong interaction regime which was given in the three dimensional case by $1/k|a| \ll 1$ is now rather at $|\ln(ka_{2D})| < 1$. The regime of weak interaction is then characterized by $\ln(ka_{2D}) \to +\infty$ for the BCS regime and $\ln(ka_{2D}) \to -\infty$ in the BEC case [Vog13].

The coupling strength of a two dimensional Fermi gas in the weakly interacting regime

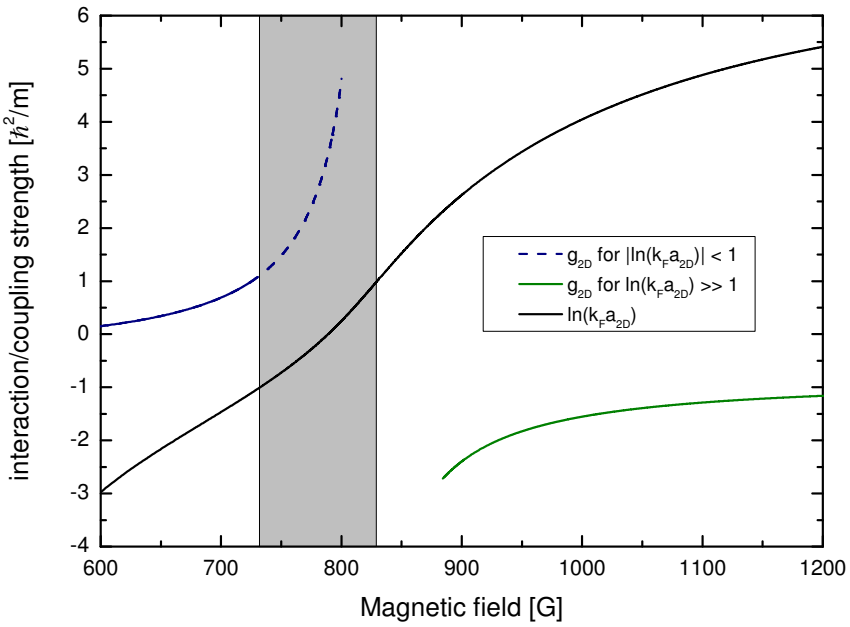

Figure 3.5.: **Coupling strengths for both weakly repulsive and weakly attractive interactions.** The 2d interaction parameter (black) $\ln(k_F a_{2D})$ is shown defining the weakly and strongly (gray) interacting regimes. Further both the coupling strength in the weakly attractive interacting regime (green) and the coupling strength in the weakly/strongly repulsive interacting regime (solid/dashed blue line) are depicted. Since the energy dependence ($k_F \approx \hbar\omega_z$) of the interaction parameter shifts the strongly interacting regime to the repulsive side, we decreased the validity regime of the coupling constant of weak repulsive interaction $\tilde{g} = \frac{m}{\hbar^2} g_{2D}$ for $\ln(k_F a_{2D}) \ll -1$ to $\tilde{g} < 1$ (see Equation 3.41). The dashed continuation stops at the point were $a \sim l_z$.

is further given by [Frö12, Blo75, Vog13]

$$g_{2D} = \frac{-2\pi\hbar^2}{m \ln(k_F a_{2D})}, \tag{3.40}$$

where we replace the general wave vector k by the Fermi wave vector k_F. This coupling describes the attractive interaction in the mean-field regime discussed in Section 2.3.2 and it is depicted in green in Figure 3.5 for the valid regime $|a| < l_z$. Since the interaction depends on the energy, we approximated $k_F \approx \hbar\omega_z$ motivated by the measurement results from Section 5.5.
In the repulsive weakly interacting regime $\ln(k_F a_{2D}) \ll -1$ the logarithmic and imaginary term in Equation 3.37 can be neglected as long as the first term in the denominator of the scattering amplitude $\sqrt{2\pi} l_z/a$ stays larger than 1. Thus, we obtain similar to the 3d case a energy independent scattering amplitude

$$f(k) \approx \sqrt{8\pi}\frac{a}{l_z} = \tilde{g}. \tag{3.41}$$

Assuming a contact potential comparable to three dimensions, the 2d interaction energy is

$$E_{int} = \frac{\hbar^2 \tilde{g}}{2m} \int n^2(\mathbf{r}) d^2 r, \tag{3.42}$$

and the characteristic length scale corresponding to the interaction energy, the so-called healing length $\xi = 1/\sqrt{\tilde{g}n}$ can be obtained.

In Figure 3.6 the magnetic field dependence of the dimensionless coupling constant $\tilde{g}$ is plotted for the bosonic regime as discussed in Figure 3.2. The curve in Figure 3.6 was calculated using the harmonic oscillator length $l_z = \sqrt{\hbar/(2m\omega_z)}$ for diatomic molecules at a trap frequency $\omega_z = 2\pi \times 5.879$ kHz. Further, the molecular scattering length $a_{dd} = 0.6a$ [Pet05] was taken into account. This coupling constant which can be written as $\tilde{g} = g_{2D} m/\hbar^2$ determines the strength of repulsive interaction in two dimensions. Thus, weakly repulsive interacting systems are defined by $\tilde{g} \ll 1$ whereas if $\tilde{g}$ is on the order of 2π the system is strongly repulsive interacting.
The strongly interacting regime is qualitatively defined by equating the kinetic energy of N non-interacting particles, which are equally distributed over the lowest N single particle states, with the mean field interacting energy of N particles. From this, one obtains the value $\tilde{g} = 2\pi$ for the regime of a strongly correlated many-body ground state [Had11]. Further holds this value only in the low energy limit $k_F \propto E_F < \hbar\omega_z$. We enter this strong coupling regime in the low energy limit at about 800G (see Figure 3.6) where $l_z \sim a_{dd}$ and $\tilde{g} \sim 5.0$. This is already close to the 3d Feshbach resonance thus the fermionic nature of our weakly bound molecules start to become relevant.
As seen in Figure 3.5 the regime of strong interactions gets shifted towards the repulsive side if $k_F \approx \hbar\omega_z$ and decreases the validity of the coupling constant $\tilde{g}$ depicted in blue. Since we perform most of our experiments at 692G, we obtain $\tilde{g} \approx 0.6$ which is not small compared to 1 and hence we are not really in the weakly interacting regime anymore. In the vicinity of a Feshbach resonance a increases and can become on the order of l_z (blue dashed continuation in Figure 3.5). Now the logarithmic term in Equation 3.37 dominates and the coupling strength becomes more complicated.

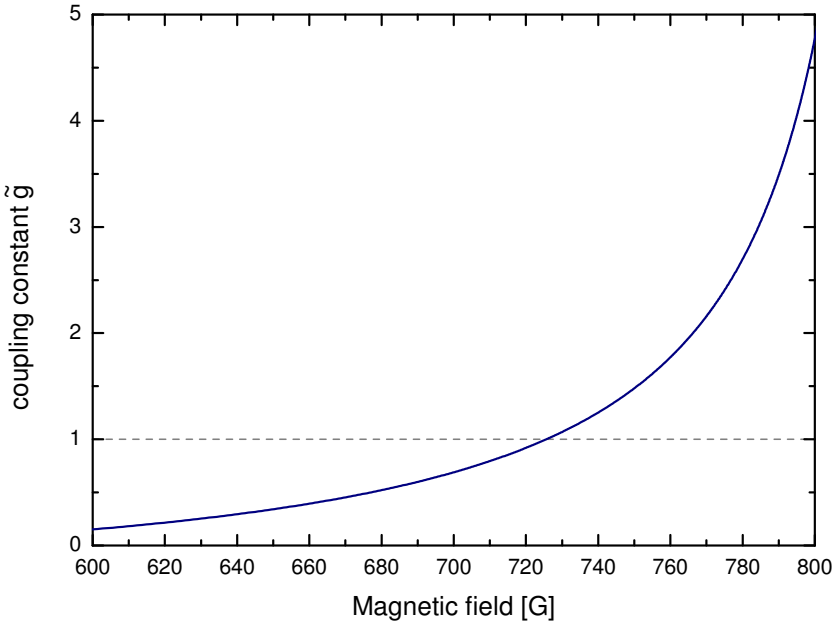

Figure 3.6.: **Dimensionless coupling constant for a weakly repulsive interacting quasi-2d system in the low energy limit.** The blue curve shows the increase of $\tilde{g}$ with increasing magnetic field in the bosonic regime $E_B > \hbar\omega_z$. $\tilde{g}$ was calculated using the $^6Li_2$ mass in the harmonic oscillator length and the 3d dimer-dimer scattering length a_{dd} for the $|1\rangle - |2\rangle$ mixture.

3.4. Mechanisms and characteristics of the Berezinskii-Kosterlitz-Thouless transition

After introducing the different quantum statistics and scattering properties of a quasi-2d system, we want to describe in this section the mechanisms and characteristics of the BKT transition predicted for a quasi-2d system in more detail.
We will see, that the BKT phase transition only depends on the phase fluctuations of the order parameter $\Psi = \sqrt{n}\exp(i\theta)$. The suppression of the phase fluctuations in the BKT phase leads to the algebraic decay of the already introduced first order correlation function $g_1(r)$ and thus to a quasi-long rang order in the system. Thus, we start by motivating the suppression of the density fluctuations for a BEC at $T = 0$.

3.4.1. Suppression of density fluctuations for repulsive interaction

As discussed in the previous sections, Bose-Einstein-Condensation can occur in finite two dimensional systems for very low temperatures. Thus, at $T = 0$ we can describe a weakly interacting 2d Bose gas by a constant macroscopic wave function given by

$$\psi = \sqrt{n}e^{i\theta}, \tag{3.43}$$

here n and θ are classical fields which for any finite temperature will thermally fluctuate. The interaction energy of this repulsively interacting system ($g_{2D} > 0$) can be written as

$$E_{int} = \frac{g_{2D}}{2}\int n^2(\mathbf{r})d^2r = \frac{g_{2D}}{2L^2}\langle n^2(\mathbf{r})\rangle, \tag{3.44}$$

where we used $g_{2D} = \tilde{g}\hbar^2/m$ as the interaction strength. Since the density fluctuations $(\delta n)^2$ for a fixed average density $n = \langle n(\mathbf{r})\rangle$ are defined as

$$(\delta n)^2 = \langle n^2(\mathbf{r})\rangle - n^2, \tag{3.45}$$

it becomes clear that in order to minimize E_{int} the density fluctuations $(\delta n)^2$ in $\langle n^2(\mathbf{r})\rangle = (\delta n)^2 + n^2$ should be minimal. As motivated in [Had11], the density fluctuations are strongly suppressed if the density of states $D_{2D} \gg 2\pi/\tilde{g}$. Numerical calculations [Pro01] have shown that a significant suppression is already reached for $D_{2D} \gg 1$.

3.4.2. The Bogoliubov spectrum

To motivate the fact that long wavelength phonons are the origin of the quasi long range order, we start with a brief summary of a Bogoliubov analysis near $T = 0$ for a weakly interacting Bose gas which can be described by $\psi(\mathbf{r}, t) = \sqrt{n(\mathbf{r}, t)}e^{i\theta(\mathbf{r},t)}$. We introduced here the local density $n(\mathbf{r}, t)$ and the local phase $\theta(\mathbf{r}, t)$ motivated in the beginning of the section. In the subsequent calculation we follow the more detailed argumentation of [Had11].
From Bogoliubov theory we can determine the Hamiltonian

$$H = nL^2\sum_{\mathbf{k}}\left[\frac{\hbar^2k^2}{2m}|c_{\mathbf{k}}|^2 + \left(\frac{\hbar^2k^2}{2m} + 2gn\right)|d_{\mathbf{k}}|^2\right], \tag{3.46}$$

where L corresponds to the linear size of the system, g to the 2d coupling constant and n to the global density. $c_{\mathbf{k}}$ and $d_{\mathbf{k}}$ are time-dependent Fourier coefficients related to the phase fluctuation and density fluctuation respectively. From the Hamiltonian the following set of coupled equations of motion for $\mathbf{k} \neq 0$ can be derived

$$\dot{c}_{\mathbf{k}} = -\left(\frac{\hbar k^2}{2m} + \frac{2gn}{\hbar}\right)d_{\mathbf{k}}, \tag{3.47}$$

$$\dot{d}_{\mathbf{k}} = \frac{\hbar k^2}{2m} c_{\mathbf{k}}, \tag{3.48}$$

From $\mathbf{k} = 0$ the time evolution of the global phase of the gas can be obtained since $\dot{c}_0 = -gn/\hbar$. For each $\mathbf{k}$ in the summation, the Hamiltonian exhibits a harmonic-oscillator like form and the eigenfrequencies are given by

$$\omega_k = \sqrt{\frac{\hbar k^2}{2m}\left(\frac{\hbar k^2}{2m} + \frac{2gn}{\hbar}\right)}. \tag{3.49}$$

This is known as the Bogoliubov excitation spectrum. By expanding the square root in the dispersion relation for large k, one finds

$$\omega_k \approx \frac{\hbar k^2}{2m}\left(1 + \frac{2mgn}{\hbar^2 k^2}\right) = \frac{\hbar k^2}{2m} + \frac{gn}{\hbar}, \tag{3.50}$$

which corresponds to free particle eigenmodes. In contrast one can neglect 4th order terms for small k and thus the eigenmodes can be related to long-wavelength phonons since $w_k = ck$ with $c = \sqrt{gn/m}$. The crossover between both regimes is at $k \sim 1/\xi = \sqrt{\tilde{g}n}$.
To give a qualitative argument why the phonons imply only phase fluctuations one can use the virial theorem $\langle m\omega^2 x^2\rangle = \langle p^2/m\rangle$ since it holds for the harmonic oscillator in thermal equilibrium and $|c_{\mathbf{k}}|^2$, $|d_{\mathbf{k}}|^2$ correspond to conjugated, dimensionless variables. Hence, from the Hamiltonian in Equation 3.46 we can obtain the following relation

$$\frac{\langle |d_{\mathbf{k}}|^2\rangle}{\langle |c_{\mathbf{k}}|^2\rangle} = \frac{\hbar^2 k^2/2m}{\hbar^2 k^2/2m + 2gn}. \tag{3.51}$$

For $k \to 0$ one can follow, that $\langle |d_{\mathbf{k}}|^2\rangle \ll \langle |c_{\mathbf{k}}|^2\rangle$. This means that density fluctuations are suppressed for long-wavelength phonons ($k = 2\pi/\lambda$) whereas the free particle eigenmode (large k) involves both phase and density fluctuation. Moreover, the suppression of density fluctuations occurs on a length scale $r > \xi$ and depends on the interaction parameter g as mentioned in the section before [Had11].

3.4.3. Algebraic decay of the correlation function

In Section 3.2.1 we introduced the first-order correlation function $g_1(r) = \langle \psi^*(\mathbf{r})\psi(0)\rangle$ as a measure for long range order. For distances $r > \xi, \lambda$ the density fluctuations are suppressed as seen from the previous section and the Hamiltonian from Equation 3.46 is reduced to the phase fluctuation part. From the classical equipartition theorem we know that each variable which is quadratic in the Hamiltonian adds $k_B T/2$ to the

energy, thus the contribution of the phononic part can be approximated by

$$n_s L^2 \frac{\hbar^2 k^2}{2m} \langle |c_k|^2 \rangle = \frac{k_B T}{2}, \tag{3.52}$$

n_s is here related to the uniform superfluid density which is slightly smaller than n. Substituting n by n_s for large r is a heuristic way to include the short distance physics [Had11]. To calculate the first-order correlation function we use again $\psi(\mathbf{r}) = \sqrt{n_s} e^{i\theta(\mathbf{r})}$ as an ansatz for the wave function without density fluctuations. Thus, we can write $g_1(r)$ as

$$g_1(r) = n_s \left\langle e^{i(\theta(\mathbf{r}) - \theta(0))} \right\rangle. \tag{3.53}$$

By expanding the phase in Fourier series $\theta(\mathbf{r}, t) = \sum_{\mathbf{k}} c_{\mathbf{k}}(t) e^{i\mathbf{kr}}$ the phase difference can be expressed in terms of the Fourier coefficients $c_{\mathbf{k}}(t)$ which we already introduced in the Hamiltonian

$$\theta(\mathbf{r}) - \theta(0) = \sum_{\mathbf{k}} c'_{\mathbf{k}} (\cos(\mathbf{kr}) - 1) - c''_{\mathbf{k}} \sin(\mathbf{kr}). \tag{3.54}$$

Here $c_{\mathbf{k}} = c'_{\mathbf{k}} + i c''_{\mathbf{k}}$ and from Equation 3.52 we obtain

$$\langle |c'_{\mathbf{k}}|^2 \rangle = \langle |c''_{\mathbf{k}}|^2 \rangle = \frac{\pi}{n_s \lambda^2 L^2 k^2}. \tag{3.55}$$

We assumed that $c'_{\mathbf{k}}$ and $c''_{\mathbf{k}}$ are fluctuating independently, thus $\langle c'_{\mathbf{k}} c''_{\mathbf{k}} \rangle = 0$ and further a correlation between the modes $\mathbf{k}$ and $\mathbf{-k}$ exists because θ is real which implies $c'_{\mathbf{k}} = c'_{\mathbf{-k}}$ and $c''_{\mathbf{k}} = -c''_{\mathbf{-k}}$. Using the fact, that for independent Gaussian variables the expectation value can be rewritten like $\langle e^{ix} \rangle = e^{-\frac{1}{2}\langle x^2 \rangle}$ and transforming the discrete sum into $L^2/(4\pi^2) \int d^2k$ leads to the form

$$g_1(r) = n_s \exp\left(-\frac{1}{2\pi n_s \lambda^2} \int \frac{1 - \cos(\mathbf{kr})}{k2} d^2k \right). \tag{3.56}$$

Since we restrict our evaluation to the phonon part, the upper bound of the integral is given by $k = 1/\xi$ and the main contribution is related to modes with $k > 1/r$ [Had11]. By calculating the integral

$$\int \frac{1 - \cos(\mathbf{kr})}{k2} d^2k = 2\pi \ln\left(\frac{r}{\xi}\right), \tag{3.57}$$

we obtain the final result for the first-order correlation function

$$g_1(r) = n_s \left(\frac{\xi}{r}\right)^{1/n_s \lambda^2}, \tag{3.58}$$

which delivers insight into the algebraic decaying correlation for large distances r. The fact that $g_1(r) \to 0$ for $r \to \infty$ and thus the absence of true long range order, is a consequence of the Mermin-Wagner theorem. The slow decay of correlations permits a system with a so called 'quasi-long-rang order' and a superfluid state with suppressed density fluctuations can be called a superfluid 'quasi-condensate', since the phase is not constant for each r [Pet04a].
Thus, in the last two sections we identified the long-wavelength phonons as one origin of the quasi-long range order in a quasi-2d system. In the next section we will focus on the algebraic exponent and will give reasons why it is never larger than 1/4 in the superfluid state. Further we will introduce the concept of vortices which will allow us to define a critical transition point where the phase transition from the normal phase into the BKT phase occurs.

3.4.4. BKT transition in a two dimensional Bose gas

So far we have seen, that on both sides of the transition no true long range order can be established because of the exponential decay of $g_1(r)$ in the normal state motivated in Section 3.2.1 and the algebraic decay of $g_1(r)$ in the superfluid state due to long-wavelength phonons. But just from a phononic point of view, it is not possible to find a critical transition point, because the phonons will influence the long range order at any non-zero temperature since the exponent grows smoothly with temperature.
A microscopic theory of the superfluid transition in 2d was developed by Berezinskii [Ber71], Kosterlitz and Thouless [Kos73] (see [Min87] for review) and since the transition occurs in a quantum degenerate regime in which, as seen before, the density fluctuations are significantly suppressed the transition can just be driven by phase fluctuations. Therefore, one of the key aspects of the BKT theory is the appearance of a second source of phase fluctuations, so-called vortices.
Vortices are singularities in the superfluid density around which the phase θ changes by a multiple of 2π. Since we are in the ultracold regime, we can assume just vortices with phase windings of $\pm 2\pi$ as energetically stable, where the sign corresponds to the sense of rotation around the vortex. To each single vortex one can assign a velocity field $\mathbf{v} = \hbar\nabla\theta/m$ which varies as $\hbar/mr$ because the phase only depends on the azimuthal angle φ. The size of the vortex is determined by the healing length ξ which is consistent with the assumption that density fluctuations are suppressed on a length scale $r \gg \xi$. In this vortex picture the microscopic mechanism of the superfluid to normal phase transition can be explained as seen in Figure 3.7.
For $T < T_{BKT}$ the vortices form pairs with opposite circulations, which can be compared to dipole like structures. These pairs do not create any effective circulation along closed contours larger than the size of each pair which would be on the order of ξ for tightly bound pairs. Hence, they will influence the phase θ and the corresponding velocity field just at distances $r < \xi$. The behavior of $g_1(r)$ is therefore unaffected at large distances $r > \xi$. For $T > T_{BKT}$ the size of the vortex pairs grows, until separation and proliferation of single free vortices takes place. They form a disordered gas of phase

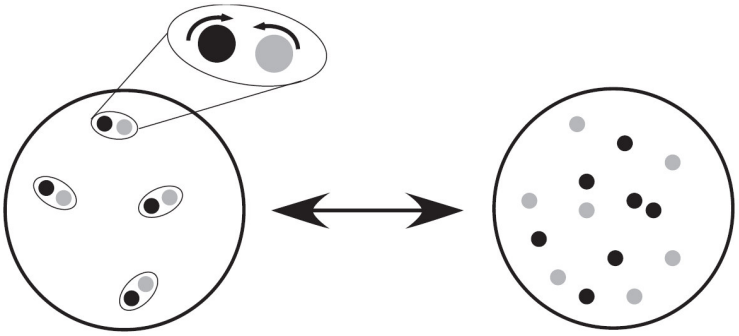

Figure 3.7.: **Transition between superfluid (left) and normal phase (right) as explained in BKT theory.** As temperature increases, the size and density of the vortex pairs with opposite circulations (left) grows. When the distance between several pairs becomes comparable to their size, they start to overlap leading to unbound pairs and proliferation of free vortices. Above T_{BKT} (right) only free vortices are left destroying the quasi long range order and the superfluid density vanishes. The picture was taken from [Had11].

defects and scramble the phase at every length scale, destroying the quasi long range order in the system.
Increasing the temperature further, leads to a regime where the suppression of density fluctuation is no longer valid and the concept of individual vortices is no longer the dominant effect in the system. In the introduction to this section we already mentioned, that the superfluid phase transition is related to some kind of topological order in the system. Since the vortex pairs are topologically annihilated for large enough contours one can refer to the system as topologically ordered for $T < T_{BKT}$. For $T > T_{BKT}$ the free vortices affect the phase θ at arbitrary large distances because an arbitrary large closed contour around free vortices will in general not contain equal number of vortices with opposite circulations. Hence, one can call a superfluid quasi-condensate in the absence of free vortices topologically identical to a BEC with true long range order, whereas a system containing free vortices is on every length scale topologically different from a BEC [Had11]. T_{BKT} is here a well determined transition point at which the superfluid density n_s exhibits a universal jump which will be discussed now.

Since the full theoretical derivation of the universal jump in the superfluid density is rather complicated involving renormalization group arguments, we want to give here a simple physical picture how vortices drive the BKT transition [Had11]. The existence of the universal jump in the superfluid density was described theoretically by Nelson and Kosterlitz in [Nel77] and first experimental certification was achieved by Bishop and Reppy [Bis78] in an experiment with liquid ^{4}He films.
Let us consider a superfluid with finite density n_s and assume a circular geometry with the system size $R \to \infty$. A good estimation for the energy E of a single vortex sitting

at the origin affecting only the superfluid density is given by

$$E = \int_{\xi}^{R} \frac{1}{2} n_s \left(\frac{\hbar}{mr}\right)^2 d^2r = \frac{\hbar^2\pi}{m} n_s \ln\left(\frac{R}{\xi}\right). \tag{3.59}$$

The density in the normal phase n has disordered phases and is therefore not affected by the presence of a single vortex. Further, we can approximate the entropy S associated with a single vortex core, which is given by the number of possible positions to find a vortex with radius ξ in a circle with radius R

$$S = k_B \ln\left(\frac{R^2\pi}{\xi^2\pi}\right) = 2k_B \ln\left(\frac{R}{\xi}\right). \tag{3.60}$$

Neglecting edge effects, the free energy $F = E - TS$ can be written down as

$$\beta F = \frac{1}{2}(n_s\lambda^2 - 4) \ln\left(\frac{R}{\xi}\right). \tag{3.61}$$

From this equation we can conclude, that the free energy changes sign if $n_s\lambda^2 = 4$, which defines the transition temperature T_{BKT}. If $n_s\lambda^2 > 4$ the free energy is positive and the superfluid is stable, meaning that no free vortices are created, whereas for $n_s\lambda^2 < 4$ the free energy F is negative and proliferation of free vortices occurs. The first free vortices lead to a reduction of the superfluid density which makes the appearance of further free vortices even more favorable. Because of this avalanche effect, n_s is instantaneously decreased to 0 leading to the universal jump in the superfluid density from $n_s = 0$ for $T > T_{BKT}$ to $n_s = 4/\lambda^2$ for $T < T_{BKT}$. This differs from the 3d case where the superfluid density grows smoothly.
Nevertheless, $n_s\lambda^2 = 4$, which surprisingly is independent of the interactions $\tilde{g}$, is not sufficient to determine T_{BKT} for a given system. Taking the short distance physics into account one can calculate the critical phase-space density as mentioned before for weak interactions $\tilde{g} \ll 1$ [Fis88, Pro01, Pro02]

$$D_{BKT} = (n\lambda^2)_{BKT} = \ln(C/\tilde{g}), \tag{3.62}$$

with $C = 380 \pm 3$ determined by Monte Carlo simulations [Pro01]. At the transition point the density of the normal phase n is larger than the superfluid density n_s. Thus $n\lambda^2 > n_s\lambda^2 = 4$ holds and D_{BKT} has to be larger than 4 which leads to an interaction strength of $\tilde{g} < 7$.
After this brief theoretical overview over the properties of a quasi-2d quantum system and the introduction of the BKT transition, we will describe our experimental setup in the next chapter.

4. Experimental setup and techniques

In this chapter we give an overview over our experimental setup and the techniques we are using to form and investigate a quantum degenerate system. Section 4.1 will introduce you to the vacuum system and the experimental chamber. The different techniques of trapping and cooling of a cloud of ^{6}Li atoms down to the quantum degenerate regime are described in the Sections 4.2 and 4.3. In Section 4.4 we present our setup to create highly anisotropic dipole traps and we will close this chapter in Section 4.5 by introducing our imaging technique.

4.1. Vacuum setup, oven and experiment chamber

All our experiments have to be conducted in ultra high vacuum (UHV) in order to avoid loss of atoms by collisions with the thermal background gas. In Figure 4.1 the vacuum setup is schematically shown and the different parts of the experiment are visible.
The pressure in the octagonal experiment chamber of $P_{exp} \leq 10^{-11}$mbar is provided by a titanium sublimation pump (VARIAN) and to pump non-reactive gases like He or Ar an additional ion-pump (VARIAN StarCell 75) is connected to the experiment. To achieve best performance inside the experiment chamber, the experiment chamber itself is coated with a 'Non Evaporative Getter coating' (NEG), which consists of a TiZrV alloy. Similar to the Titanium sublimation pumps it acts as a getter surface and avoids outgassing from the octagon walls. The vacuum does not limit the lifetime of our prepared atoms since we measured the lifetime of atoms trapped in a highly anisotropic dipole trap to be about 50s [Nei13]. Due to the fact that the time scale of one experiment cycle is about $\sim$ 12s, we are limited by neither beam power fluctuation nor losses via background gas collisions. One experiment cycle can be briefly subdivided into: 4s loading of the magneto-optical trap (MOT), 5s transfer to the optical dipole trap (ODT) with evaporation and 3s transfer to the pancake trap with imaging. We had to increase the MOT loading time to 4s due to the decreased power in our TA (tapered amplifier) laser system (Toptica Photonics) providing the trapping light for the MOT.
The preparation of ^{6}Li atoms takes place in the oven chamber which is pumped by a second titanium sublimation pump (VARIAN) and a smaller ion-pump (VARIAN StarCell 40) down to $P_{oven} \approx 3 \cdot 10^{-11}$mbar. The oven chamber is connected to the experiment chamber via the Zeeman slower which acts as a differential pumping stage to suppress any negative effect due to the higher pressure in the oven chamber and will be discussed later in more details. The oven in the oven chamber operates at $T_{oven} = 350$°C

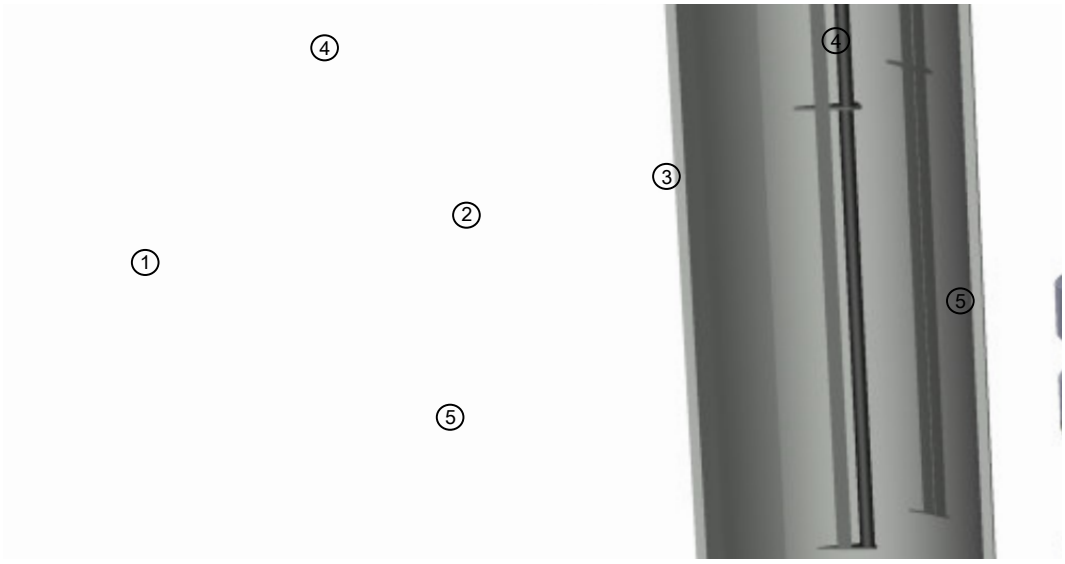

Figure 4.1.: **The vacuum setup.** The ^{6}Li atoms are produced by heating Lithium up to $T = 350$°C in an oven placed at (1). In the Zeeman slower (2) the atoms get decelerated down to the capture velocity of the MOT which is formed in the experiment chamber (3) by six slightly red-detuned laser beams (red arrows). The trapped atoms are then further transferred into optical dipole trap potentials to perform e.g. evaporative cooling. Optical access is achieved by six viewports on the side of the spherical octagon and two viewports from below and above. The ion pumps (5) are connected to the experiment via the two towers (4) which provide the gettering surface for the titanium sublimation pumps. The picture is adapted from [Wen13]

which leads to evaporation of ^{6}Li atoms since the melting point is around $T \approx 180$°C. The atom beam can be blocked by a mechanical shutter (black flag in Figure 4.1) which can be rotated into the beam path.
The heart of the vacuum setup is the experiment chamber. To prevent any unwanted magnetization it is made of non-magnetic steel and formed like a spherical octagon which allows us to optically access the atoms through six viewports in the horizontal plane and two viewports from below and above. In Figure 4.1 the red arrows correspond to the resonant laser beams of the magneto-optical trap (MOT). The beam for further trapping in an optical dipole trap enters the experimental chamber from the front viewport and is reflected back under a small angle.
Besides that, we are able to image the atomic cloud from the front viewport, both side viewports and from above as can be seen in Figure 4.5. The theoretical maximal achievable resolution is given by the Rayleigh criterium and the numerical aperture of the viewports. For the side viewports $NA_{hor} = 0.15$ and the resolution is given by $d_{min,hor} = 0.61\lambda/NA = 2.78\mu$m for $\lambda = 671$nm [Nei13]. Since the vertical viewports are closer to the atomic cloud in the center of the chamber they have a larger

numerical aperture of $NA_{vert} = 0.88$ which leads to a higher theoretical resolution of $d_{min,vert} = 465$nm. To access the higher resolution from above, a new objective with a numerical aperture of $NA = 0.6$ was designed in our group [Ser11, Ber13] and build up in a bachelor thesis [Kri13]. By testing the new objective a resolution of $d_{min} = 0.68\mu$m was achieved for $\lambda = 671$nm and $d_{min} = 1.08\mu$m for $\lambda = 1064$nm respectively.
The two large red rings on the experiment chamber (see Figure 4.1) correspond to the MOT coils which are in anti-Helmholtz configuration and form a quadrupole field which is necessary for magneto-optical trapping as will be discussed later. They are powered by a Delta Elektronika (SM $45-70$D) power supply which provides a current up to 70A. Each of the coils consists of four stacked coils with 25 windings each and is glued to a water cooled copper heat sink. The current direction of both coils, thus the magnetic field configuration, can be changed, which allows us to use the MOT coils as a compensation for gravity in the experiment.
As pointed out earlier the interactions between the atoms can be tuned by a homogeneous magnetic offset field. We apply this field by the so-called Feshbach coils depicted as the smaller green rings in Figure 4.1. They are placed close to the atoms in nearly Helmholtz configuration, so that we need just 30 windings at a current of 200A to produce fields of the order of 1400G. This accelerates the switching progress compared to the MOT coils because the inductivity is reduced. Due to the high current they are glued to water cooled copper heat sinks as well (brown).
The advantage of the nearly Helmholtz configuration is that one creates a small magnetic field saddle which leads for high field seeking states to a weak magnetic anti-confinement in vertical direction whereas in horizontal direction an additional magnetic confinement is been established which supports the optical trapping of the optical dipole trap (ODT) along the ODT beam axis where the optical confinement is the weakest. The asymmetry of the magnetic field due to the current connectors (brown arm) is compensated by small blocks of ferromagnetic steel which are placed directly on the heat sink. We measure the current through the coils by a Danfysik Ultrastab 866 current transducer and for magnetic field stabilization we use a PID-feedback loop to regulate the voltage of the Delta Electronika (SM $30-200$) power supply which will be discussed later. A more detailed discussion of the vacuum chamber the oven and the MOT coils producing the magnetic fields can be found in [Rie10].
In the next sections the mechanisms of optical trapping and cooling of a sample of ^{6}Li atoms in the experiment chamber will be discussed.

4.2. Trapping and Doppler cooling of a cloud of ^{6}Li atoms

As mentioned above, the heated atoms leave the oven with a thermal longitudinal velocity of $\bar{v} = \sqrt{\frac{8k_BT_{oven}}{\pi m_{^6Li}}} \approx 1500$m/s. In order to trap these beam of atoms in a magneto-optical trap (MOT) we have to decrease the mean velocity of the atoms down

to the capture velocity of our MOT which is in the range of $v_{cap} \approx 50$m/s.

Zeeman slower

This is achieved by the Zeeman slower where a red detuned laser beam which is directed towards the atomic beam leads to a deceleration of the atoms by photon recoil. The detuning is necessary since the laser photons and atoms are counter-propagating which results in a Doppler shift in the resonance frequency. This kind of laser cooling can be understood by approximating the atom as a two-level system [Met99]. If a laser photon is absorbed by the atom, the atom gains the photon momentum which is pointed against the direction of the initial momentum of the atom. Due to spontaneous emission after some characteristic lifetime τ the absorbed photon is re-emitted leading to a photon recoil which has no preferred direction. Thus, this recoil is averaged out over many events and the remaining effective recoil is the directed recoil from the absorption process leading to a deceleration of the atom. The force acting on the atom due to the scattering of photons is called the spontaneous light force and a detailed description can be found in many textbooks like [Met99]

$$\langle F_{spont} \rangle = \hbar \mathbf{k} \Gamma_{sc}, \tag{4.1}$$

here $\mathbf{k}$ corresponds to the momentum of the absorbed photon and Γ_{sc} represents the scattering rate of photons which is given by

$$\Gamma_{sc} = \frac{\frac{s_0 \gamma}{2}}{1 + s_0 + \left(\frac{2\delta}{\gamma}\right)^2}, \tag{4.2}$$

where γ is the linewidth of the excited state, δ describes the detuning of the laser frequency and $s_0 = I/I_{sat}$ corresponds to the intensity saturation. Thus, to maximize the spontaneous light force one needs both, enough intensity to saturate the transition $s_0 > 1$ and has to stay close to resonance so minimizing the detuning $\delta \to 0$. As mentioned above, the Doppler shift $\delta_{Doppler}$ leads to a red-detuned laser light δ_0. Further the velocity dependence of the Doppler shift results in the fact, that the deceleration by the spontaneous light force moves the atoms out of resonance. This can be compensated by a spatially varying magnetic field, which shifts the levels due to the Zeeman shift such, that they are in resonance at each position $\mathbf{x}$. Summing up all effects one has to satisfy the following resonance condition

$$\delta = \delta_0 + \delta_{Doppler}(\mathbf{v}) + \delta_{Zeeman}(\mathbf{x}) = \delta_0 + \mathbf{kv} - \frac{\mu_B B(\mathbf{x})}{\hbar}. \tag{4.3}$$

Since δ has to be minimized $\delta \to 0$ the spatial dependence of the magnetic field B can be calculated

$$B(z) = B_0 \sqrt{1 - \frac{z}{z_0}}, \tag{4.4}$$

with the slower length $z_0 = mv_0^2/\hbar k\gamma$ where v_0 corresponds to the maximum slowable velocity and the magnetic field at the beginning of the slower $B_0 = \hbar k v_0/\mu_B$. To minimize the additional fields of the Zeeman slower in the experiment chamber we use a decreasing field configuration. Hence, we have to be close to resonance with the laser light which can lead to unwanted excitations during trapping in the MOT. Nevertheless, this allows us to use the magnetic field of the MOT coils as the last part of the slower field which makes the Zeeman slower more compact and allows us to capture the atoms directly at the end of the slower where their expansion perpendicular to the slower axis is smaller. More detailed information according to the Zeeman slower can be found in [Sim10].

Magneto-optical trapping

Since the MOT was already discussed in many textbooks e.g. [Met99] we will focus here on the basic principles of magneto-optical trapping. More information on the performance of the MOT we use in our experiment can be found in [Rie10].
Using again the spontaneous light force F_{spont} enables us to now trap the already slowed down atoms in the experiment chamber. By adding pairs of counterpropagating slightly red detuned laser beams in each spatial direction (as seen in Figure 4.2), one achieves a velocity dependent cooling which is called optical molasses. For an atom with zero velocity the spontaneous force from each beam is the same, which leads to a zero effective force. If the atom is moving in one direction it gets due to the Doppler shift closer to the resonance with the corresponding beam pointing against its moving direction, resulting in a stronger spontaneous force in this direction. Hence, the atom is slowed down in this direction and the cloud of atoms can be cooled down to a characteristic limiting temperature, the so-called Doppler temperature $T_D = \hbar\gamma/2k_B = 137.6\mu$K for the D_2 line of ^{6}Li [Met99]. So far we achieved a confinement in velocity space but not a confinement in real space meaning that the atoms can still leave the overlap of the beams and are lost. Hence the optical molasses acts more like a viscous medium and we need a position dependent force to achieve spatial confinement.

This position dependent force is provided by a linear magnetic-field gradient applied by the two coils (blue) which can be seen in Figure 4.2 a). The anti-Helmholtz configuration of the coils leads to a quadrupole field which causes a position dependent linear Zeeman splitting of the different m_J states as depicted in Figure 4.2 b). Since the quantization axis is defined by the magnetic field B_{MOT} which changes sign at $z = 0$ the $m_J = -1$ state always tunes to lower energies for both negative and positive z. If we shine in polarized light from both sides (σ^- because we want to drive the $|m_J = 0\rangle \rightarrow |m_J = -1\rangle$ transition), both beams are resonant with atoms sitting at the center of the trap ($z = 0$) leading to a zero effective force. If we now red-detune the beams by δ_0, the transition will be on resonance at the points characterized by the capture radius $\pm R_c$. Now, the left beam will drive the transition at $z = -R_c$ and pushes the atoms to the trap center. At $+R_c$ the beam would be again energetically resonant but due to the change of the quantization axis at $z = 0$ the atoms at $z = +R_c$ see this

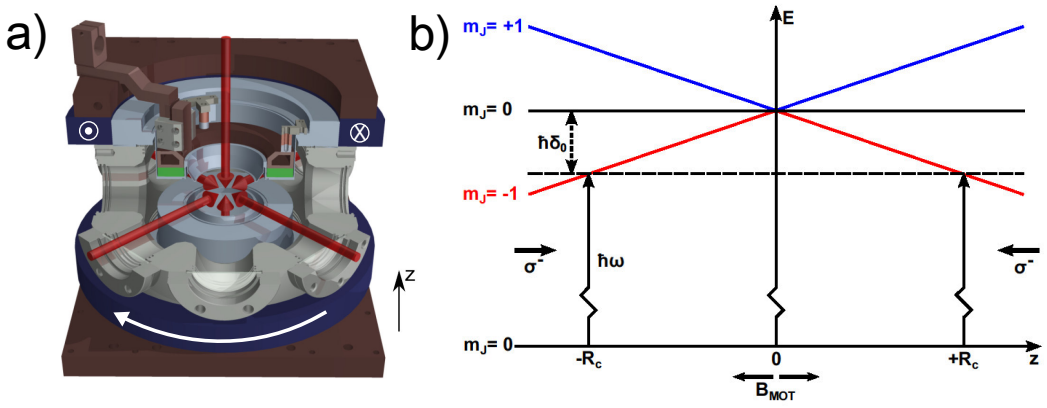

Figure 4.2.: **Setup and schematic principle of a MOT.** a) shows the experiment chamber. The red arrows describe the six slightly red detuned beams used for the optical molasses and in blue the MOT coils in anti Helmholtz configuration (white arrows) are depicted. In Figure b) the linear splitting of the magnetic sublevels m_J caused by the magnetic field gradient is shown. Since the counterpropagating σ^--polarized beams are detuned by δ_0 the transitions at $z = \pm R_c$ can be driven by the corresponding beam. This leads to an effective force directed towards the trap center. The pictures are adapted from [Wen13, Rie10]

beam with a σ^+ polarization. Thus, a beam coming from the left side cannot interact with atoms on the right side and vice versa. The resulting force of all six beams (two counterpropagating in each direction) will therefore lead to a restoring force towards the center of the trap. With this technique we are able to trap a cloud of atoms with a loading rate of about $3 \cdot 10^8$ atoms/s and cool them down to a typical final temperature of about $300\mu K$ which is quite close to the limiting temperature of $T_D = 137.6\mu K$. This is still not enough to reach quantum degeneracy and therefore we load the atoms into an optical dipole trap where we can further cool our sample by evaporative cooling.

4.3. The Optical Dipole Trap

Far-detuned optical dipole traps (ODT) are a perfect tool to trap and further cool a cloud of atoms down to quantum degeneracy because in this conservative potential the influence of spontaneously emitted photons is dramatically reduced. Moreover, this trapping mechanism does not depend on any magnetic fields which allows us to use them to control the interaction of the sample. The trapping mechanism is based on the electric dipole interaction between the strong electric field of the laser beam and the induced dipole moment of the neutral atoms. Since neutral atoms have no permanent dipole moment, this trapping mechanism is very weak and requires a pre-cooled sample which is in our experiment achieved by the MOT.

4.3.1. Theory of optical dipole trapping

To evaluate the main characteristics of optical dipole traps we follow the argumentation in [Gri00]. Here, a classical oscillator model is applied, which is a good approximation for neutral atoms with a strong dipole allowed transition. Since ^{6}Li is an alkali atom with a single valence electron, it should be well described by this model as long as we are far detuned from resonance where saturation effects can be neglected. The electric field $\mathbf{E}(\mathbf{r},t)$ of the radiation and the induced dipole moment $\mathbf{p}(\mathbf{r},t)$ which oscillates at a driving frequency ω can be written in the complex form

$$\mathbf{E}(\mathbf{r},t) = \hat{\mathbf{e}}E_0(\mathbf{r})\exp(-i\omega t) + c.c., \qquad \mathbf{p}(\mathbf{r},t) = \hat{\mathbf{e}}p_0(\mathbf{r})\exp(-i\omega t) + c.c., \tag{4.5}$$

here $\hat{\mathbf{e}}$ corresponds to the unit polarization vector. The amplitudes E_0 and p_0 are connected by

$$p_0 = \alpha(\omega)E_0, \tag{4.6}$$

via the complex dynamic polarizability α which depends in general on the driving frequency ω. Now, the interaction potential U_{dip} of the dipole moment $\mathbf{p}$ induced by the field $\mathbf{E}$ can be evaluated

$$U_{dip} = -\frac{1}{2}\langle \mathbf{pE}\rangle = -\operatorname{Re}(\alpha)|E_0(\mathbf{r})|^2 = -\frac{1}{2\epsilon_0 c}\operatorname{Re}(\alpha)I(\mathbf{r}). \tag{4.7}$$

Here, the rapid oscillating terms $\propto \exp(\pm 2i\omega t)$ vanish due to the time average labeled by $\langle\rangle$ and the spatial dependent laser intensity $I(\mathbf{r}) = 2\epsilon_0 c|E_0(\mathbf{r})|^2$ is introduced. Since the dipole moment is induced rather than permanent, a factor 1/2 has to be taken into account. The direct relation to the real part of the polarizability is responsible for the dispersive properties of the interaction, since it describes the in-phase component of the dipole oscillation. The resulting conservative dipole force is given by the gradient of the interaction potential

$$\mathbf{F}_{dip}(\mathbf{r}) = -\nabla U_{dip} = \frac{1}{2\epsilon_0 c}\operatorname{Re}(\alpha)\nabla I(\mathbf{r}). \tag{4.8}$$

It is directly proportional to the intensity gradient of the radiation field.
Besides the dipole force with its dispersive character the atom can absorb a certain power P_{abs} which can be interpreted in a quantum mechanical picture as scattering of photons with energy $\hbar\omega$ by absorption and spontaneous re-emission leading to the spontaneous force F_{spont} discussed before. The scattering rate Γ_{sc} can be written in the classical oscillator model as

$$\Gamma_{sc} = \frac{P_{abs}}{\hbar\omega} = \frac{\langle \dot{\mathbf{p}}\mathbf{E}\rangle}{\hbar\omega} = \frac{1}{\hbar\epsilon_0 c}\operatorname{Im}(\alpha)I(\mathbf{r}). \tag{4.9}$$

This reveals the absorptive character of the spontaneous force since Γ_{sc} is related to the imaginary part of the polarizability which describes the out of phase component of the

oscillation. The crucial point is, that this photon scattering process leads to heating in the atomic cloud which limits us in both temperature and lifetime since for very low traps this can cause atom loss.
An explicit expression of the polarizability α can be calculated in a Lorentz model of a classical oscillator. In this simple picture the valence electron is bound elastically to the atomic core able to oscillate with an eigenfrequency ω_0 modeling the optical transition frequency. Allowing the electron to emit radiation leads to a equation of motion of a damped, driven oscillator

$$\ddot{x} + \Gamma_\omega \dot{x} + \omega_0^2 x = -\frac{eE(t)}{m_e}, \tag{4.10}$$

where e and m_e describe the charge and mass of the electron and Γ_ω is a classical damping rate which is given by [Jac75]

$$\Gamma_\omega = \frac{e^2\omega^2}{6\pi\epsilon_0 m_e c^3}. \tag{4.11}$$

Integrating the equation of motion and using that the dipole moment can be written as $\mathbf{p} = e\mathbf{x}$ leads to the following explicit equation for the polarizability

$$\alpha(\omega) = 6\pi\epsilon_0 c^3 \frac{\frac{\Gamma}{\omega_0^2}}{\omega_0^2 - \omega^2 - i\left(\frac{\omega^3}{\omega_0^2}\right)\Gamma}, \tag{4.12}$$

where $\Gamma \equiv \Gamma_{\omega_0} = (\omega_0/\omega)^2\Gamma_\omega$ describes the on-resonance damping rate which corresponds in a semi-classical approach like the two-level-system to the spontaneous decay rate of the excited state and thus has to be related to the dipole matrix element between ground and excited state

$$\Gamma_{2level} = \frac{\omega_0^3}{3\pi\epsilon_0\hbar c^3}|\langle e|\mu|g\rangle|^2. \tag{4.13}$$

As mentioned in the beginning for atoms with a strong dipole-allowed transition Γ is still a good approximation of the spontaneous decay rate. With expression 4.12 we can write down an explicit equation for U_{dip} and Γ_{sc} using Equation 4.7 and 4.9.

$$U_{dip}(\mathbf{r}) = \frac{3\pi c^2}{2\omega_0^3}\left(\frac{\Gamma}{\Delta} + \frac{\Gamma}{\Delta + 2\omega_0}\right) I(\mathbf{r}), \tag{4.14}$$

$$\Gamma_{sc}(\mathbf{r}) = \frac{3\pi c^2}{2\hbar\omega_0^3}\left(\frac{\omega}{\omega_0}\right)^3 \left(\frac{\Gamma}{\Delta} + \frac{\Gamma}{\Delta + 2\omega_0}\right)^2 I(\mathbf{r}), \tag{4.15}$$

with the detuning labeled by $\Delta = \omega - \omega_0$ and a linear dependence on the applied intensity $I(\mathbf{r})$. Since the driving frequency ω is mostly tuned close to resonance so that

$|\Delta| \ll \omega_0$ holds, the second term in the equations can be neglected leading to the well known scaling laws $U_{dip} \propto \Gamma/\Delta$ and $\Gamma_{sc} \propto (\Gamma/\Delta)^2$ which can be summarized in

$$\Gamma_{sc} = \frac{\Gamma}{\hbar\Delta} U_{dip} \tag{4.16}$$

This approximation is the so-called rotating-wave approximation in which the resonance at $\omega = -\omega_0$ can be neglected. It becomes clear from the scaling laws that it is possible to have low heating rates and a sufficiently large trapping potential by using a far-detuned laser beam at high power. For light alkali atoms like ^{6}Li this detuning has to be even larger due to their large recoil temperature $T_{rec} = \hbar^2 k^2 / 2mk_B$ because in a 3D harmonic trap the following linear heating rate can be given [Gri00]

$$\dot{T} = \frac{1}{3} T_{rec} \bar{\Gamma}_{sc}, \tag{4.17}$$

where $\bar{\Gamma}_{sc}$ corresponds to the mean photon scattering rate.

Further, depends the sign of U_{dip} only on the sign of the detuning Δ, which leads to

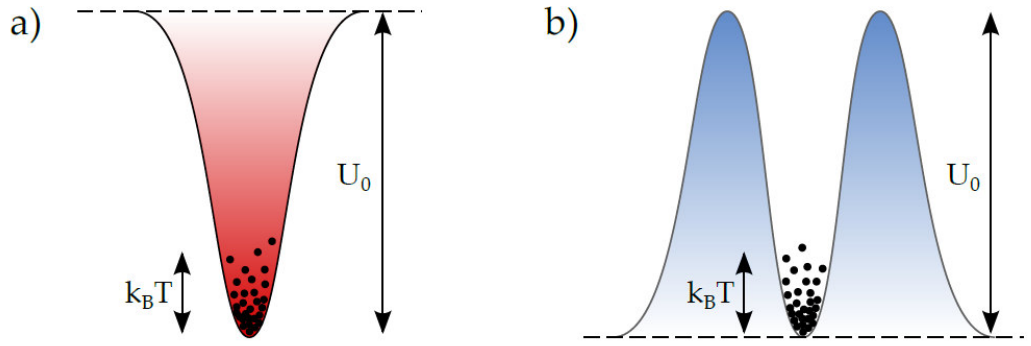

Figure 4.3.: **Schematic view of a red and blue detuned optical dipole trap (ODT).** Since the atoms (black dots) are always minimizing their energy in the potential they are attracted to the maximum of intensity for a red detuned ODT a) whereas they are repelled from the maximum of intensity for a blue detuned ODT b). The corresponding dipole trap potential is shown as the colored area with a maximum trap depth U_0. Due to the fact that the kinetic energy $k_B T$ of the trapped atoms is much smaller than the trap depth the dipole trap potential can be well approximated in the center by a harmonic oscillator. The picture is adapted from [Gri00]

two possible trap configurations seen in Figure 4.3. If $\Delta < 0$ which corresponds to a red-detuned laser beam, U_{dip} is negative and the atoms are trapped in the intensity maximum of the radiation field. Whereas for blue-detuned light, $\Delta > 0$, the dipole potential is positive and the energy is minimized in the intensity minimum. Hence, with both configurations trapping of atoms is possible. Nevertheless, trapping atoms

with a red-detuned laser beam with a Gaussian intensity distribution is much simpler than using a blue-detuned laser with a 'donut' like intensity potential. This is the reason why we use a focused Gaussian beam at $\lambda = 1064$nm which is far red-detuned from our dipole transition in ^{6}Li at ~ 671nm. Due to the large detuning we need a power of about 200W to achieve a sufficient trap depth. By shining in the laser in y-direction we obtain the following intensity profile of the beam as seen in Figure 4.4 a)

$$I(x,y,z) = \frac{2P}{\pi w_x(y) w_x(y)} \exp\left(-2\frac{x^2}{w_x^2(y)} - 2\frac{z^2}{w_z^2(y)}\right), \tag{4.18}$$

where the following characteristic parameters are used

$$w_i(y) = w_{0,i}\sqrt{1 + (y/y_R, i)^2}, \tag{4.19}$$

which describes the beam radius at $1/e^2$ of the beam intensity in $i = x, z$-direction. $w_{0,i}$ corresponds to the minimal beam waist in the beam focus and the Rayleigh length $y_{R,i} = \pi w_{0,i}^2/\lambda$ is the distance from the focus where the corresponding beam waist $w_{0,i}$ has increased by a factor of $\sqrt{2}$. As seen from the definition of the Rayleigh length, it will always be larger than the beam waist, which leads to a weaker confinement in the propagation direction. As seen in Figure 4.4 b) the confinement along the propagation axis can be improved by crossing two perpendicular polarized beams under an angle 2ϕ because the axial confinement is now limited by the length of intersection given by $l \approx 2w_z/\sin(\phi) < y_{R,i}$. We achieve this in our setup by back reflecting the dipole trap beam under a small angle of $\sim 6°$, which increases the trap depth in the focus by a factor of two.
In order to stay trapped in the optical potential the kinetic energy $k_B T$ of the atoms has to be much smaller than the trap depth U_0 which requires pre-cooling in the MOT as already mentioned. As shown in Figure 4.3 the atomic cloud only occupies a small volume deep in the trap which allows us to approximate the potential as a harmonic oscillator with well defined energy levels separated by $\hbar\omega_i$

$$U_{dip}(x,y,z) \approx -U_0\left(1 - 2\left(\frac{x}{w_{0,x}}\right)^2 - 2\left(\frac{z}{w_{0,z}}\right)^2 - \left(\frac{y}{y_R}\right)^2\right), \tag{4.20}$$

where the trap depth $U_0 \sim I_0 = 2P/(\pi w_{0,x} w_{0,z})$ and the characteristic trap frequencies can be obtained by

$$\omega_{x,z} = \sqrt{\frac{4U_0}{m w_{0,x,z}^2}} \quad \text{and} \quad \omega_y = \sqrt{\frac{2U_0}{m y_R^2}}. \tag{4.21}$$

They scale with the beam power as $\omega_i \propto \sqrt{P}$ and in the case of a crossed back-reflected beam y_R has to be replace by l and the trap depth increases by $U_0 \sim 2 \times I_0$. This approximation is only valid as long as the atoms just probe the energy levels deep in

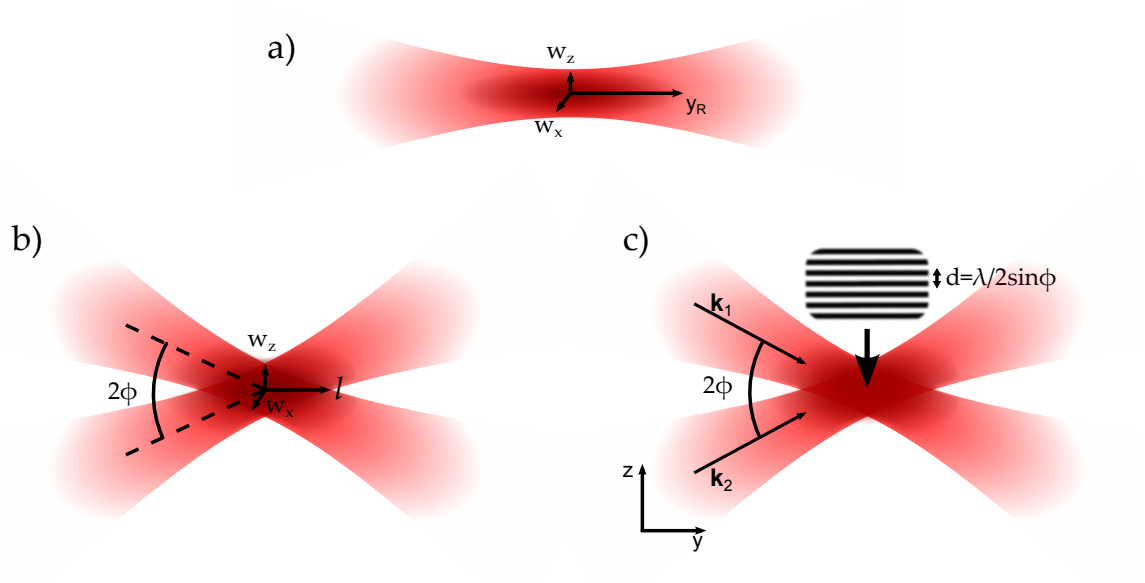

Figure 4.4.: **Different beam configurations of red detuned optical dipole traps.** In a) the ODT is formed by a single Gaussian beam and the trap volume is defined by the beam waists (here: $w_{0,x,z} = w_{x,z}$) and the Rayleigh length y_R. By crossing two Gaussian beams with perpendicular polarization the confinement in y-direction $l < y_R$ can be improved dependent on the crossing angle 2ϕ. In c) both beams with wave vectors $\mathbf{k}_1$ and $\mathbf{k}_2$ have the same polarization, which leads to an interference pattern in z-direction. The picture is adapted from [Boh12]

the dipole trap potential.
In Figure 4.4 c) both beams have identical polarizations which results in interference of the two beams. We use such a beam configuration in our pancake trap to create optical potentials with a really tight confinement in one direction as explained later in more details. The total intensity of the interfering beams is given by

$$I_{tot} \approx |\mathbf{E}_1(\mathbf{r}) + \mathbf{E}_2(\mathbf{r})|^2 \quad \text{with} \quad \mathbf{E}_i(\mathbf{r}) = E_{0,i} \exp(i\mathbf{k}_i\mathbf{r}) + c.c. \tag{4.22}$$

If both beams have the same intensity and cross each other with $\mathbf{k}_1$ and $\mathbf{k}_2$ under an angle of 2ϕ the intensity can be written as [Nei13]

$$I_{tot} \approx I_0 |\exp(ik(\cos\phi y - \sin\phi z) + \exp(ik(\cos\phi y + \sin\phi z)|^2 = 4I_0 \cos^2\left(\frac{2\pi z}{\lambda \sin\phi}\right), \tag{4.23}$$

here $k = 2\pi/\lambda$ is the wave vector and I_0 the intensity of each beam. Due to the linearity between the intensity and the trap depth, we achieve a periodic trap structure

in z-direction with a spacing between neighboring trap sites given by

$$d = \frac{\lambda}{2 \sin \phi}. \tag{4.24}$$

The interfering beams increase the trap depth U_0 by a factor 4 which leads to a factor 2 higher heating rate compared to non-interfering beams.

4.3.2. ODT setup and transfer from the MOT

In Figure 4.5 an overview over the optical setup of our experiment is presented. The red beam path corresponds to the optical dipole trap and the setup is described in detail in [Boh12]. Hence, we will focus on the main characteristics of the setup. To produce the high output power of about 200W, we use a diode pumped single-mode, linearly polarized Ytterbium fiber laser (IPG Photonics). The two crossed acousto-optical modulators (AOM) allow a fast and precise power modulation and the cylindrical telescope (cyl) leads to an elliptical beam profile. By crossing the incoming beam with the back-reflected beam under an angle $2\phi = 12°$ we create a surfboard shaped ODT with a beam ellipticity of $1 : 6$.

Since we can approximate our dipole potential quite well by a harmonic oscillator this allows us to characterize our potential by one parameter, the trap frequency $\omega_i = 2\pi\nu_i$ where $i = x, y, z$. To measure these trap frequencies we prepare a two-component non-interacting Fermi gas in the ODT at the zero-crossing of the 3d scattering length a at 527G. To minimize the interaction further one can remove the atoms in spin state $|1\rangle$ by a resonant light pulse provided by the imaging light to create an one-component Fermi gas of atoms in state $|2\rangle$. Now we suddenly increase the potential depth $U_0/2$ by twice its value to U_0. This compresses the cloud and excites a so-called breathing mode. A breathing mode describes a collective motion of the trapped atoms and hence can be monitored in a change of the width of the cloud. Therefore, we release the atoms from the trap after different wait times and image them after a certain time-of-flight (TOF) of about 2ms. Dependent on the wait time we will image a different oscillation state of the breathing mode which is amplified by the time-of-flight expansion of the cloud. We image the atoms by absorption imaging which will be discussed in Section 4.5. With this imaging method we can monitor the width of the cloud on every axis dependent on the wait time and thus monitor an oscillation like the one seen in Figure 4.6 a). By fitting this oscillation for each trap depth U_0 with a damped sine function due to the left over interaction and the inhomogeneous magnetic field gradients, we can determine the oscillation frequency which is twice the trap frequency because of the breathing mode character of the oscillation. We further fit the data in Figure 4.6 b) with a fit function $\propto \sqrt{const. \cdot U_0}$ motivated by the theoretical principles of dipole traps introduced in the section before. The fit describes the data with an error of about 10% which is sufficient for our applications and we found the following equation for the

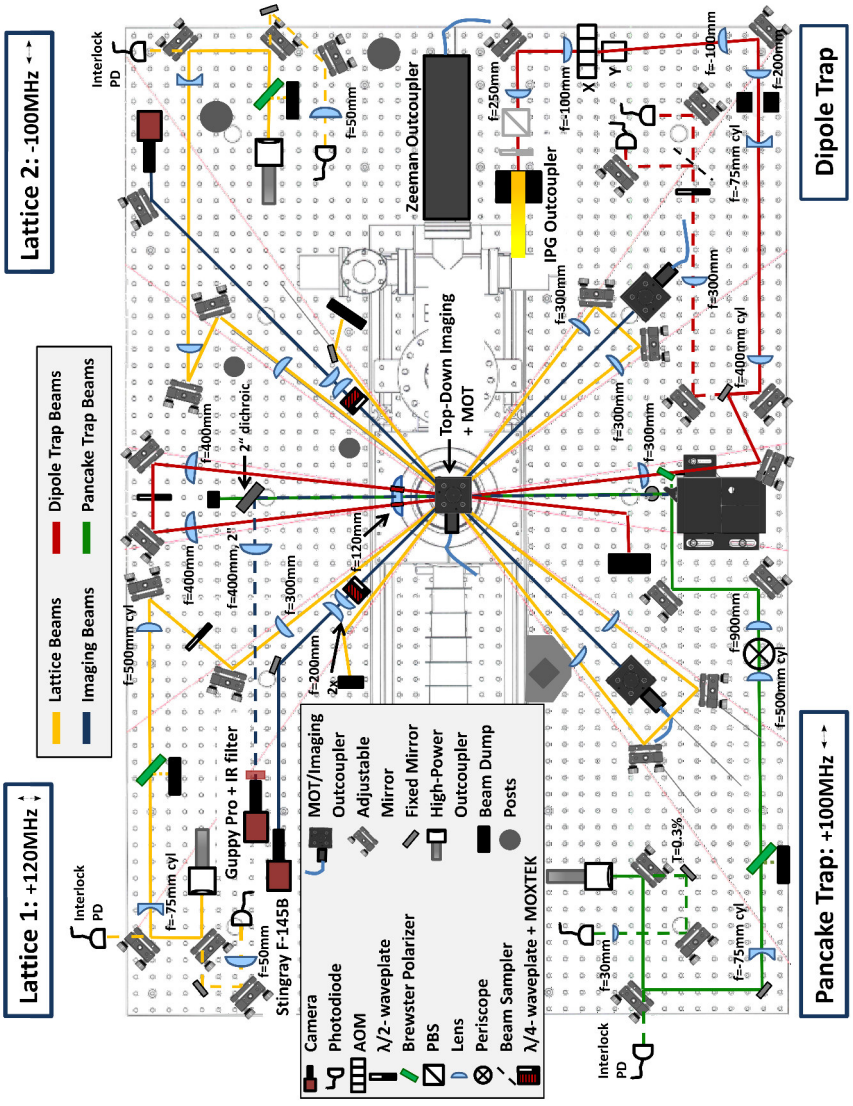

Figure 4.5.: **Optical setup around the experimental chamber.** The beam paths of the retro-reflected MOT beams are parallel to the beam paths of the imaging beams (blue). In red the ODT beam path is depicted and the green beam path provides the light for the pancake trap. Further are the lattice beams depicted in yellow. The sketch is taken from [Nei13].

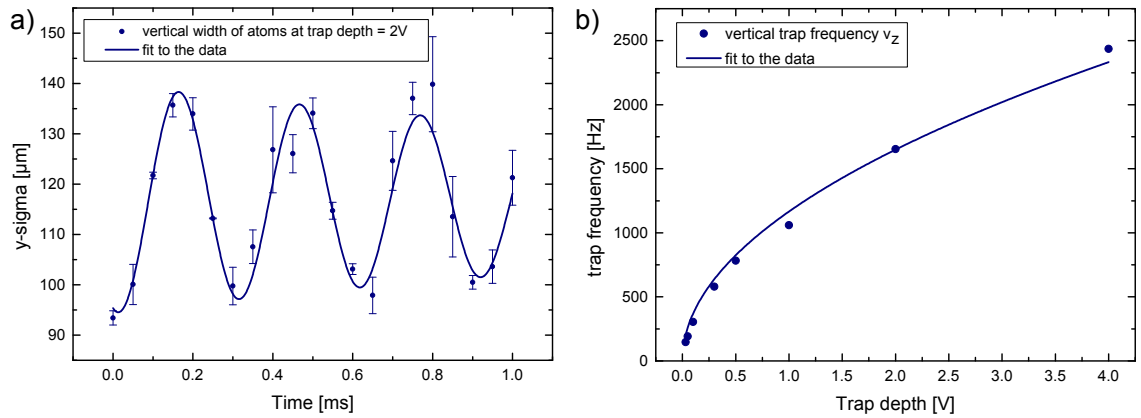

Figure 4.6.: **Vertical trap frequencies of the ODT.** In a) the excited collective motion of the atoms inside the trap is depicted at a trap depth $U_0 = 2$V and fitted by a damped sine to obtain the oscillation frequency. In b) the result for different trap depth is shown and fitted by a square root law.

vertical trap frequency

$$\nu_z = 1166 \frac{Hz}{\sqrt{V}} \sqrt{U_0}. \tag{4.25}$$

The trap frequencies in the horizontal axis have been determined in an analogous manner given as

$$\nu_x = \sqrt{\left(255 \frac{Hz}{\sqrt{V}}\right)^2 \cdot U_0 + (5Hz)^2} \quad \text{and} \quad \nu_y = \sqrt{\left(24 \frac{Hz}{\sqrt{V}}\right)^2 \cdot U_0 + (5Hz)^2}. \tag{4.26}$$

Thereby results the additional factor of $\nu_{mag} = 5$Hz from the influence of the magnetic field saddle of the Feshbach coils at 527G. This leads to a weak anti-confinement in the vertical axis and a weak confinement in the horizontal plane. Due to the fact that the optical confinement in vertical direction is much stronger than the magnetic anti-confinement, it can be neglected as done for the trap frequency in Figure 4.6 b). These trap frequencies have been obtained using an old photodiode box to measure the beam power. Hence they have to be rescaled to the power measured by the new photodiode box by $\nu_{new} = 1/\sqrt{1.15} \cdot \nu_{old}$. In Figure 4.7 the dependence of the horizontal magnetic trap frequency ν_{mag} on the magnetic offset field is depicted. The deviation between the depicted ν_{mag} and the results from the square root fits of the horizontal trap frequencies in the ODT is due to the fact that the latter measurement only includes the influence of the magnetic offset field during the breathing mode in the optical confinement whereas the release from the ODT allows a more precise measurement of ν_{mag} since the optical confinement is much less.

The description of the transfer from the MOT into the ODT can be found in [Nei13] and is here briefly summarized. By switching on the ODT to a power of 200W thermal

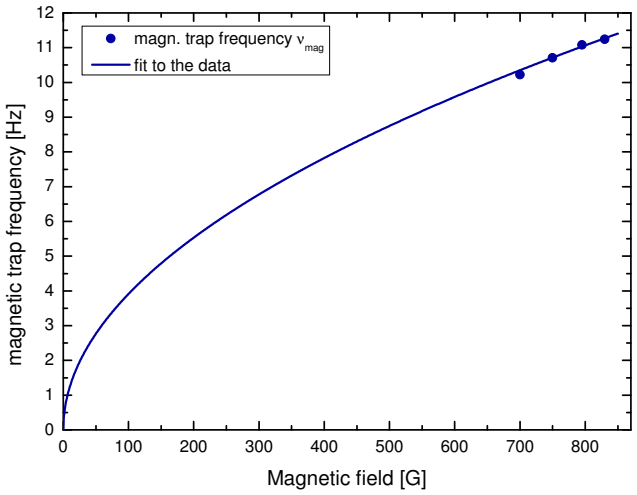

Figure 4.7.: **Horizontal magnetic trap frequencies of the Feshbach field.** The trap frequency was measured by suddenly lowering the trap depth of a single beam optical dipole trap and monitoring the breathing mode along the axis of weak optical confinement $\nu_y \ll \nu_{mag}$ as discussed in the text. The data was fitted by a square-root law and the following magnetic field dependence was obtained $\nu_{mag} = 0.39\frac{Hz}{\sqrt{G}} \cdot \sqrt{B}$.

lensing occurs, which results in a shift of the beams dependent on the power. Nevertheless, since the focus of the thermalized ODT is precisely aligned to the saddle point of the magnetic offset field provided by the Feshbach coils, its position is fixed. This position can be adjusted quite well by releasing the atoms from the ODT, so that they expand along the magnetic offset field trajectories. To obtain a highly efficient transfer of the atoms we have to overlay the MOT with the focus of the ODT as good as possible. But the zero crossing of the MOT gradient and even the zero crossing of the Feshbach gradient are not aligned with the ODT focus. Since the zero crossing of the Feshbach gradient is located closer to the ODT focus position we load the atoms first into a MOT which is composed of the Feshbach quadrupole field, the so called 'Feshbach MOT'. The Feshbach MOT can be moved during the transfer vertically by decreasing the current of the lower coil via a parallel circuit. For movement along the horizontal axis we use the last coil of the Zemann slower and an additional coil mounted on the front viewport to move along the axis defined by the entering dipole trap beams. By optimizing this movement we can efficiently transfer the atoms from the MOT into our ODT. To improve the overlap of the Feshbach MOT and the ODT focus further we change the detuning of the MOT laser beams which leads to a slight compression of the trapped cloud. After finalized transfer we lower the ODT power to 40W to achieve a stable trap position. This allows us to trap a cloud of around 10^6 atoms in the ODT

which now can be further cooled evaporatively.

4.3.3. Evaporative cooling

To reach quantum degeneracy we perform evaporative cooling in the ODT which is perfectly suited for that due to the low heating rate. The energy of the pre-cooled atomic cloud can be described by a Maxwell-Boltzmann velocity distribution and the temperature of the gas can be obtained from its mean velocity. By removing the hottest atoms from the cloud and giving the remaining atoms time to re-thermalize by elastic collisions, the mean velocity decreases to an equilibrium value defined by the trap depth U_0. Because of the decrease in temperature the phase space density increases, thus repeating this progress allows to cool the gas of atoms down to the quantum degenerated regime.
We perform evaporative cooling by decreasing the laser power of our ODT over $(2-3)$s and thus lowering the trap depth. In doing so, we monitor the laser power with the help of two photodiodes (each calibrated to a certain power regime) collecting a fraction of beam power transmitted through a mirror. During the evaporation process we switch from the high power photodiode with low gain to a low power photodiode which has a unity gain factor and exhibits a improved dynamic range. After further evaporation we switch in the photodiode box of the low power photodiode to a special operational amplifier with a gain factor of 300. This increases the dynamic range of the input channel of the experimental control and enables us to efficiently cool further. The power is stabilized by controlling the diffraction efficiency of two AOMs by regulation of the rf-power via a PID-feedback loop. The AOMs are rotated by 90° with respect to each other. To achieve efficient thermalization and due to the collision properties of ultracold fermions, we apply a radio-frequency-pulse of about 600 ms at the beginning of the evaporation procedure to achieve a $50:50$ mixture between the states $|1\rangle$ and $|2\rangle$. Further, for fast thermalization we perform the evaporation at magnetic fields with large positive scattering length a. To form a mBEC one uses typically magnetic fields of $B_{mBEC} \approx 796$ G because at this fields the produced Feshbach molecules are still stable. For a production of a Fermi gas of atoms in the spin state $|1\rangle$ and $|2\rangle$ the evaporation takes place at lower magnetic fields $B_{FG} \approx 300$ G where a is negative [Nei13].

4.4. Setup of the two dimensional Pancake-Trap

Because we want to investigate the physics of an ultracold degenerate gas in two dimensions we need a large level spacing in one dimension of our harmonic dipole potential. In the remaining two dimensions the trap frequency has to be rather small in order to allocate a large number of energy levels which can be populated and thus confine as much atoms as possible in these dimensions. Hence, we have to create a dipole potential with a large aspect ratio between the vertical and horizontal axis.

We use a beam configuration as shown in Figure 4.4 c) and optimize the aspect ratio by maximizing the angle of intersection to $\phi \sim 7°$ which is limited by the aperture of the viewports. Due to the interference of the two beams, this leads to a stack of flat dipole potentials with a vertical spacing between each so-called pancakes of about $d = 4.4\mu$m. This spacing is enough to successfully suppress tunneling between adjacent pancakes in the trap depth regime we operate. In order to make the pancakes as round as possible we have to use again elliptical shaped beams with an aspect ratio of $1 : 8$. A trap depth of $U_0 \approx 6.8\mu$K is obtained at a power of 2W in each of the two pancake beams. By transferring our evaporatively cooled quantum gas from the surfboard shaped ODT into one single pancake potential we enter a system in which we can fulfill the 2d-ness condition given in the beginning of Section 3. Further details on the design criteria of the pancake trap can be found in [Boh12].

Stability validation

In order to load reproducibly into one single pancake, the trap has to be designed in a way that long time drifts are much smaller than half the spacing d between the pancakes. Thus, to ensure a high passive stability of the interference fringes all required optical elements are mounted into a heavy aluminum casing to damp any mechanical oscillations. The elliptical shaped beam with $\lambda = 1064$nm enters the casting under an angle of 45° as seen in Figure 4.8 and passes a $50 : 50$ non-polarizing beam splitter. A $\lambda/2$-plate can be inserted in the lens mount in the upper beam path to rotate

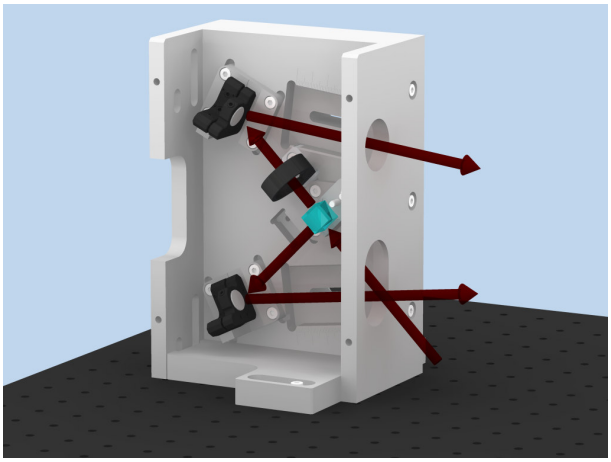

Figure 4.8.: **Aluminum casing for the pancake trap setup.** The incoming beam is divided by a $50 : 50$ non-polarizing beam splitter and reflected into the experiment chamber. Since both beams have the same polarization they interfere in the crossing point and create a stack of flat optical potentials in vertical direction called pancakes. The picture is taken from [Wen13]

the polarization to switch off the interference. The pancake trap then reduces to a normal crossed dipole trap which simplifies the alignment. The two dielectric mirrors

reflect both beams into the experiment chamber where they cross under an angle of $2 \cdot \phi = 14°$. Both beams are focused by a $f = 900$mm lens before the casing as seen in Figure 4.5. The stability of the pancake position was determined by a tomographic radio-frequency spectroscopy method which will be discussed in detail in Section 5.3. From this measurements [Nei13] we could validate the good short term stability of the interference pattern forming the pancakes since the phase change was $\Delta\phi \leq \pi/12$, which is enough that we can reproducible load a particular pancake. The long term stability was investigated as well by repeating the tomography measurement about a week later. By comparing the data, a long term stability of $\Delta\phi \leq \pi/8$ was detected. This means that in a completely thermalized experiment the position of the pancakes changes by less than 500nm over ten days. Since this is less than an eighth of our pancake spacing the position is stable on the time scales of our experiment.

Optical setup

In order to create samples that are as cold as possible, we have to minimize any source of heating in the system which could be caused for example by intensity fluctuations of the trapping laser beams. Hence, we need a low-noise laser system for the trapping beams. We will discuss here the most important parts and changes of the setup and briefly summarize the results of the noise characterization. Detailed information concerning the optical setup and the characterization of the noise of the laser system can be found in [Nei13].
The light for the pancake trap is provided by a $\sim$ 40W NUFERN fiber amplifier (Sub$-1174-22$) which amplifies the seed light of a continuous-wave single-frequency solid state laser (INNOLIGHT Mephisto-S 500 NE) emitting at $\lambda = 1064$nm. The maximum output power is 500mW but for sufficient seeding we just need about 70mW. The noise of the Mephisto is actively reduced by a so-called 'noise eater' leading to a measured relative intensity noise (RIN) below -135dB/Hz. Further, it has a very narrow linewidth of less than 1kHz. Nevertheless, because of the amplification of the Nufern the RIN is significantly increased as well, but will not limit the intended experiments as described in [Nei13]. At high stabilized laser power of about 25W the RIN first increases from about -115 dB/Hz to -105 dB/Hz and then decreases to the Mephisto RIN for frequencies larger than 200kHz.
In Figure 4.9 the optical setup is shown. The light enters through the Nufern fiber under a particular angle which is compensated by the proximate collimator and the beam diameter is increased to about 4.4mm (Gaussian diameter) to reduce the effect of thermal lensing. The following optical isolator (Thorlabs IO$-10-1064$ VHP) prevents back reflection into the fiber and with the low-order $\lambda/2$-waveplate the losses in the isolator can be minimized leading to a transmission of about 92%. Clipping is avoided since the aperture diameter is about 9mm. The polarization is rotated to the horizontal axis by an additional low-order $\lambda/2$-waveplate behind the optical isolator. The following combinations of low-order $\lambda/2$-waveplates and polarized beam splitter (PBS) are used to clean the polarization and adjust the power in the corresponding arms. As seen in

Figure 4.9 the light of the NUFERN is furthermore used for two lattice beams which are implemented in the experimental setup as well (yellow beam path in Figure 4.5). In principle, the setup of each arm is quite similar so we will focus on the design of

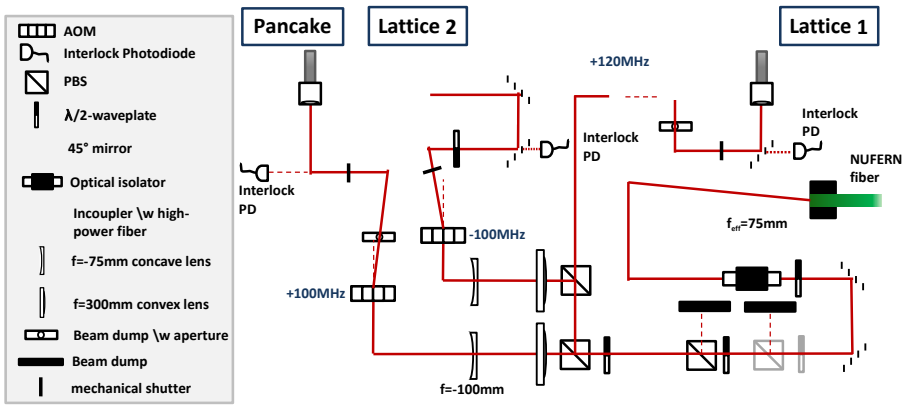

Figure 4.9.: **Nufern breadboard.** This figure shows the optical setup providing the light for both the pancake trap and two lattice beams which are implemented in the setup as well. The sketch is adapted from [Nei13].

the pancake trap arm and point out the differences. In order to match the size of the AOM crystal and the fiber facet of the high-power fibers (OZ Optics) which connects the Nufern breadboard with the experiment chamber setup we reduced the beam size by a factor of 3 in the pancake trap beam. This is achieved by a telescope with anti-reflection (AR) coated spherical lenses with $f = 300$mm and $f = -75$mm in the lattice beams and $f = 300$mm and $f = -100$mm in the pancake trap beam. As can be seen from the different telescope configurations, the beam size of the lattice beams is reduced by a factor of 4. This is due to the fact that we have not yet checked, if the incoupling of these beams in the fiber facet is sufficient. If it is not, we probably have to modify these telescopes as well and optimize the divergence angle like in the procedure described below. The $f = 300$mm lens can be tilted in both axes to compensate the astigmatism which occurs due to thermal lensing at high power. The telescope in the pancake trap beam was modified because the coupling efficiency was below 60%. We took a closer look at the beam profile and the divergence angle of the beam and used an additional fiber to send light provided by the Mephisto from the side of the experiment chamber to the Nufern setup to measure the facet of the high power fiber. In doing so we matched the beam profile and the divergence angle of the ingoing and outgoing beam which leads to the modification of the telescope. In Figure 4.10 the beam profile of the corresponding beams at different steps is depicted. With this modification we again achieved a coupling efficiency of $\sim 85\%$ which is necessary because we will couple later up to 8W into the fiber.
The diffraction efficiency of the AOM can be controlled precisely by adjusting the rf-frequency power and since we use the first diffraction order it allows us to switch and

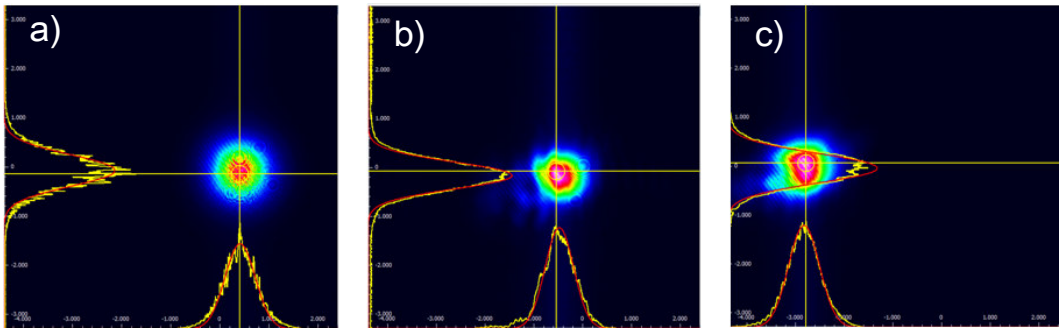

Figure 4.10.: **Beamprofile during optimization of pancake trap arm.** In a) the beam profile of the outgoing beam (from Mephisto) in front of the high-power fiber incoupler is shown with a Gaussian diameter of $\sim 1258\mu$m. b) corresponds to the Nufern beam measured at the same position with a $f = -75$mm lens in the telescope and a Gaussian diameter of $\sim 1132\mu$m. c) shows the same beam with a $f = -100$mm lens and optimized collimation leading to a Gaussian diameter of $\sim 1238\mu$m

fine-tune the beam power in each arm. The zeroth order is thereby dumped on a beam dump. Further, we insert a mechanical shutter in each beam path which can be externally controlled by the ADWIN experimental control. This allows to block the beam without shutting down the AOM. Thus, the AOM stays in its thermal equilibrium state the whole time which improves the stability of the beam. To stabilize the intensity we measure a fraction of the light with a photodiode on the experimental chamber side of the high-power fiber (see Figure 4.5) and regulate the diffraction efficiency with a digital PID-feedback loop via the experimental control.
Since the three beams cross each other in the experiment chamber, one has to avoid frequency beating in a critical range up to 100kHz which would result in heating of the atoms and therefore losses. To prevent this the frequency of each beam arm is slightly shifted by the AOMs as depicted in Figure 4.9. Furthermore, the polarization of the lattice 1 beam is rotated by 90°.
The photodiodes in Figure 4.5 and Figure 4.9 labeled as interlock PD belong to our interlock system which automatically shuts down the beam power by switching off the diffraction of the AOMs if the coupling efficiency drops below 60%. That is necessary because the high-power fiber facets can be damaged if too much power is dumped in them. The power is measured before and after the fibers by the photodiodes and the efficiency is calculated by an Arduino micro-controller board connected to the AOM driver box.
A detailed description of the pancake trap beams (green beam path in Figure 4.5) on the side of the experiment chamber can be found in [Nei13].

Trap frequencies of the Pancake-trap

As already described in Section 4.3 our dipole potential can be well approximated by a harmonic oscillator characterized by the trap frequency $\omega_i = 2\pi\nu_i$ where $i = x, y, z$. To measure these trap frequencies we transfer a mBEC from the ODT to the pancake potential to populate as less pancake potentials as possible. Since we want to avoid any effect of interaction in the breathing mode, we ramp up the magnetic field to about 1400G where we prepare a two-component Fermi gas. By removing the atoms in spin state $|1\rangle$ via a resonant light pulse provided by the imaging light we create a non-interacting one-component Fermi gas of atoms in state $|2\rangle$. Now we ramp back to 795G and excite and monitor the breathing mode as described in Section 4.3.2. By fitting the damped oscillation we determine the oscillation frequency which is twice the trap frequency because of the breathing mode character of the oscillation. In Figure 4.11 the resulting trap frequencies for each direction as a function of trap depth U_0 are depicted. The vertical trap frequency ν_z ∼kHz is much larger than the horizontal trap frequencies ν_x and ν_y which verifies the large aspect ratio of the pancakes. The fits

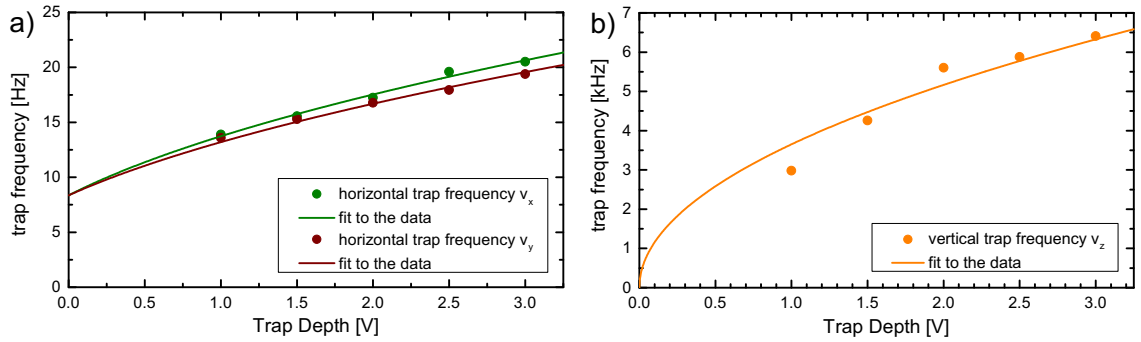

Figure 4.11.: **Trap frequencies ν_i for different trap depth U_0 in the pancakes.** Each frequency was determined by monitoring the oscillation of a breathing mode excited by a sudden compression of a non-interacting Fermi gas.

are obtained by a square-root law of the form $\nu_i = \sqrt{const.^2 \cdot P_{Laser} + \nu_{mag}^2(B)}$. ν_{mag} results from the influence of the magnetic field saddle of the Feshbach coils mentioned in Section 4.3.2. Due to the fact that the optical confinement in vertical direction is much stronger than the magnetic anti-confinement, it can be neglected as done for the ODT trap frequency in Figure 4.6 b) and for the vertical trap frequency in Figure 4.11 b). In the horizontal plane a magnetic trap frequency of $\nu_{mag} = 8.36$Hz was measured at a field of 795G and its dependence on the magnetic offset field has been shown in Figure 4.7. From the square root fit we obtained the following relation between the trap frequencies and the trap depth $U_0 \propto P_{Laser}$

$$\nu_x = \sqrt{119\frac{Hz^2}{V} \cdot U_0 + (8.36Hz)^2} \quad \text{and} \quad \nu_y = \sqrt{104\frac{Hz^2}{V} \cdot U_0 + (8.36Hz)^2}$$

$$\nu_z = 3777 \frac{Hz}{\sqrt{V}} \sqrt{U_0}.$$

Furthermore a calculation of the aspect ratio shows that our pancakes are almost round since $\nu_x/\nu_y \approx 1.1$ (at a trap depth of 2.5). Including the vertical frequency we obtain $\nu_x : \nu_y : \nu_z \approx 1.1 : 1 : 327$ which is in very good agreement with the planed aspect ratio of 1 : 1 : 300 calculated from the projected waists $w_{horizontal} = 600\mu$m and $w_{vertical} = 2\mu$m.

4.5. Imaging of an atomic cloud

In the end of each experiment cycle we image our cloud of atoms either in-situ, thus trapped in an optical dipole potential, or after releasing them for a certain time-of-flight. Since the atoms cannot emit any photons in these states, we apply an absorption imaging technique to measure the density distribution of our prepared degenerate quantum gas. From the density distribution one can extract all the relevant physical quantities like number of atoms, temperature or the quantum statistic of the gas.

4.5.1. Absorption Imaging

The basic principle of this imaging technique is to shine in a resonant laser beam and monitor the transmitted light on a CCD camera. Due to the fact that the atoms will scatter the light they will appear as a dark, shadow-like spot in the image I_{abs}. To obtain the optical density ρ_{OD} we take a second image displaying only the imaging light without the atoms I_{ref} and a dark image without both I_{bg}. Due to the imaging process we already integrate the optical density in the imaging direction (here: z-direction) which leads to

$$\rho_{OD}(x,y) = -\ln T(x,y) = -\ln\left(\frac{I_{abs}(x,y) - I_{bg}(x,y)}{I_{ref}(x,y) - I_{bg}(x,y)}\right), \tag{4.27}$$

here $T(x,y)$ corresponds to the relative transmission. By subtracting the I_{bg} from each image the images are cleaned from the dark signal of the camera, whereas the division of the cleaned images eliminates any static inhomogeneities in the imaging beam like interference fringes. In the low intensity limit $I \ll I_{sat}$ the scattering cross-section between the imaging photons and the atoms becomes independent of the intensity and is given in the case of circular-polarized imaging light propagating along the magnetic field axis by $\sigma_0 = 3\lambda^2/2\pi$. For a different polarization or propagation direction σ_0 has to be modified by a numerical factor from the corresponding Clebsch-Gordon coefficient. Based on that, the transmitted intensity follows from the Lambert-Beer law with the three dimensional cloud density $n(x,y,z)$

$$I(x,y) = I_0(x,y) \int \exp(-\sigma_0 n(x,y,z)) dz. \tag{4.28}$$

With the definition $T(x,y) = I(x,y)/I_0(x,y)$ and using Equation 4.27 we can connect the two dimensional cloud density with the optical density

$$n(x,y) = \int n(x,y,z)dz = \frac{\rho_{OD}(x,y)}{\sigma_0}, \tag{4.29}$$

which is directly related to the atom number per pixel via

$$N_{pix}(x,y) = \frac{A_{pix}}{M^2\sigma_0}\rho_{OD}(x,y). \tag{4.30}$$

The known camera properties M^2 and A_{pix} correspond to the magnification and the area of one pixel. In the high intensity case $I \gg I_{sat}$ the scattering cross section becomes intensity dependent and the relation for the number of atoms has to be modified

$$N_{pix}(x,y,) = -\frac{A}{\sigma_0 M^2}\frac{I_0}{I}(1 - T(x,y)). \tag{4.31}$$

By fitting the density distribution of the atoms obtained from the absorption image, we can deduce quantities like the atom number or temperature. Nevertheless, this measurement destroys our ultracold gas in each cycle due to absorption of imaging photons which heat up the cloud. A more detailed discussion about imaging techniques and extracting physical quantities from the density distribution can be found in [Ket99, Ott10].

4.5.2. Up-down imaging

We can image our atoms from three directions as seen in Figure 4.5 which has been described in detail in [Nei13]. Hence, we will focus here only on the changes in the imaging setup. A new camera (AVT Stingray F145 B) was implemented in the up-down imaging which has a smaller read out noise, a better quantum efficiency and a pixel size of $6.45\mu\text{m} \times 6.45\mu\text{m}$. The imaging beam is coupled out from the old up-down imaging beam path by a 2" mirror and focused on the camera by a Melles Griot Doublet LAI15/083 lens with $f = 190\text{mm}$ which leads to an effective magnification of $M = 1.98$. We use here doublet lenses because they achieve a very low wavefront distortion of the imaging beam. The resolution of the imaging system can be estimated by the numerical aperture $NA \approx 0.14$ of the $f = 80\text{mm}$ Doublet lens collecting the light from the experimental chamber. This leads to a resolution of $d_{min} = 0.61 \cdot \lambda/NA = 2.9\mu\text{m}$. To further improve the resolution of the up-down imaging a new objective with a numerical aperture $NA \approx 0.6$ will be implemented in the setup in the near future as mentioned earlier (see [Kri13]).

4.5.3. Laser diode modulation to improve the atom number determination

Determining the atom number from absorption imaging relies on two main factors. First the light of the imaging pulse has to be resonant with the atomic transition which demands a precise control of the frequency. This is achieved by actively stabilizing a tunable external diode laser (Toptica DL 100) by Doppler-free saturation spectroscopy. Both the cooling and imaging lasers are beat-locked to a spectroscopy laser and a linewidth of the locked lasers less than 1MHz was obtained. Since we use for cooling and imaging the D_2-transition in ^{6}Li with a natural linewidth of $\Gamma = 5.87$MHz, the obtained linewidth is sufficient. The duration of the imaging pulse τ was optimized to about 8μs to minimize the shot noise level.

Due to the large photon recoil $v_{rec} = \hbar k_{photon}/m_{^6Li} = 0.085$m/s, even at this short

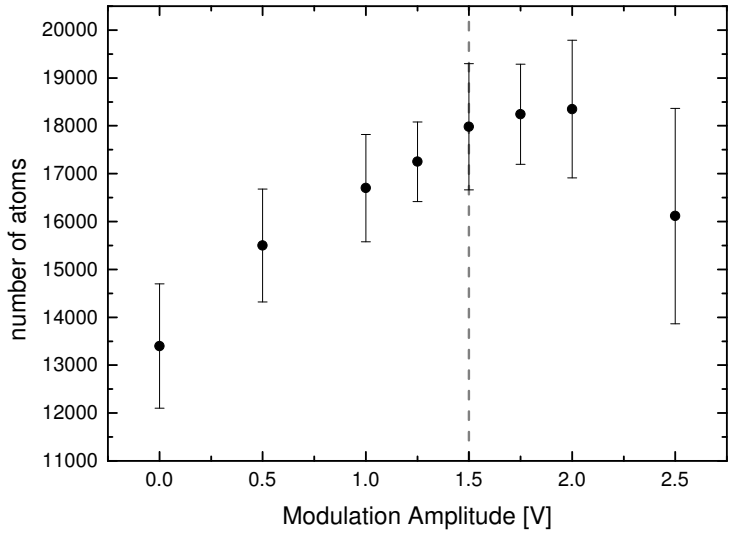

Figure 4.12.: **Voltage amplitude of the diode current modulation.** One can see a clear optimum around a modulation amplitude $V_{pp}/2 = 1.5$. Due to the compensation of the Doppler shift we could increase the number of imaged atoms by a factor of 1.3

pulse duration the atoms are moved and get Doppler shifted with respect to the imaging light. Thus, we see less atoms because of a reduced absorption probability and further the shape of the density distribution might be changed due to increase of the dispersion in the atomic could. We estimated this effect by imaging the cloud with a pulse duration of $\tau \approx 1\mu$s and measuring the absorption distribution by slightly detune our imaging laser and recording the change in atom number. By repeating this measurement with a pulse duration of $\tau = 8\mu$s we determined a drift of the maximum of the distribution

of about 2.5MHz which is on the order of $\Gamma/2 = 2.9$MHz. Since the effect of dispersion is maximized at a detuning of $\Gamma/2$ with respect to the resonance frequency, we decided to compensate this detuning due to the Doppler shift. By modulating the current of the imaging laser diode with a 8μs long linear ramp provided by a 20MHz arbitrary waveform generator (Agilent 33220A) the frequency of the imaging light can be directly shifted. Thus, we calibrated the applied voltage to achieve a 5 MHz shift corresponding to a voltage offset of 1V by comparing the frequency shift between the imaging laser and the spectroscopy laser. Now we scanned the current modulation amplitude $V_{pp}/2$ and monitored the imaged atom number of a mBEC at 730G trapped in the dipole trap at a pulse duration of $\tau = 8\mu$s. The result is seen in Figure 4.12 and a clear maximum is visible around $V_{pp}/2 = 1.5$V leading to a gain in the detected atom number of about 1.3.
As pointed out in the section before, the determination of the atom number depends on the intensity of the imaging light. From [Geh03] we know, that the saturation intensity for the D_2-transition in ^{6}Li is given by $I_{sat} = 25.4\text{W/m}^2$. To estimate our imaging intensity we extracted the counts of one pixel with maximum signal from our raw data. Since the quantum efficiency of the camera (AVT Stingray F145B) is $\eta = 0.45$ and the gain factor is $g = 0.29$ the ratio I/I_{sat} can be estimated by

$$\frac{I}{I_{sat}} = \frac{counts_{pix}}{\eta g}\frac{hc}{\lambda\tau}\frac{1}{A_{pix}/M^2}, \tag{4.32}$$

which leads with $counts_{max,pix} = 330$ to $I/I_{sat} \approx 1/3$. Thus, the intensity of our imaging light is on the same order as I_{sat} and we are not in one of the limiting regimes. This leads to an error in the atom number determination. A more detailed description and evaluation of the relative error can be found in [Ott10]. By lowering the imaging intensity with an -11dB attenuator to $I/I_{sat} \approx 1/30$ we measured an increase in atom number in the dipole trap by a relative factor of 1.7 on average. Nevertheless, we went back to the old intensity to get a better signal to noise ratio and hence underestimate our atom number by a factor of 1.7. In the following measurements we will therefore correct the atom number by these factors.

5. Preparation of a degenerate quasi-2d gas

After the discussion of the characterization of our experimental setup in the previous chapter, we now want to focus on the preparation of a quasi two dimensional system. Therefore, we start in the first two sections by describing the transfer of our degenerate sample from the ODT into the pancake trap. In the next Section 5.3 we describe our radio frequency (rf) tomography method to verify that we are able to load into a single pancake potential. Here we will focus on several applications which improved this method. In the last two sections of this chapter we will validate, that we are able to prepare and control a quasi two dimensional system of ultracold atoms.

5.1. Transfer from ODT into several layers of the Pancake traps

By evaporative cooling of our atomic cloud in the ODT we are able to enter the quantum degenerate regime. Dependent on the interaction in the system controlled by the scattering length we end up either with a BEC consisting of $|12\rangle$-molecules or a degenerate Fermi gas with atoms in a ballanced $|1\rangle - |2\rangle$ spin mixture. To control the number of particles which will be transferred, we can either apply an additional magnetic field gradient to decrease the depth of the effective trapping potential in one direction or carefully lower the depth of the optical potential further. In the first method which we call 'spilling' the particles are spilled from the trap due to the magnetic force acting on them. The second method continues evaporative cooling by decreasing the intensity of the optical dipole trap beams which might become inefficient at some point when the density becomes to low and no re-thermalization can be achieved at sufficient timescales. We lower our optical trap depth down to $U_0 \approx 30$nK so that the magnetic trapping potential of the Feshbach coils has to be taken into account even in the vertical direction. Hence, we still trap the particles in horizontal direction by the very harmonic magnetic field, whereas the atoms can leave the trap in vertical direction, because of the anti-confining saddle point of the Feshbach field, controlled by the weak optical confinement. With both methods a degenerate gas of about 10^4 particles can be produced but the latter method leads to a cooler sample in the pancake trap. To transfer the particles we perform an adiabatic compression of the cloud which squeezes the particles in all directions by increasing the intensity of the ODT beams. At the

same time, we slowly ramp up the power in the pancake trap beams. To achieve a well thermalized sample in the pancakes we allow elastic collisions and wait additional $(100 - 200)$ms before decreasing the power in the ODT beams. Figure 5.1 depicts a mBEC at a magnetic field of 795G before (upper row) and after the transfer (lower row). In the vertical imaging direction the difference between the surfboard shaped ODT and the almost round pancake potential can be seen. In the images taken along the hor-

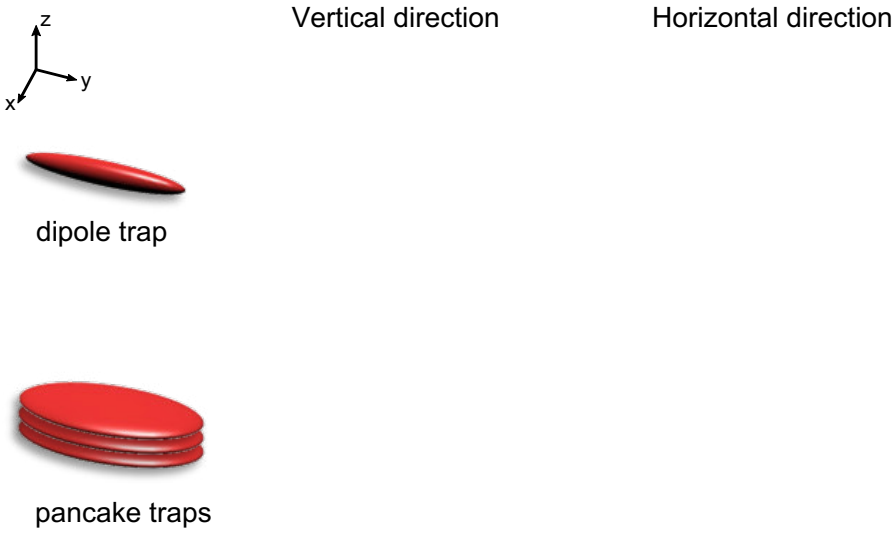

Figure 5.1.: **A mBEC before and after transferred into a stack of pancake traps.** In the first row a cloud of condensed molecules is imaged from two directions in the ODT. The second row shows a similar sample transferred into a stack of $\sim$ 5 pancake trap potentials. Since the cameras in the two imaging directions have a different magnification and imaging angle the width in x-direction is slightly different. The picture is adapted from [Nei13].

izontal axis the anisotropy of the tighter axis x and z of the ODT is depicted which emphasizes the surfboard character of our optical dipole trap. The vertical extension (z-axis) was estimated from a Gaussian fit to be around 20μm which is significantly larger than the expected vertical width of a single pancake potential which is around 4μm. Hence, if we were transferring directly using these trap configurations we would transfer particles in about 5 neighboring pancake potentials. The depth of focus can be calculated by $z_{DOF} = 4\lambda/NA^2 \approx 93\mu$m with the nominal aperture of $NA \approx 0.15$ given by the size of the vacuum window for this imaging direction. By comparing this value with the extension of the almost round pancakes along this directions of about $(200 - 300)\mu$m one sees, that the achievable resolution of $d = 2.7\mu$m will be decreased because of blurring and that a single pancake can not be optically resolved. Since

$z_{DOF} \propto 1/NA^2$ one could increase the depth of focus to reduce the effect of blurring by decreasing the NA to $0.10 - 0.12$. This would result in a slightly worse effective resolution $d = 0.61\lambda/NA$ of $(3.41 - 4.1)\mu$m which is on the edge to resolve the particles in the individual pancake potentials. Nevertheless, we succeeded in loading into the pancake trap potential and the lifetime of the transferred sample was measured to be about $50s$ which is considerably larger than the time the gas is kept in the pancake potentials $\sim$ 2s [Nei13].

5.2. Loading a sample in a single Pancake trap

In order to prepare a quantum degenerate gas in just a single pancake trap potential we tried to decrease the vertical expansion of the cloud in the ODT before the transfer. Therefore, we realigned the foci of the ODT so that they are exactly at the position where the beams intersect which leads to an increased confinement in vertical direction. Since few Hertz pressure fluctuations in the airflow might lead to vibrations of the optical elements, we decreased the fan speed of the flow box controlling the temperature of the air at the optical table to reduce shot-to-shot fluctuations of the ODT beam position.
To lower the vertical spreading further we implemented a technique which we call 'painting'. Thereby, we modulate the rf-frequency of the x-AOM (see Figure 4.5) of the optical dipole trap with a sine function. This results in a fast modulation of the optical dipole trap position in the horizontal plane and since the frequency of $\sim$ 50MHz is larger than the trap frequency of the ODT in x-direction (axis of intermediate confinement) the atoms cannot follow the modulation and hence see an effective time independent dipole potential. Due to the modulation, the effective waist in x-direction is increased and we achieve a larger aspect ratio leading to a change of the density of states in x-direction. Hence, the population of the cloud will be preferentially spread in the x-direction which leads to a decrease of the occupation in the other directions especially in vertical direction. That results in a squeezing of the cloud in vertical direction and a broadening in x-direction.
As can be seen in Figure 5.2, it is easier to transfer a molecular BEC into a single pancake potential instead of a degenerate Fermi gas. Due to the fermionic quantum statistics, the degenerate Fermi gas obeys the Pauli principle which leads to a pressure that keeps fermions separated. The pressure in the degenerate Fermi gas is always non-zero even at zero temperature which brings about a larger spatial expansion than a non- or weakly interacting Bose gas where all particles are condensed in the single particle ground state. Hence, the mBEC with its smaller vertical extension can be transferred into a single pancake potential much more easily.
Furthermore, as we want to perform measurements in the BEC-BCS crossover we have to transfer a mBEC into a single pancake potential. Investigating the crossover regime with a degenerate Fermi gas is almost impossible since we normally create our degenerate Fermi gas on the left hand side of the Feshbach resonance around 500G as

seen in Figure 2.6. The larger negative scattering length compared to the right hand side of the resonance leads to a more efficient evaporative cooling. If we now ramp the magnetic field over the zero-crossing of the scattering length to reach the crossover regime, we immediately create deeply bound molecules by three-body recombination processes. Since the scattering length a is still small in this regime three-body collision processes with the background gas are not yet suppressed as close to the Feshbach resonance. Hence, as the molecules can be transferred into deep vibrational energy states, they release a lot of binding energy which leads to a high loss of particles. In case of a mBEC which is already formed close to the Feshbach resonance, the three-body-collision processes are significantly suppressed as seen in Equation 2.46 leading to less losses by investigating the crossover regime.
To shift the position of the atoms trapped in the ODT in vertical direction we apply a magnetic field gradient and thus a force $\sim \mu \nabla B$ slightly pulling or pushing the atoms with magnetic moment μ. To determine the position of the atoms we perform a radio-frequency spectroscopy as described in the following section. Thus by adjusting the strength of the gradient we can precisely tune the position of the cloud with respect to the pancake potentials and load it into a single pancake. This enables us further to control the partition of transferred particles in one or two pancake potentials as can be seen in [Wen13].

5.3. Measuring the density distribution in the pancake trap

In order to investigate how the transferred particles are distributed within our pancake trap potentials, a measurement technique was developed to probe the spatial distribution of the atoms in each pancake trap using tomographic radio-frequency (rf) spectroscopy. The principle is shown in Figure 5.2 for both a degenerate Fermi gas (DFG) and a molecular BEC (mBEC) depending on the homogeneous magnetic offset field of the Feshbach coils. The addressing of each pancake is achieved by applying a magnetic-field gradient $\frac{\partial B}{\partial z}$ provided by the MOT coils in the vertical direction due to the spin projection along the magnetic offset field in z-direction. Due to this magnetic field gradient, the energy shift between the non-degenerate hyperfine states (see Figure 2.5) becomes position dependent in z-direction. Since the hyperfine states are split by $\sim$ 80 MHz, and tune with the magnetic offset field, the transition can be driven by rf-pulses. As long as the position dependent resonance frequencies of the atoms in each pancake trap are separated by more than the effective resolution of the rf-pulse the pancakes can be addressed individually.
We prepare our system in spin state $|2\rangle$ and transfer the atoms into spin state $|3\rangle$ at a certain rf-frequency. By imaging the atoms in state $|3\rangle$ we are able to determine the atom number for each rf-frequency, corresponding to the atoms at a certain spatial position in z-direction. Thus, we repeat this measurement while scanning the

rf-frequency and monitor the atom number. This measurement technique has already

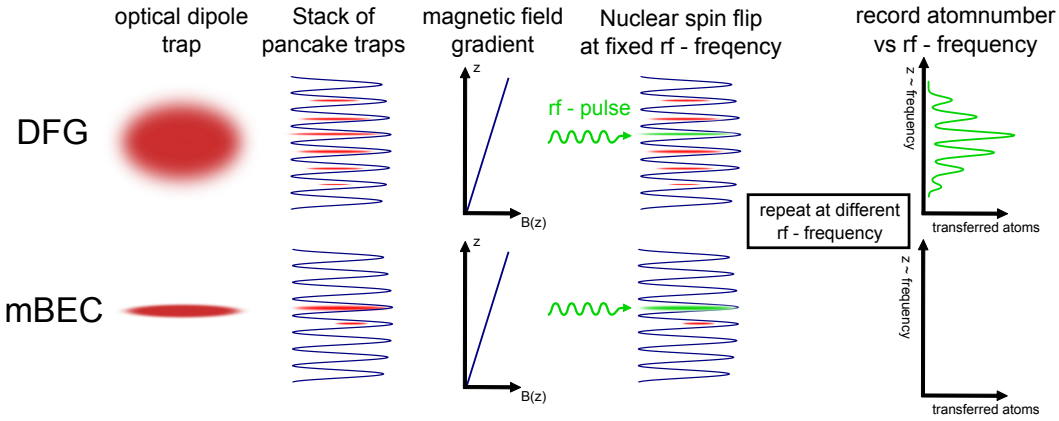

Figure 5.2.: **Principle of rf-tomography for both a degenerate Fermi gas (DFG) and a molecular BEC.** The basic steps of the measurement technique mentioned in the text are shown. The amount of loaded pancake potentials depends on the quantum statistics of the prepared quantum system. Due to the Pauli pressure the DFG is more expanded and thus loading into a single pancake is easier by transferring a mBEC. The picture is adapted from [Wen13].

been described in detail in [Nei13] and we will summarize the important steps, starting with a short introduction to rf-spectroscopy.

5.3.1. Basic principles of radio-frequency spectroscopy

As described in Section 2.3.4, the three lowest hyperfine states of ^{6}Li in the Paschen-Back regime differ in their orientation of the nuclear spin. Hence, driving a transition between two of these states requires flipping the nuclear spin, which can be achieved via a magnetic dipole transition by applying an oscillatory magnetic field. Since this transition is a forbidden electric dipole transition its lifetime is far longer than the timescale of our experiment.

$$\mathbf{B}(t) = \mathbf{B}_0 \cos(\omega_{RF} t) \tag{5.1}$$

This field couples to the magnetic moment of the atoms and the transition rate Γ_{if} for this effective two-level system can be obtained from Fermi's golden rule [Chi05]

$$\Gamma_{if} = \frac{2\pi}{\hbar} |\langle f|\hat{V}_{RF}|i\rangle|^2, \tag{5.2}$$

where $\hat{V}_{RF} = \hbar\hat{\Omega}/2$ corresponds to the interaction operator which strength is given by the Rabi frequency Ω. The initial and final states can be written as a product wave

function of the external and internal state where the internal state is described by the hyperfine or spin wave function $|\chi\rangle$ and the external state is described by the spatial wave function $|\varphi\rangle$. Since typical energies of rf-transitions are in the MHz range the momentum transfer to the atoms is negligible and the spatial wave function is not effected. This leads to

$$\Omega_{if} \propto \langle f|\hat{V}_{RF}|i\rangle = \langle \chi_f|\hat{V}_{RF}|\chi_i\rangle\langle\varphi_f|\varphi_i\rangle. \tag{5.3}$$

Thus the strength of the transition from $|2\rangle$ to $|3\rangle$ depends not only on the coupling of the rf-field to the spin but also on the overlap of the spatial wave functions.
We create the oscillatory magnetic field by an impedance matched rf-antenna which is mounted inside the experimental chamber. If the oscillation frequency is on resonance with the rf-transition frequency, we induce Rabi oscillations between the states $|2\rangle$ and $|3\rangle$ with full contrast. The probability of finding the atom in state $|3\rangle$ after applying a resonant rf-pulse of length t is given by [Bra03]

$$P_{|3\rangle} = |b(t)|^2 = \sin^2\left(\frac{\Omega t}{2}\right). \tag{5.4}$$

Here we see, that in an ideal, coherently driven system we can completely transfer the atom to state $|3\rangle$ after a pulse duration of $t = 2\pi/\Omega$ which corresponds to a π-pulse. As mentioned above the Rabi frequency is related to the amplitude of the oscillating field and can thus set by the applied rf-power $P_{RF} \propto B_0^2$.

5.3.2. RF-Tomography

Since we have successfully prepared an ultracold degenerate Fermi gas of atoms in a spin mixture of $|1\rangle$, $|2\rangle$ or a molecular BEC $|12\rangle$ as seen in Figure 5.2, we remove atoms in state $|1\rangle$ by a resonant light pulse of about 10μs provided by our imaging light. Otherwise, this spin component would lead to interaction effects while performing the rf-tomography, which would cause three-body-losses and a shift of the resonance frequency [Zür13]. Since in the case of a transferred molecular BEC the atoms are bound into diatomic molecules, we ramp the magnetic offset field to a magnetic field region of about 1000G where the atoms are no longer bound into confinement induced dimers due to collisional dissociation and apply the light pulse. From our measurements we see that this procedure in fact heats the remaining atoms, but that they do not leave the pancake potentials [Wen13]. Our system now consists of a single-component Fermi gas and we sweep back to typical fields of either 527G or 795G.
In a next step we apply the magnetic field gradient in z-direction provided by the MOT coils. Since the minimum of the MOT potential and the minimum of the pancake potential are not superimposed, the resonance frequency gets shifted due to the offset field of the MOT coils.
We apply gradients up to 72G/cm provided by a Delta Elektronika power supply (SM

$45 - 70$D) where the creating current is stabilized using a PID feedback loop with parameters especially optimized to control a constant current. For that matter the current in the MOT coils is measured by a LEM current transducer (LEM LAH 50-P/SP3). Due to the feedback loop we are able to compensate the effect of temperature on the resistance of the coils. A overheating interlock is obtained by an Arduino microcontroller checking the resistance of the coils during the measurement.
The gradient can be estimated from the measured current to compensate gravity since $\mu\frac{\partial B}{\partial z} = m_{^6Li}g$ with a levitation current of 0.069V and an offset value of 0.0156V. Thus, the gradient at 6V corresponding to 60A is given by $72\text{G/cm} = 7.2\text{mG}/\mu\text{m}$. The splitting of the $|2\rangle - |3\rangle$ transition depends on the magnetic offset field and can be calculated to be 6.3Hz/mG at 795G [Bre31]. This leads to a spacing of the individual pancakes in frequency space of about $6.3\text{Hz/mG} \cdot 7.2\text{mG}/\mu\text{m} \cdot 4.4\mu\text{m} \sim 200$Hz which is on the order of the resolution of the rf-spectroscopy method.
Nevertheless, the large gradient leads to a force acting on the atoms which has to be compensated by a large depth of the optical pancake potentials. Due to the limited available optical power, this sets a limit on the gradient strength and thus the available spacing of the rf-resonance frequencies. Besides that, the large magnetic field gradient leads to a dephasing of the atoms during the rf-pulse. Since the atoms in a coherent superposition of spin state $|2\rangle$ and $|3\rangle$ acquire a different phase they become distinguishable and thus can collide. These collisions lead to a decoherence of the rf-dressed state during the rf-pulse which results in the fact, that we are not able to apply the rf-pulse coherently. Thus, the maximum number of atoms we can transfer to state $|3\rangle$ is limited to 50% of the initial number of atoms in state $|2\rangle$. Within a 20ms pulse, which corresponds to a Fourier limited width of 50Hz we are able to transfer 50% of the atoms, which leads to a lower bound of the Rabi frequency of $\Omega \geq 25$Hz.
To find the resonance frequencies of the atoms in the individual pancake potentials, we start with a Rabi-frequency of several 100Hz and thus driving atoms from several pancake potentials. By scanning the rf-frequency over an interval of several kHz and imaging atoms in-situ along the horizontal MOT axis in state $|3\rangle$ the distribution of atoms in the pancakes convoluted with the power broadened rf-pulse is determined. Hence, the structure of the sample in the individual pancake traps cannot be resolved yet, but the resonant rf-frequency in the 80MHz range is now known up to an uncertainty of several 100KHz. Decreasing the scanned frequency interval to $\sim (800 - 1000)$Hz and minimizing the power-broadening with simultaneously transferring efficiently allows to resolve separated peaks in the distribution which can be related to the density distributions in the individual pancakes. Thereby, the determined distribution of atoms in state $|3\rangle$ in each image is fitted by a Gaussian distribution and the z-position and atom number is inferred. From the precise determination of the center position by the Gaussian fit we achieve an additional improvement of the effective resolution as seen in Figure 5.3.

The effective resolution of this measurement technique depends decisively on the stability of the magnetic offset field, since a drift of 1mG results in a rf-frequency change of 6Hz. Thus, we will now focus on the achieved improvements of the stability of the

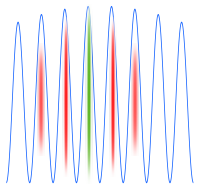

Figure 5.3.: **Gaussian fit to the imaged atom distribution in state $|3\rangle$.** Here an average of ~ 50 single shots of the obtained density profile integrated over the horizontal axis is shown and fitted by a Gaussian function to obtain the position in vertical direction. As can be seen on the inlay which depicts the raw data as monitored on the CCD camera, the pancakes are not optically resolved. The picture is adapted from [Nei13].

magnetic field and further present measurement results for both a degenerate Fermi gas and a mBEC.

5.3.3. Realizing a high magnetic field stability

So far we have described the procedure which enables us to measure the density distribution in the pancake potentials. To validate a transfer into a single pancake potential we had to optimize the resolution and the stability of the rf-tomography. To successfully address the atoms in the individual pancakes long-term fluctuations of both the magnetic offset field and the gradient have to be minimized. Since the current of the gradient coils is stabilized to 10^{-3} precision and the field of the gradient only contribute with ≈ 0.5G to the offset field, its stability of < 0.5mG is sufficient.
The long-term stability of the total magnetic offset field was measured to be only within 40mG at 800G. This corresponds to an rf-frequency stability of $6.3\text{Hz/mG} \cdot 40\text{mG} = 252\text{Hz}$ for the $|2\rangle - |3\rangle$ transition at 795G and thus had to be improved. The experiment is controlled via digital and analog channels of an ADwin Pro II real-time control system. Using analog-digital converters (ADC) and digital-analog converters (DAC) an analog input signal can be processed in a digital PID-feedback loop and sent to the analog output channels. The sampling rate of the converters is about 100kHz which results in a 10μs updated analog channel, whereas the bandwidth of the digital channels is on the order of 1MHz leading to 1μs.
The resolution of the DAC output signal was increased by a factor of 6 in the following steps: We increased the dynamic range of the voltage control input of the Feshbach

power supply (Delta Elektronika SM 30 − 200) by a factor of 2 by using the full range of the input from 0V to 10V. Besides that, the output signal of our DAC which regulates the Feshbach current is divided by a factor 3 via a TTL controlled voltage divider. The PID feedback loop then automatically increases the ADC input signal by the same factor. In summary after applying these configurations, changing one bit of the 16bit DAC with a dynamic range from −10V to 10V corresponds to a change in magnetic field of 30mG[1]. This precision seems at the first glance to be insufficient to control the offset field up to a precision of 1mG. Yet, the update rate of the DAC of about 10μs is much faster than the response of the large inductance coils whose time constant is about $\tau \approx 1$ms. Thus, by changing the DAC between two neighboring bits with its update rate, one can achieve an even larger precision. This effect is similar to pulse width modulation, where a fast change of two discrete voltages is low pass filtered for creating voltage values in between.
Further we improved the resolution of the ADC input signal as can be seen in Figure 5.4. The current in the Feshbach coils is measured using a current transducer (Dan-

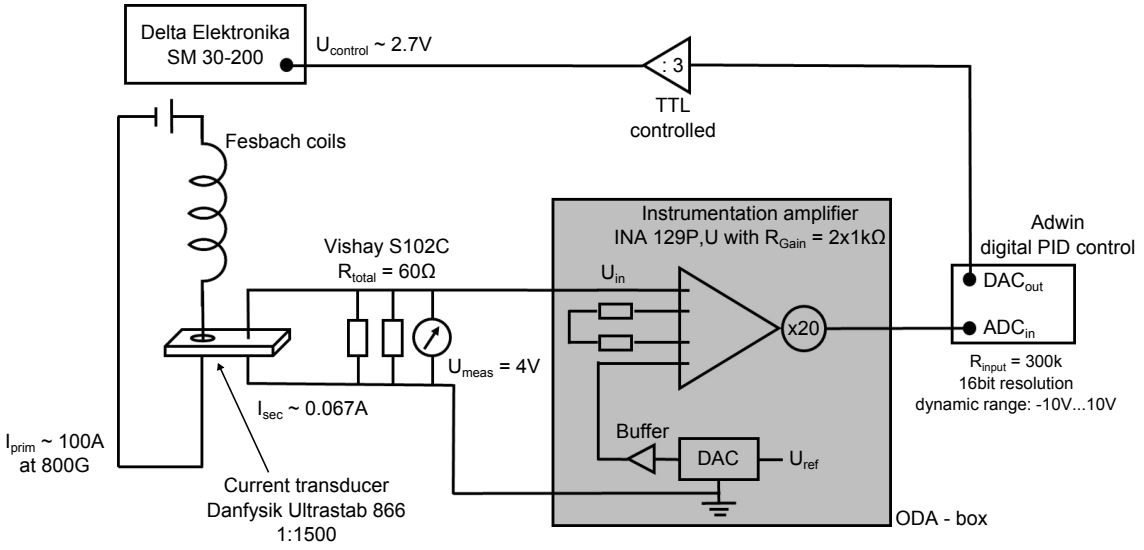

Figure 5.4.: **Schematic implementation of the new ODA-Box.** On the left side the current of the Feshbach coils is determined by a current transducer and translated into a voltage U_{in}. Further signal processing is applied in the ODA-box to obtain a higher signal resolution as described in the text. On the right side the signal is passed to the experimental control via a analog-digital converter input channel.

fysik Ultrastab 886) which generates a secondary current proportional to the primary

[1]Resolution of DAC is given by $20\text{V}/2^{16} = 0.3\text{mV/bit}$ divided by 3 and since we measured that 2.64V correspond to 795G leads to $\frac{0.1\text{mV}\cdot 795\text{G}}{2.64\text{V}} = 30\text{mG}$.

current running through the coils but reduced by a factor of 1500. This secondary current is then measured using two precision resistors of $R_{total} = 60\Omega$. At 800G where we typically perform experiments the primary current of about 100A is thus converted to a measurement voltage[2] of 4V. Directly converting this signal with the 16bit ADC of our experimental control system ranging from -10V to $+10$V would result in a resolution of 60mG/bit. In a setup where we emulated a measurement voltage (9V monobloc battery) which we recorded both with the ADC and a precise 6.5 Digit Digital Multimeter (Agilent), we could determine a peak to peak drift of the measured ratio corresponding to 40mG. As this resolution would translate to a frequency drift of 250Hz in a tomography measurement we would not be able to resolve the atoms in neighboring pancake traps separated by about 200Hz in their resonant frequency.
As we want to achieve a magnetic field stabilization of about 5mG, we have to increase the resolution by a factor 10. Therefore we subtract from the input control voltage U_{in} by means of an instrumentation amplifier (INA 129P,U) a voltage offset U_{ref}, which we can set according to the magnetic field. The RMS noise of the offset voltage U_{ref} which is generated by a precision voltage reference and set by a DAC, was measured to be $\sim 1.2 \cdot 10^{-6}$ within 13h. The difference signal is then amplified by a factor 20 and send to the ADC resulting in a factor of 20 increased resolution. The signal converting is implemented in a so-called 'offset and differential amplifier' box (ODA-box) produced by the electronic workshop of the institute and only used when we perform a tomography measurement. The noise of the high precision circuit of the box was measured which results in a long term RMS noise of $1.9 \cdot 10^{-6}$ within half a day. To assure that the noise of the input voltage is not the dominant noise source, we compared it with the noise of the current transducer. Since temperature drifts and drifts due to aging of the device are negligible[3], we focused on the short term current RMS noise which is around 2.4μA for currents in the range from DC to 10kHz. Due to the large inductance of the coils[4] an RMS current noise of 2.4μA below 100Hz translates into an RMS frequency noise[5] in the rf-transition of about 180Hz at an offset field of 795G which could be a significant contribution of limiting the resolution of our tomography measurement.
The ODA-box was implemented in the experimental setup and tested. We monitored the magnetic field stability at an offset field of 800G by measuring the measurement voltage U_{meas} with the 6.5 Digit Digital Multimeter for 2 days as seen in Figure 5.5 a). The data were binned in a histogram and fitted by a Gaussian distribution. The determined mean voltage is 3.639919V with a standard deviation of $\sigma \approx 15\mu$V. This leads to a long term RMS resolution of the magnetic field of $800\text{G} \cdot 15\mu\text{V}/3.639919\text{V} = 3.3\text{mG}$. At the same time we performed an rf-spectroscopy using the $|2\rangle - |3\rangle$ transition. Here we segmented the rf-data which was taken over 2 days into 6 data sets of 8 hours each and determined the resonance frequency for each data set by a Lorentzian fit. In Figure

[2] We use two Vishay 120Ω high precision resistors (S102C) rated up to 0.9W in parallel which minimizes the heat input to each resistor to 0.13W at a primary current of 100A.
[3] $< 2 \cdot 10^{-6}$ per °C and $< 1 \cdot 10^{-6}$ per month
[4] Coil time constant $\tau \approx 1$ms corresponding to 1kHz.
[5] $6.3\text{Hz/mG} \cdot \frac{800\text{G} \cdot 2.4\mu\text{A}}{67\text{mmA}} = 180\text{Hz}$

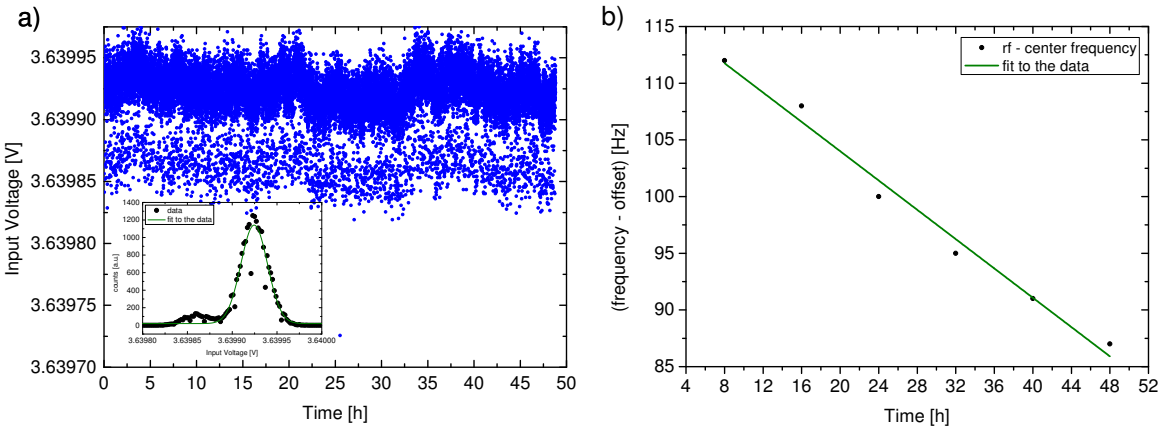

Figure 5.5.: **Test of the magnetic field stability with new ODA-box.** In a) the input voltage is monitored at $800G$ with a precise 6.5 Digit Digital Multimeter over 2 days. The inset shows the measured data binned in a histogram and fitted by a Gaussian function. From the fitted width the RMS resolution was obtained see text. The second strongly suppressed peak could be a measurement artifact. In b) the change of the $|2\rangle - |3\rangle$ transition frequency vs time is depicted. From the linear drift we could calculate the long-term magnetic field stability of 0.8mG/8h.

5.5 b) these frequencies are shown and linear fitted. From the slope of the linear drift, we determined a magnetic field stability of 5mG over 2days. Within the duration of a typical rf-tomography measurement of 8h, we thus achieved a stability of about 0.8mG, which is sufficiently low to resolve the atoms in the individual pancake potentials.
During the stabilization measurement we further investigated, that the magnetic field shifts with temperature of the Feshbach coils $\sim$ 2mG/K = 10Hz/K at 795G. This means that the cooling water of the coils need to be stabilized to $\pm$0.5K over 8h. Moreover, a shift after switching on the experiment was determined of about 100Hz – 200Hz corresponding to 15mG – 30mG, but so far we could not find any correlation to the measured current. The thermalization of the high precision resistors which have a thermal drift of 2ppm/K could significantly contribute to this, because we apply a power of $\sim$ 0.13W to each of the resistors for about 6s. This could be validated by characterizing the heating of each when the experiment is switched on. Other reasons might be some external parameter like expansion of the coils while heating up.
However, in total we achieve a long-term stability of the magnetic offset field of 1mG after the experimental setup has reached a thermal steady state about one hour after switching it on.

5.3.4. Measurement results

In order to check if all the achieved improvements lead to a better resolution of the density distribution in the pancake trap potentials and to verify, that we are able to transfer particles in only one single pancake we performed the introduced rf-tomography measurement. Figure 5.6 shows the resulting density distributions convoluted with the width of the rf-pulse and the magnetic field uncertainty. In Figure 5.6 a) we transferred a degenerate Fermi gas (DFG) into the pancake trap whereas we achieved to load a molecular BEC (mBEC) into a single pancake potential in Figure 5.6 b). We obtained the atom number at each rf-frequency by fitting a Gaussian distribution to the density distribution of the particles transferred to the state $|3\rangle$ in each integrated raw data image. Then we average over the whole stack of ~ 50 images.

In both cases the distribution was fitted with a sum of three Gaussian distributions

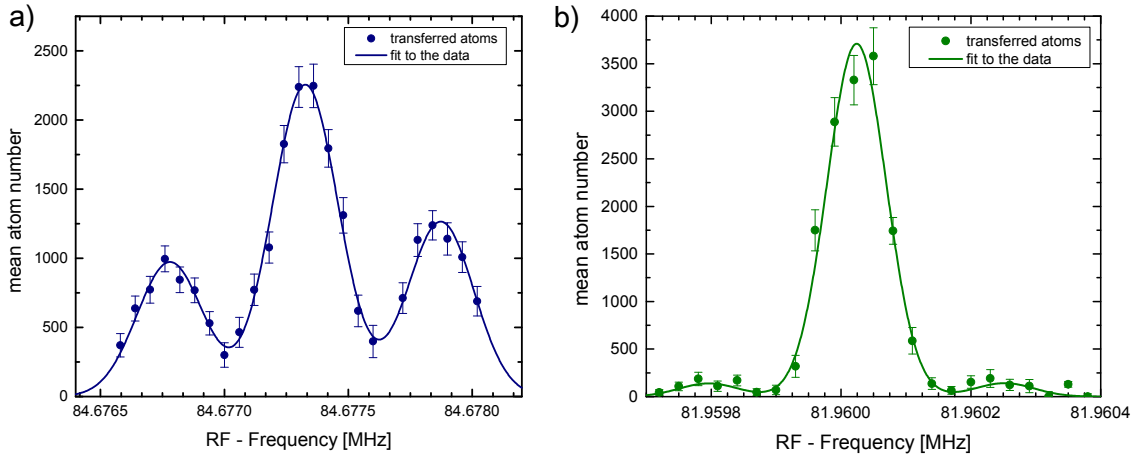

Figure 5.6.: **Density distribution of a transferred degenerate Fermi gas and a molecular BEC.** The fit values and errors are obtained by fixing a zero-background and the center frequency. In a) we see, that we transfer the degenerate Fermi gas into three pancake potentials due to the Pauli pressure. b) depicts the successful transfer of a molecular BEC into a single pancake potential.

separated by the spacing of the pancakes $\Delta\nu$

$$N_{|3\rangle}(\nu) = bg + A_{1,3} \cdot \exp\left(-\frac{(\nu - (\nu_{center} \pm \Delta\nu))^2}{2\sigma^2}\right) + A_2 \cdot \exp\left(-\frac{(\nu - \nu_{center})^2}{2\sigma^2}\right). \quad (5.5)$$

Further we can estimate the start parameter of the width of each peak σ by the width of the rf-pulse used in the measurement and an overall background bg is allowed. Due to the fact, that the integral of each Gaussian distribution is related to the atom number, we can obtain the ratio between adjacent pancakes directly from the ratio of the amplitudes A_1, A_2 and A_3. In Table 5.1 the obtained fit results are summarized.

From Figure 5.6 a) it becomes clear, that we load the degenerate Fermi gas into three

parameter	degenerate Fermi gas	molecular BEC
$A1$	974 ± 35	168 ± 40
$A2$	2260 ± 57	3716 ± 213
$A3$	1267 ± 42	176 ± 50
σ	134 ± 3 Hz	46 ± 2 Hz
ν_{center}	84.67733 MHz	81.96002 MHz
$\Delta\nu$	546 ± 5 Hz	230 ± 10 Hz
bg	0	0

Table 5.1.: **Results obtained by fitting a sum of three Gaussian distributions to the data.** The difference in the fixed center frequencies results from the fact that we performed the two measurements either at 527G or 795G. Besides that, we set the background bg to zero in both fits.

pancakes which is due to the larger expansion of the cloud because of the Pauli pressure. We load $\sim 50\%$ of the transferred atoms into the center pancake whereas the remaining atoms are almost symmetrically distributed about the two adjacent pancake potentials. The left pancake contains about 43% of the center pancake and the right one about 56%. The envelope Gaussian distribution which is more pronounced in Figure 5.6 a) is due to the distribution of the cloud in the trapping potential of the ODT. In case of the molecular BEC in Figure 5.6 b) we managed to transfer most of the atoms $\sim 95\%$ into a single pancake potential. The depicted relative atom number of transferred atoms is underestimated in the rf-tomography because the strong gradient which we apply during the measurement procedure spills atom from the pancake traps. The fraction of atoms spilled from each potential is larger for the center pancake since it contains more atoms. Thus, without the application of the gradient we should be able to load even more atoms into each pancake potential and especially into the center pancake. We determined a total loss of atoms of about 25% at a magnetic field of 795G by imaging atoms in spin state $|2\rangle$ before and after applying the gradient. In the end of this chapter we will show a different method to obtain the atom number in a single pancake which agrees more with the predictions from Section 3.2.4.
The frequency spacing of the pancake potentials of the Fermi gas could be determined from the fit to be about $\Delta\nu_{DFG} = (546 \pm 5)$Hz which is about 14% off if we compare it with the expected value. Since we perform the rf-tomography in case of a Fermi gas at 527G this leads due to the Breit-Rabi formula [Bre31] to a different splitting of the $|2\rangle - |3\rangle$ transition of ~ 15Hz/mG and hence to a spacing of $7.2\text{mG}/\mu\text{m} \cdot 15\text{Hz/mG} \cdot 4.4\mu\text{m} = 475$Hz in frequency. The determined spacing in frequency for the mBEC is $\Delta\nu_{mBEC} = (230 \pm 10)$Hz which disagrees as well with the calculated value of 200Hz at 795G by 13%.
This deviation might be due to some systematic error of the expected value. Since the splitting of the rf-transition is precisely calculated from the Breit-Rabi formula,

we will focus on the error of the gradient or the pancake spacing. The gradient was estimated by the compensation of gravity which might be off by a factor of 5% due to a drift in the offset value of the levitation current. The spacing was calculated from the angle between the intersecting beams which should be quite stable due to the aluminum casing but might be off by 10% since it was never precisely measured. If we assume those as the dominant errors in the system the overall deviation of 13% can be explained.
All in all, we could verify by the rf-tomography that we are able to load a molecular BEC into one single pancake potential.

5.4. Cooling in a single pancake

Both the temperature and the number of atoms define if we prepare a quasi two dimensional quantum system. We thus optimized the transfer procedure for being as cold as possible after the transfer into a single pancake trap. Moreover, we implemented a technique to precisely control the final number of particles in the trap. In Section 5.1 we already introduced the spilling technique and the procedure of evaporative cooling. These methods allow us to adjust the number of particles in the ODT which are then transferred to the pancake trap. As we will see in this section by further optimizing these techniques we could lower the temperature in the pancake trap.
Figure 5.7 sums up the progress and shows the individual contributions of the different steps. To observe the change in temperature during the several steps we measured the expansion of the trapped cloud in-situ in both directions by imaging a mBEC in a single pancake from above. From an increase of the width of the cloud obtained by a fit of a Gaussian distribution we infer, that we have a higher temperature in the sample and vice versa. In doing so, we compare the Gaussian width at equal trap depth thus at the same atom number. The atom number was controlled either by the depth of the optical dipole trap labeled as 'gradient off' (gravity is still compensated) or by the spilling technique 'gradient up' in vertical direction by overcompensating gravity. As seen from the connected lines the temperature of the atoms in the pancake trap depends slightly on the number of transferred particles. For a magnetic field of 690G and with spilling the atoms, a change of about 0.3μm per 1000 atoms could be determined (black solid line, triangles). We will focus in the following discussion on a transferred number of particles around $30000 - 39000$ per spin state[6]. Further, we performed the measurement for two magnetic offset fields 690G (black) and 730G (green). The difference between the lines of about $(2 - 3)\mu$m is mostly because of the decreased density due to the larger molecules.

To give a rough estimate for the achieved temperature we can use the equipartition theorem to approximate the contribution to the mean energy by $\frac{1}{2}m_{dimer}\omega_x^2\sigma_x^2 \approx \frac{1}{2}k_BT$, where ω_x describes the trap frequency in the pancake trap which is about $2\pi \cdot 19.2$Hz.

[6]Atom number is corrected by factors 1.3 and 1.7 due to the absorption imaging see Section 4.5.3

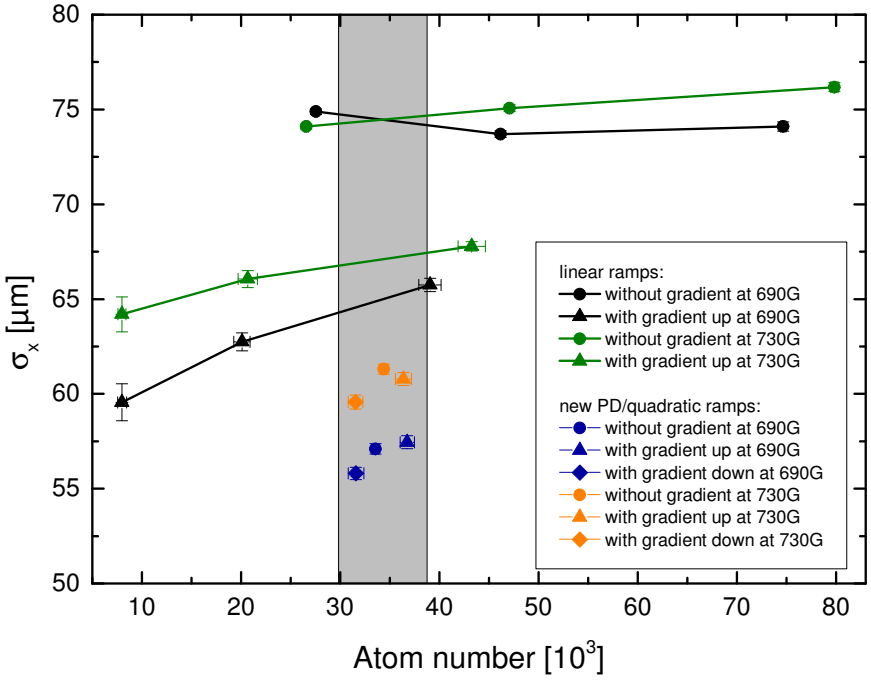

Figure 5.7.: **Effect of quadratic evaporation ramps and spilling in ODT on the cloud temperature in the pancake trap.** The decrease in temperature was here inferred from a smaller Gaussian width σ_x of the cloud in horizontal direction. 'Gradient off' corresponds to the case where gravity is compensated by the MOT gradient whereas 'gradient up/down' labels either a overcompensation or a gradient smaller than gravity.

As mentioned in Section 4.3.3 the atoms are cooled in the ODT by evaporative cooling. So far we decreased the power of the ODT beams linearly and, as seen in Figure 5.7, we can clearly see that the spilling technique (green, black triangles) leads to a $\sim 25\%$ colder sample. To improve the evaporative cooling in the ODT we change the gain factor of the low power photodiode by switching to an operational amplifier with an increased gain factor of 300. This reduces the beam noise and makes the evaporation in this low power regime even more stable. Further we replaced the linear ramps by quadratic ramps with the same relative slope in the beginning and end of the ramp. The orange 730G and blue 690G data shows a further decrease in temperature of $\sim 27\%/44\%$ for no spilling at 730G/690G, $\sim 17\%$ for spilling at 730G and $\sim 21\%$ for spilling at 690G in the ODT. In the measurement 'gradient down' labeled by the diamonds we decreased the gradient so far, that it does not even compensate gravity anymore. Thus, the atoms can leave the trap due to the gravitational gradient. This leads to a $\sim 7\%$ decrease of the cloud temperature in the pancake trap. Hence,

the implementation of the quadratic ramps was quite efficient, whereas the decrease in temperature due to the spilling technique is only on the order of 9%. To summarize we can estimate for the non-spilled data a temperature of 115nK at $\sigma_x = 74\mu$m and a final temperature of 73nK at $\sigma_x = 59\mu$m.
To achieve further cooling during the transfer of the cloud, we lower the adiabatic compression in the end of the evaporation to obtain a better phase space overlap between the ODT and the single pancake potential. In doing so, we always verified loading into one single pancake which could be achieved up to a compression depth of 2.1μK for a small number of transferred particles of about 25000 per spin state. The temperature decrease obtained due to lowering the adiabatic compression depth from 3.6μK to 2.1μK was about 6%. However, a decreased compression depth limits us automatically in the number of transferred atoms and thus we had to develop another technique which is similarly effective in cooling and sets no limitation on the atom number in a single pancake.
We had the idea to first transfer more particles into the single pancake trap by restoring the compression depth to 3.6μK and increasing the final trap depth of the evaporation process to 0.03μK. After transfer we remove the hottest particles by applying the spilling technique directly in the pancake potential. This allows us to control the particle number directly in a single pancake and perform optimal cooling of the sample in one step. In Figure 5.8 the procedure with optimized ramp times and trap levels

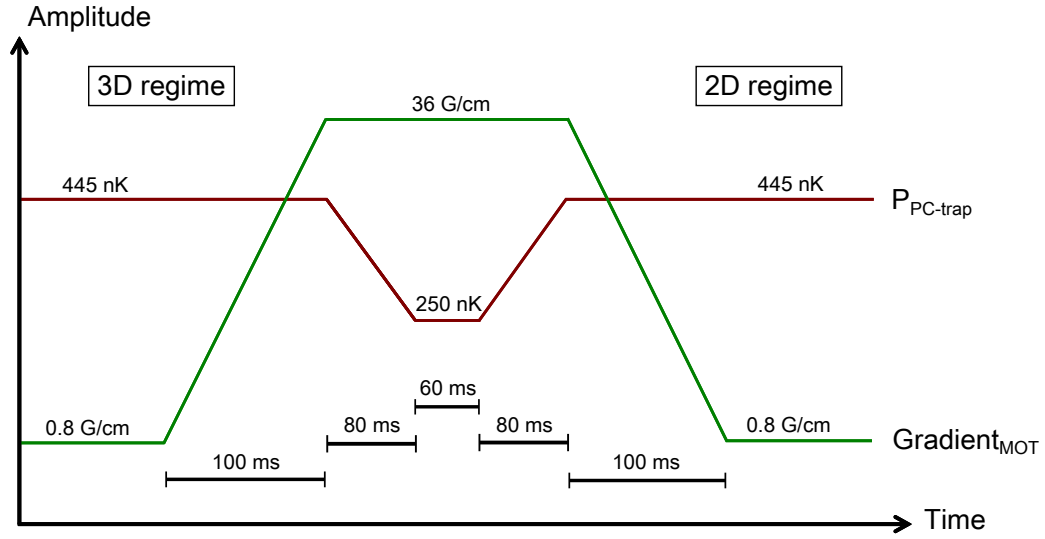

Figure 5.8.: **Schematic description of the spilling process in the pancake trap.** We increase the MOT gradient (green) from gravitation compensation up to 36G/cm while we decrease at the same time the power of the pancake trap beams (red) to the desired trap depth. Here we lower the optical potential down to 250nK which leads to about 50000 atoms in a single pancake trap after increasing the power to the original value of 445nK.

is schematically depicted. With these settings we are now able to load about 100000 atoms per spin state at a trap depth of 295nK into a single pancake potential. By performing the spilling method down to a number of particles of about 43000, we obtain a decrease in temperature from 75nK down to 63nK. Thus we can now tune the atom number by slightly decreasing and increasing the depth of the pancake potential at a fixed gradient of about 36G/cm, and check at which number of particles we fulfill the 2d-ness condition as described in the next section.

5.5. Entering the quasi-2d regime

As introduced in the beginning of Chapter 3 the quasi-2d regime can be defined by the condition $k_B T, \mu, E_F \ll \hbar\omega_z$. We obtained a large spacing between the individual energy levels $\hbar\omega_z$ by an extremely tight confinement in the vertical direction and in addition implemented several methods to efficiently cool the trapped sample. We are thus able to freeze out the vertical degree of freedom meaning that due to thermal excitations on the order of $k_B T$ the trapped particles cannot populate excited energy levels in the z-direction. Thus, only the lowest radial trap levels are still populated because T is larger than zero. By loading more and more particles in the trap, higher excited radial energy levels become stronger occupied and hence, at a certain critical atom number even the first excited trap level in vertical direction will be populated. As shown in Section 3.2.4 the fermionic character of the cloud allows us to find a maximum atom number before populating the first excited vertical trap level just by counting the number of available radial states. We calculated the number to be about 51200 particles per spin state for our pancake trap potential. This number limits the quasi-2d regime under ideal conditions at $T = 0$ and gives therefore only an upper limit.
However, inspired by the work of [Dyk10] we investigated how the expansion of a weakly interacting Fermi gas changes when the system becomes quasi-2d. Therefore we transfer a mBEC into a single pancake potential and ramp the magnetic offset field up to 1400G where the unbound atoms now form a degenerate Fermi gas. Due to the transfer into a single pancake potential we have to prepare the Fermi gas on the right side of the 3d Feshbach resonance as mentioned earlier in Section 5.2. Since interactions will influence the expansion of the cloud, we ramp to such high magnetic fields to be as weakly interacting as possible.
Further we apply the spilling technique described in the last chapter to tune the number of atoms and image the width of the cloud from the side by absorption imaging of one spin state after a 3ms time-of-flight. In doing so, we are able to extract the Gaussian width of the cloud as a measure of the expansion in vertical direction. By decreasing the trap depth from 294nK to 223nK we can change the atom number between 100000 and 9700 and thus tune the level of the Fermi energy E_F. Hence, we investigate the crossover between populating as well energy levels above the first excited vertical energy level and only occupying radial trap levels below the first vertical excited level. Since we probe here an ensemble of particles, the vertical expansion of each particle only occupying

the radial trap levels below the first vertical excited level can be described by the single-particle ground state wave function of the quantum harmonic oscillator (QHO) in vertical direction. Thus, in this regime the vertical cloud width is expected to stay constant in a purely ballistic expansion since the ensemble expands with the momentum given by the curvature of the single-particle wave functions. This measurement allows us to determine precisely the number of atoms we are allowed to load into a single pancake trap to be in the quasi-2d regime. We verified loading into a single pancake by performing an rf-tomography right after the measurement.

In Figure 5.9 the measured data is depicted and a clear kink in the cloud width

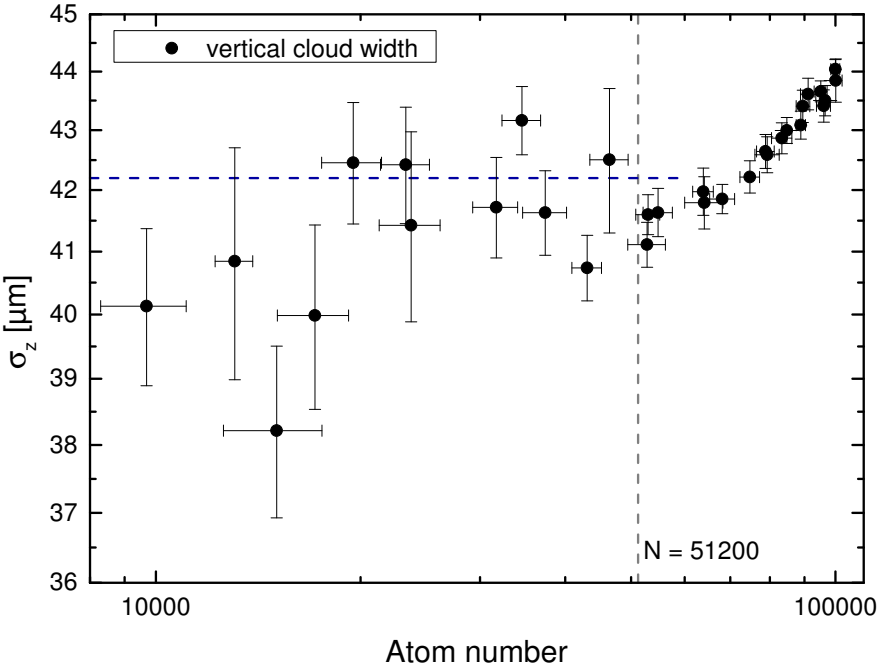

Figure 5.9.: **Transition between the quasi-2d regime and the 3d regime.** By tuning the atom number and monitoring the vertical cloud extension one can determine the atom number where the first excited vertical trap level becomes populated. The gray dashed line marks the estimated critical atom number N from Section 3.2.4. The regime of almost constant cloud width corresponds to the quasi-2d regime and the blue dashed line is the calculated width of the density distribution of the vertical harmonic oscillator single particle ground state.

around 60000 trapped particles[7] is visible, referring to the regime of $E_F \leq \hbar\omega_z$. The

[7]atom number corrected by factor 1.7 due to imaging

gray dashed line corresponds to the calculated atom number of 51200. Thus, we are able to observe the transition from the 3d regime to the quasi-2d regime by decreasing the number of trapped atoms. We further see, that by loading up to about 55000 atoms into a single pancake trap we are able to prepare a quasi-2d system.
For larger atom number, if the threshold of populating higher levels is crossed, the vertical momentum of the expanding particle ensemble is defined by both the single-particle ground state wave function and the wave function of the first excited state. This leads to the linear increase of the cloud width, since more and more atoms populate radial levels above the first excited vertical level and hence exhibit larger momenta due to the steeper curvature of the first excited vertical single-particle wave function. Thus by increasing the atom number, the ratio of atoms with larger vertical momentum grows which is measured as the increase of the cloud width.
We see further that the error of the atom number detection grows when we leave less and less atoms in the trap. This can be explained by the signal to noise ratio which gets worse for less atoms affecting the Gaussian fit. Nevertheless, for decreasing atom number the Gaussian width of the cloud in vertical direction tends to an almost constant value. We estimated the expected cloud width σ_z in the 2d regime by calculating the width of the density distribution of the single particle ground state in a quantum harmonic oscillator after a ballistic expansion of $t = 3$ms. The time evolution of the QHO-ground state wave function is thereby given by a free dispersion of a Gaussian wave packet whose width evolves in time according to

$$\sigma_z = \sqrt{\frac{\hbar}{2m_{Li}}\left(\frac{1}{\omega_z} + \omega_z t^2\right)}. \tag{5.6}$$

A more detailed derivation of this equation and connection to the Gaussian width σ_z is given in the Appendix A.1. This leads to an expected Gaussian width of $\sigma_z = 42.2\mu$m which is represented by the blue dashed line in the plot and confirms that we are only populating the vertical ground state in this regime.
In this chapter we presented the realization of a quantum degenerate system in a quasi-2d environment under controlled conditions. The next chapter contains a summary of the first measurement results concerning the interesting physical properties of this sample.

6. Measurements in a quasi-2d quantum degenerate sample

In this chapter we will present the first measurement results we obtained for a repulsively interacting quasi-2d quantum gas. Therefore we transferred a molecular BEC into a single pancake potential and decreased the Fermi energy to enter the quasi-2d regime. Since we perform in this thesis mainly time-of-flight measurements we want to give a short introduction to this common measurement technique in Section 6.1. Then we investigate the density distribution of the expanding cloud after short time-of-flight as described in Section 6.2 and Section 6.3. In Section 6.4 we focus first on the matter wave focusing technique we use to image the in-situ momentum distribution after a long time-of-flight of the sample. We close the chapter by discussing the obtained measurement results.

6.1. Time-of-flight measurements

In the following measurements we investigate the density distribution of a repulsively interacting quantum gas after releasing the sample from the highly anisotropic, pancake shaped, optical dipole trap and let it expand in space for a certain time-of-flight. Then we image the sample from above by absorption imaging as described in Section 4.5.
Since we prepare a repulsive interacting sample the interactions in the cloud lead to a hydrodynamic expansion. We minimize these interactions by suddenly switching off the optical potential. Thus the particles expand instantaneously and the transformation of the interaction energy into the kinetic energy is faster achieved which minimizes the effect of interactions during the release. Furthermore is the interaction energy at 692G where we perform the measurements presented in this thesis relatively small compared to other fields of repulsive interactions, as can be seen in Figure 2.6. Hence, we achieve an almost ballistic expansion and a single particle of the cloud at position x_0 and velocity v_0 will be placed at the position $x(t) = v_0 t + x_0$ after a time-of-flight of t.
We can define two different regimes: one regime of short time-of-flight where the initial position of the particles in the cloud x_0 and the remaining interactions still influence the density distribution after tof.
In the regime of long time-of-flight where $v_0 t >> x_0$ the distribution after tof is dominated by the initial momentum distribution and the expansion of the gas is almost pure ballistic. Further the saddle point of the magnetic field provided by the Feshbach coils will affect the expansion of the cloud. Since $v_0 t >> x_0$ the particle position $x(t)$ will

reflect the in-situ velocity of the particle v_0 and hence its momentum $p = mv_0$. Approximating Δx_0 as the in-situ cloud extension of $\Delta x = 150\mu$m and $\Delta v_{thermal} = 0.009$m/s as the initial thermal velocity at a temperature $T \approx 60$nK leads to a time-of-flight (tof) of $t > 17$ms to enter this regime. Since we can normally achieve a maximal tof of about $t = (8 - 10)$ms[1] in the experiment we are on the edge of this regime. As we will see in Section 6.4 due to the influence of the magnetic field saddle we can directly map the in-situ velocity distribution onto the imaged density distribution in this regime after a shorter time-of-flight.

6.2. Observation of density fluctuations

We imaged the trapped molecular Bose gas from above at a magnetic offset field of 692G after short time-of-flight. In this field region the 2d molecular binding energy given by $E_{B,2D}$ is much larger than the Fermi energy $E_F \ll \hbar\omega_z$ as depicted in Figure 3.2. Thus the transferred particles are deeply bound into molecules. Figure 6.1 a) shows an in-situ image of the cloud of molecules in a single pancake potential. By releasing the atoms from the trap and imaging them after a time-of-flight of 4ms from above we observe fluctuations in the density distribution of the cloud as seen in Figure 6.1 b). To confirm the random nature of the density fluctuations we average 35 images and the density fluctuations vanish in the resulting image which is depicted in Figure 6.1 c).
Besides that, we investigated a fragmentation into a thermal and a 'quasi'-condensed part. We call the second part 'quasi'-condensed, because it is significantly different from the thermal part and due to the 2d-ness of the system it can not be a real condensate since we are not cold enough to establish true long range order. To quantify this separation we fitted the density distribution after integrating it along one direction, with a 1d bimodal function consisting of a thermal Gaussian part (red dashed line) and a Thomas-Fermi parabola (blue) describing the 'quasi'-condensed part. To improve the fits for the individual shots, we used the result from a 1d bimodal fit of the averaged data as start parameters. As can be seen in Figure 6.1 d) the Thomas-Fermi approximation (blue) describes the data rather good and a significant deviation from the thermal part fitted by the red Gaussian distribution can be observed. In a next data processing step, we isolated the density fluctuations from the mean density distribution by fitting the single raw data image in Figure 6.1 b) with a 2d bimodal distribution. We subtracted the obtained fit function from each single image which results in the image seen in Figure 6.1 e). Moreover, we extracted the Thomas-Fermi radius from the 2d bimodal fit, which can be related here to the extension of the 'quasi'-condensed part. The size of the Thomas-Fermi radius is about 20 pixel which corresponds to 65μm with our imaging setup and plotted as the black dashed circle in both the single raw data image b) and image e) depicting the isolated density fluctuations.

[1] By releasing the atoms slowly a larger tof can be achieved, but interaction effects are increased as well.

From that we can observe that the density fluctuations only appear in the 'quasi'-condensed part. Due to the two facts that the density fluctuations can only be ob-

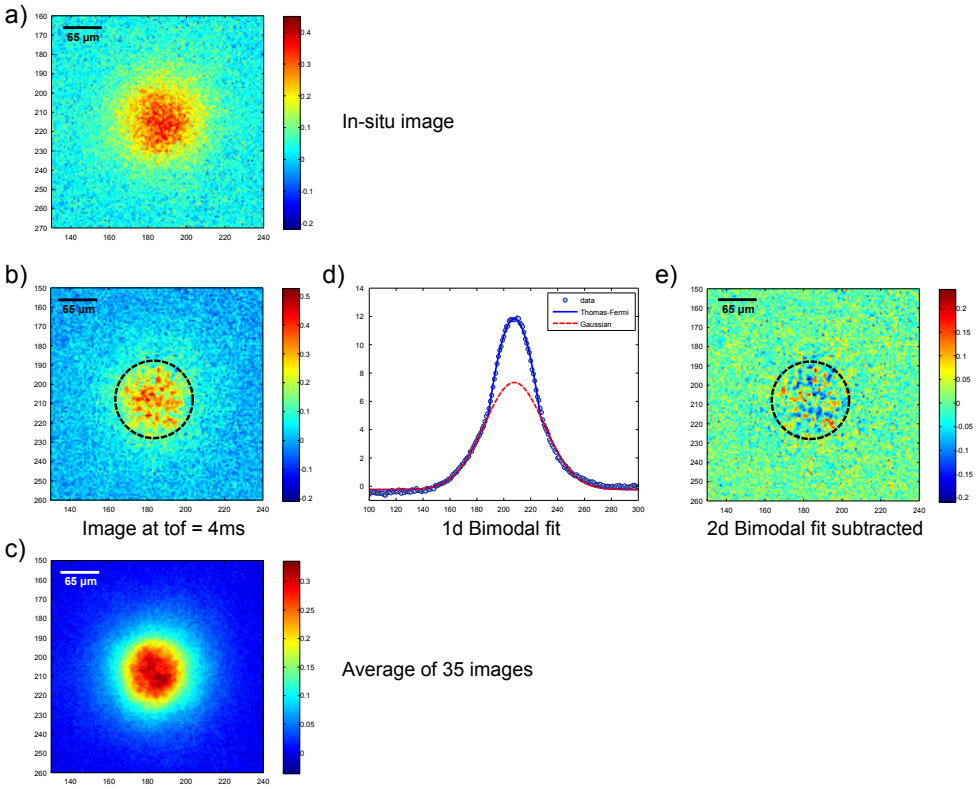

Figure 6.1.: **Density fluctuations in the 'quasi'-condensed part of the cloud.** In a) we present an in-situ image of a transferred mBEC in the 'quasi'-2d regime the x- and y-axis are given in pixel (1pix = 3.258μm) and the color corresponds to the optical density. After a certain time-of-flight (tof) we observe density fluctuations in a 'quasi'-condensed part which was determined by a 1d bimodal fit to the data as seen in d). c) shows the randomness of the density fluctuations since they vanish when averaged over many images. We isolated the density fluctuations as depicted in e) by subtracting a 2d bimodal fit from the image seen in b). The black dashed circle limits the 'quasi'-condensed part since its radius corresponds to the Thomas-Fermi radius extracted from the 2d bimodal fit.

served in a 'quasi'-condensed part and that they need a certain time-of-flight to emerge in the cloud we attribute them to an self-interference phenomenon. Since interference is strongly connected to a fixed phase relation between two or more interfering objects and since we only see random interference pattern, we think, that a from shot to shot varying local phase coherence $\theta(\mathbf{r})$ in the in-situ density distribution has to exist. Due to the interference of patches of constant phase the maxima and minima in the density

distribution are then formed.
Since in quantum mechanics, the velocity field at non-zero density is given by $\mathbf{v} = \frac{\hbar}{m}\nabla\theta(\mathbf{r})$ these local phases $\theta(\mathbf{r})$ introduce a velocity to the particles in the density distribution. After really short time-of-flight the repulsive interaction is still dominant in the cloud acting against the velocity from the phase gradient and the density distribution is not perturbed as seen in the in-situ image in Figure 6.1 a). When the interaction decreases during longer time-of-flight the introduced velocity influences the motion of the molecules more and more leading to fluctuations in the imaged density.
The condensate density of a true BEC is characterized by a true long range order in 3d and might be realized in a finite 2d system at very low temperatures as discussed in Chapter 3. However, such a condensed system would be described by only one global phase θ, thus a true long range phase coherence, and hence one would observe no interference after time-of-flight. Further would the velocity field $\mathbf{v}$ be zero since θ is independent of $\mathbf{r}$. On the other hand, in a purely thermal gas the length scale of local phase coherence is exponentially suppressed which results in a strong decoherence in the sample.
Nevertheless, in two dimensional repulsively interacting systems the phase transition to a superfluid is described by the Berezinskii-Kosterlitz-Thouless (BKT) theory which is characterized by an emergence of a topological order due to pairing of vortices with opposite circulation. This topological order leads to an algebraic decay of the order parameter ψ in space which corresponds here to the macroscopic wave function of a Bose gas. Since the density fluctuations are suppressed on a length scale $r > \xi, \lambda$ the remaining freedom in the order parameter is the phase which decays algebraically leading to a local phase coherence. The coherence length depends on the phase space density as seen in Equation 3.58, thus mainly on the temperature of the sample. For decreasing temperature T below T_{BKT} the patches of local phase coherence become larger whereas they vanish for $T > T_{BKT}$ since the proliferation of free vortices as a source of phase fluctuations destroys the local phase coherence. Due to that, we interpret the density fluctuations shown in Figure 6.1 as an indication that we entered the BKT-phase.

6.3. Analysis of density fluctuations

We introduced in Section 3.2.1 the first-order correlation function $g_1(r) = \langle\psi^*(\mathbf{r})\psi(0)\rangle$ as a measure for long range order in a quantum system thus the phase coherence. Since the first-order correlation function $g_1(r)$ can be connected to the two-point density correlation function $g_2(\mathbf{r}_1, \mathbf{r}_2)$ [CCT11], we analyzed the fluctuations by a density-density correlation function to get access to the first-order correlation function.

6.3.1. Density-density correlation function

The definition of the density-density correlation function we use in our analysis can be found in [Wen13]

$$G(\delta\mathbf{r}) = \frac{1}{\#_{\delta\mathbf{r}}} \sum_{r} \frac{\delta n(\mathbf{r}) \cdot \delta n(\mathbf{r}+\delta\mathbf{r})}{\bar{n}(\mathbf{r}) \cdot \bar{n}(\mathbf{r}+\delta\mathbf{r})}. \tag{6.1}$$

The summation is done for a fixed $\delta\mathbf{r}$ over all positions $\mathbf{r}$ inside the quasi-condensed part where the corresponding position $\mathbf{r}+\delta\mathbf{r}$ is inside the quasi-condensate as well. In order to motivate and explain Equation 6.1, Figure 6.2 depicts a simplified sketch of the different parts of $G(\delta\mathbf{r})$ applied to a 1d density distribution. Figure 6.2 a) shows the fluctuations on the density distribution (red) and the average density[2] $\bar{n}(\mathbf{r})$ (blue). In Figure 6.2 b) the average density is subtracted from the total density to obtain the density fluctuation $\delta n(\mathbf{r}) = n(\mathbf{r}) - \bar{n}(\mathbf{r})$. To further weight the fluctuations $\delta n(\mathbf{r})$ with the average density $\bar{n}(\mathbf{r})$, we divide $\delta n(\mathbf{r})$ at each point by the average density $\bar{n}(\mathbf{r})$ at this point which can be seen in Figure 6.2 c). Now to calculate the density-density

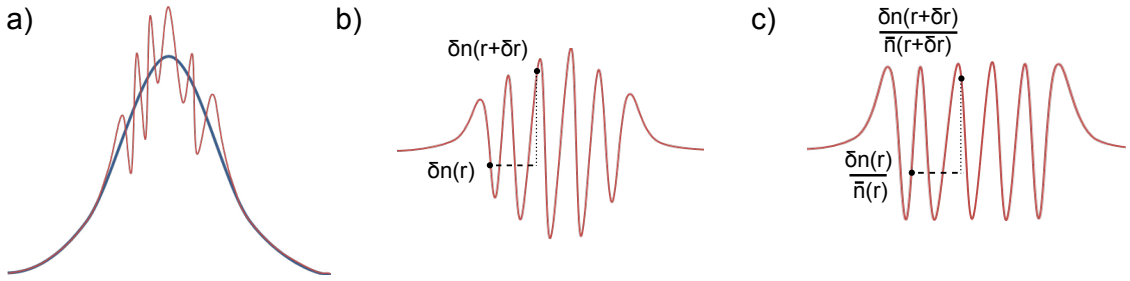

Figure 6.2.: **Sketch of the density-density correlation function.** In a) the 1d mean density $\bar{n}(\mathbf{r})$ is schematically depicted in blue while the density fluctuations are shown in red. By subtracting $\bar{n}(\mathbf{r})$ the fluctuations become isolated as seen in b). By weighting the fluctuations $\delta\mathbf{r}$ with the corresponding mean density $\bar{n}(\mathbf{r})$ at each point one obtains a sort of normalized fluctuation c) which will contribute in equal parts to the correlation function.

correlations $G(\delta\mathbf{r})$ for a fixed distance $\delta\mathbf{r}$, we multiply the weighted fluctuations at positions $\mathbf{r}$ and $\mathbf{r}+\delta\mathbf{r}$. Since we have a non-homogeneous system and only want to have the correlation of the quasi-condensate part, we perform the summation over all positions $\mathbf{r}$ inside the quasi-condensate part where the correlated position $\mathbf{r}+\delta\mathbf{r}$ is inside the quasi-condensate part as well[3]. Hence to have a normalized $G(\delta\mathbf{r})$ one has to divide by the number of terms $\#\delta\mathbf{r}$ in the summation and thus one obtains for larger $\delta\mathbf{r}$ less statistics. By applying this procedure to the single absorption images we achieve

[2] We determine the average density distribution by fitting the 2d image with a 2d bimodal distribution.
[3] We use a radius $r_{corr} = 8$pix and thus $0 < \delta\mathbf{r} \leq 2r_{corr}$.

for each image an axial symmetric two dimensional image[4] representing $G(\delta\mathbf{r})$. We average these images over the whole stack of absorption images to increase the signal of the correlation function. In addition we radially average the resulting $G(\delta\mathbf{r})$ to get a better access to the contrast.
Furthermore, the group of L. Mathey in Hamburg is currently investigating the two-point correlation function of two-dimensional bosonic systems from a theoretically point of view. They calculated the $g_2(\mathbf{r}_1, \mathbf{r}_2; t)$[5] numerically for both the quasi-condensed phase $T < T_{BKT}$ and the high temperature phase $T > T_{BKT}$ in real space and determined an analytical solution for both regimes in momentum space [Sin13]. In Figure

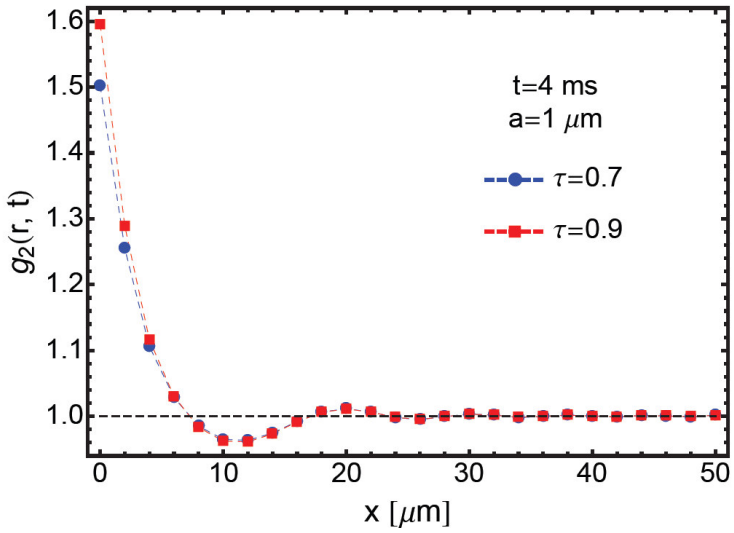

Figure 6.3.: **Theoretical prediction of the radial averaged $\mathbf{g_2(r;t)}$ for $\mathbf{T < T_{BKT}}$.** Here a homogeneous, weakly interacting bosonic ^{6}Li dimer system was assumed after a purely ballistic expansion of $t = 4$ms. The parameter τ is proportional to the temperature and a describes a cutoff parameter for finite systems given by $a = \lambda^2/2\pi\xi$, where λ is the thermal de Broglie wavelength and ξ is the healing length related to the interaction. The plot is obtained from L. Mathey by private communications.

6.3 their prediction for the radial average of the $g_2(\mathbf{r}, t)$ in the quasi-condensed phase for two different temperatures labeled by the parameter τ is depicted. Here, they performed the calculation for a bosonic system of ^{6}Li-dimers after a time-of-flight of $t = 4$ms. The parameter τ is closely related to the critical exponent of the algebraic decaying first order correlation function $g_1(r)$ and runs from 0 to 1 as the temperature is increased from 0 to T_{BKT}. They found out, that for increasing τ, $g_2(\mathbf{r}, t)$ increases

[4]The two diagonal adjacent quadrants contain the same information.

[5]For homogeneous system $g_2(\mathbf{r}_1, \mathbf{r}_2; t)$ is given by $g_2(\mathbf{r}; t) = \frac{\langle \hat{n}(\mathbf{r},t)\hat{n}(0,t)\rangle}{n_{2d}^2} - \frac{\delta(\mathbf{r})}{n_{2d}}$ where the first term describes the density-density correlation and the second term corresponds to the shot-noise that originates from the quantum nature of the bosonic operators.

for small distances (here $x < 10\mu m$). Further they observed an oscillatory behavior which depends on the critical exponent τ. This oscillatory behavior vanishes in their calculations for a sample at $T > T_{BKT}$.

We observed an indication of this oscillatory behavior[6] in our experiment as seen

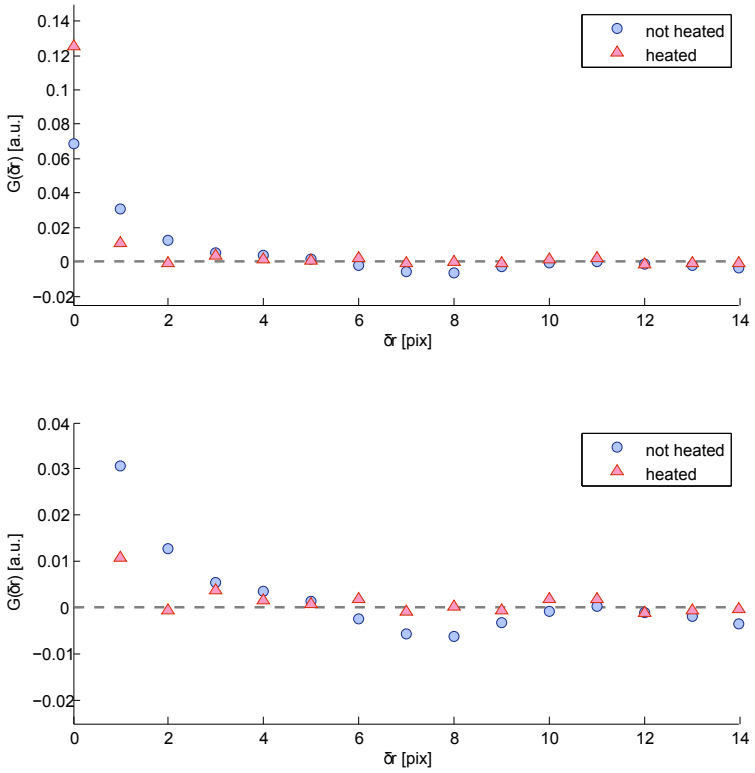

Figure 6.4.: **Radially averaged G(δr) for a mBEC after 4ms tof at 692G.** The upper plot depicts the obtained data for a non-heated sample at about 60nK (blue) and the data of a heated sample (red) at about 120nK. The increased $G(\delta\mathbf{r})$ of a heated sample at small distances $\delta\mathbf{r}$ can be seen. In the lower plot we rescaled the data to better visualize the enhanced oscillatory behavior of the non-heated data.

in Figure 6.4. The blue data represents the radial average of the $G(\delta r)$ correlation function for the transferred molecular BEC at 692G after 4ms time-of-flight presented in the previous section. Furthermore, we observed a significantly increased correlation function for small distances $\delta r < 4\text{pix} \cdot 3.258\mu\text{m/pix} \approx 13\mu\text{m}$ which is larger than the theoretical prediction. The red data corresponds to an identically prepared system but here we heated the cloud by shaking the optical pancake potential for a certain time. Therefore we modulate the diffraction efficiency of the AOM with a sine function. The amount of heating is then set by the length of modulation (here about 600ms) and the

[6]The oscillation occurs in our measurement around 0 whereas the theoretical calculation oscillates around 1 due to the slightly different definition of the numerator in the correlation function.

amplitude of the sine. In the presented data we heated the cloud from about (60±10)nK up to (120 ± 10)nK and observe a decrease in the oscillation. Further the increase of the $G(\delta r)$ for small distances of the heated sample is in qualitative agreement with the theoretical predictions. From theory we know that the oscillatory behavior of the density-density correlation is an indicator for the BKT phase and closely related to the critical exponent τ.
Unfortunately, we observed a strong correlation between the measured oscillation in the $G(\delta r)$ and the detuning of our imaging laser as depicted in Figure 6.5. Here we imaged the quasi two dimensional bosonic system at the same magnetic field and time-of-flight as above. Also, we performed this measurement before implementing the current modulation of the imaging laser discussed in Section 4.5.3. For the orange data we detuned the imaging light to the effective resonance of the particles. This means, that we detuned the imaging light with a pulse duration of 8μs to the point where we detect the maximum number of atoms. We could observe oscillations with a similar amplitude as for the non-heated data in Figure 6.4. By detuning our imaging laser with respect to the effective resonance by $\Delta = \pm\Gamma$, where Γ corresponds to the 5.87MHz natural linewidth of the D_2-transition in ^{6}Li, we observed an enhanced amplitude and a phase shift of the oscillation as seen in the blue and red data in Figure 6.5.
Due to the correlation between the oscillation of the density-density correlation function and the detuning of the imaging laser, it is rather complicated to quantitatively interpret the oscillatory behavior or to extract the critical exponent τ. Furthermore, as seen in Figure 6.4, we obtain a very low signal from this measurement approach, although we have good statistics due to radially averaging the data. Comparing the data to the theoretical predictions of the group of L. Mathey is problematic as well, because they assume in their calculations a weakly interacting homogeneous sample and a purely ballistic expansion. Therefore we choose a correlation radius r_{corr} of 8pix to be mainly in the center of the quasi-coherent part where the density is relatively homogeneous. Nevertheless our $\tilde{g}$ is about 0.6 at 692G and thus we are in a regime of intermediate interactions which makes our expansion not purely ballistic. Because of all these difficulties, we investigated a different and more elegant method to quantify the quasi-long-range order in our bosonic quasi-2d quantum gas.

6.4. Imaging the momentum distribution

Another possibility to get access to the first order correlation function $g_1(r)$ can be obtained via the momentum distribution of the cloud. As shown in Equation 3.10, $g_1(r)$ for an ideal gas can be connected to the Fourier transformed of the momentum distribution $n_k = n(k)$.
In the beginning of this chapter we already motivated the possibility to map the initial momentum distribution on the imaged density distribution for a long time-of-flight measurement. We estimated this long tof-regime to be at around tof $>$ 17ms which

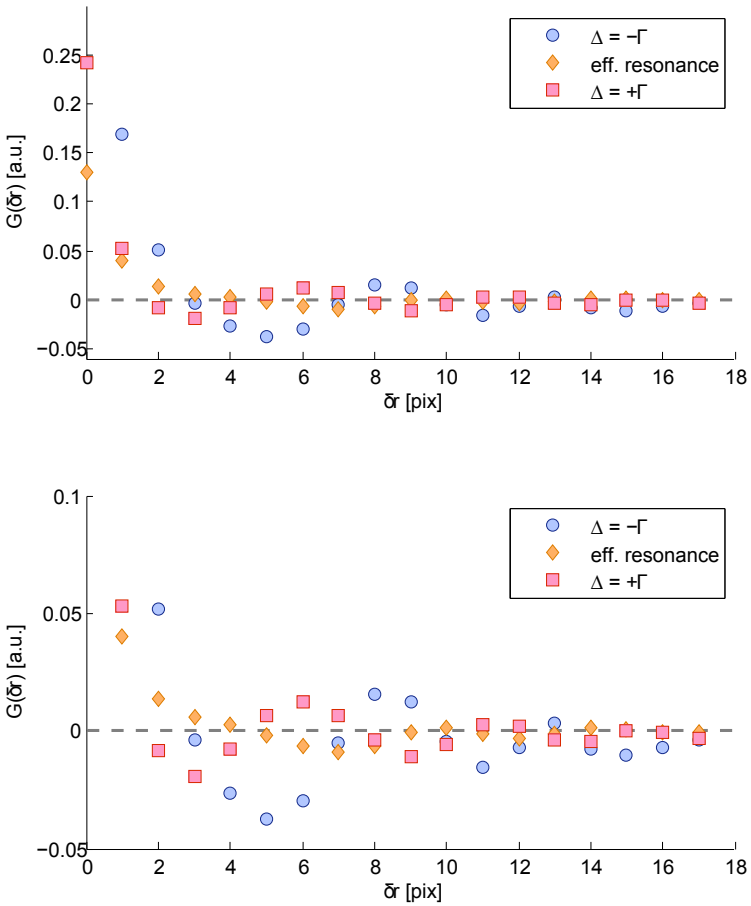

Figure 6.5.: **Correlation between the G(δr) oscillation and the detuning of the imaging light.** By detuning our imaging laser by $\Delta = \pm\Gamma$ with respect to the effective resonance, we observed an increase in the amplitude and an additional phase shift of the oscillations.

is not accessible in a free space time-of-flight due to the enhanced expansion in the vertical direction.
However, we developed a technique to map the in-situ momentum distribution on the density distribution of our expanding particles which we call matter wave focusing technique.
During the process of development we were inspired by the optical diffraction experiment of a plane wave which is diffracted by an arbitrary aperture. In the far-field limit the obtained intensity distribution corresponds to the squared absolute value of the Fourier transformation of the aperture. This mapping is similar to what we want to achieve and so we looked how the problem of accessing the far-field plane is solved in optics.
To reduce the distance between the aperture and the plane of the far-field image, one adds a thin lens after the aperture. As we know from Fourier optics a lens can be

described by a phase factor $\sim \exp(i\pi r^2)$ due to the curvature of the lens. Hence, an incoming plane wave $\psi(z,t) = A_0 \exp(ik_z z)$ adds up an additional phase $\phi_{lens} \sim i\pi r^2$ when passing through the lens. This modifies its wave front to be parabolic and the wave converges towards a point in the focal plane of the lens at distance f. The intensity distribution in the back focal plane of the lens is then given by the square of the absolute value of the Fourier transform of the wave in the input plane plus an additional phase factor, which vanishes if the distance between aperture and lens matches with f as well. Thus, the far-field image can be imaged after a distance of $2f$ [Sal91].

6.4.1. Matter wave focusing technique

The imprinting of the 'phase factor' is realized by the harmonic magnetic confinement $V_{mag}(r) = \frac{1}{2} m\omega_{r,mag}^2 r^2$ in radial direction due to the saddle point of the Feshbach field which affects the particle expansion predominantly after long time-of-flight. We assume the cloud expansion as ballistic in this direction since most of the interaction energy will be already released in the vertical direction. Thus, we can treat the motion of each expanding particle independently.
In this single particle picture each released molecule will perform a harmonic oscillation in the magnetic potential dependent on its initial momentum $p(t=0)$ which can be described by $r(t) = A\sin(\omega_{r,mag}t)$ and $\dot{r}(t) = A\omega_{r,mag}\cos(\omega_{r,mag}t)$ respectively. With an oscillation period of $T = 2\pi/\omega_{r,mag}$ one can easily see, that if $t = T/4$ one obtains $r(T/4) = A = p(0)/m\omega_{r,mag}$.

In Figure 6.6 the propagation of two molecules in the phase-space of the harmonic oscillator is depicted. The particles will evolve in time on the depicted circle dependent on its initial position $r(0)$ and momentum $p(0)$. From the equation of motion we already know the oscillation period of about $T = 2\pi/\omega_{r,mag}$. Thus, a particle at $r(0) = 0$ and finite momentum $p(0)$ will be mapped after an evolution time of $t = T/4$ in the phase-space to $r(T/4) = p(0)$ and $p(T/4) = 0$. The orange trajectory corresponds to a particle with finite initial position $r(0)$ and finite initial momentum $p(0)$ as most of the particles in the cloud. As can be seen this particle will evolve up to the second quadrant of the coordinate system leading to the fact that at $t = T/4$ its initial momentum $p(0)$ is projected on $r(T/4)$. Since we investigate an ensemble of expanding particles in the cloud with different momenta $p(0)$ and different $r(0)$ we will project at $t = T/4$ the whole in-situ momentum distribution $n(p,0)$ on the density distribution $n(r,T/4)$. As can be seen further in the blue trajectory of Figure 6.6 particles with low initial momentum will be detected at lower radii in the density distribution whereas particles with larger momentum will be detected at larger radii.
The error of the projection technique is larger for particles with larger initial position r(0) as can be estimated from the steeper curvature of the trajectory. The spread of the initial position $\Delta r(0)$ is given by the radial confinement of our pancake potential of about 200μm.
Since our horizontal magnetic trap frequency at 692G is about $\nu_{r,mag} = 10$Hz, we obtain

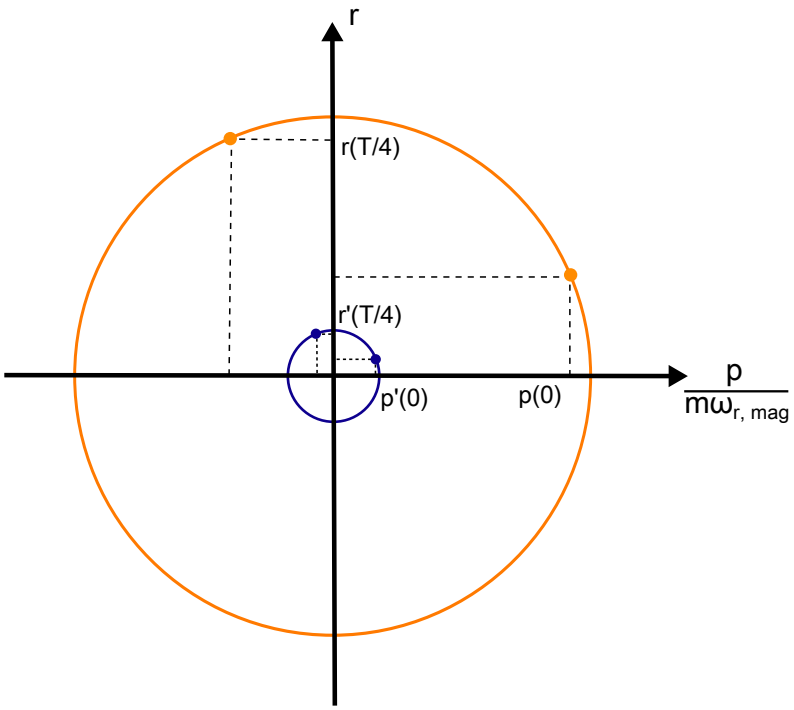

Figure 6.6.: **Phase space of the harmonic oscillator.** Here the trajectory of a single molecule with $r(0) \neq 0$ and large initial momentum $p(0)$ (orange) evolving in the harmonic magnetic confinement provided by the saddle point in radial direction is depicted. The blue circle corresponds to the trajectory of a molecule with low initial momentum $p'(0)$. At $t = T/4$ the initial momentum distribution of an ensemble of expanding molecules is projected on the density distribution and hence can be imaged.

$T/4 = 25$ms. Thus, after an expansion time of tof ≈ 25ms in the magnetic confinement we are able to image the in-situ momentum distribution of the horizontal plane.
An additional problem occurs due to the expansion of the cloud in the vertical direction. Since this is the direction of the tightest optical confinement and the axis of magnetic anti-confinement, the cloud expansion is much faster than in the radial direction. This leads to the fact that in the absorption image, although we are integrating the signal along the z-axis, after a time-of-flight of about $(8 - 10)$ms the atoms are out of the depth of focus. To solve this problem we apply the same technique as in radial direction and stop the vertical expansion by switching on the ODT at a trap depth of ~ 350nK for about 1.2ms shortly after releasing the molecules from the pancake trap. This leads to a slight modification of the radial trap frequency of the effective potential because ν_{ODT}^{weak}, $\nu_{ODT,painted}^{interm.}$ and $\nu_{r,mag}$ are on the same order, which results in $\nu_{eff} = 16$Hz. Since the ODT pulse duration is only about 1.2ms, thus $0.08 \cdot T/4$, the effective time-of-flight is given by tof $= 1.2\text{ms} + 0.92 \cdot 25\text{ms} = 24.2$ms at a magnetic field of 692G.

6.4.2. Momentum distribution of a quasi-2d quantum system

By applying the matter wave focusing technique to a quasi 2d molecular Bose gas at 692G we successfully imaged the in-situ momentum distribution of the molecules in radial direction as seen in Figure 6.7 a). Here a single image after a time-of-flight of 23ms is shown. The scale of the image is the same as the imaged density distribution in Figure 6.1 for a tof of 4ms. The density distribution is much more dense compared with the density distribution in Figure 6.1 which leads to a higher optical depth (color scale) reflecting the enhanced occupation of low momentum states. Thus similar to the short tof density distribution we observe evidences of a quasi-condensed part. Figure 6.7 c) shows the mean momentum distribution of 20 single images which have been all shifted to the same center. In order to quantitatively analyze the momentum distribution we perform a radial average of the raw data images. Figure 6.7 e) presents the resulting distribution of the averaged data in a semi-logarithmic representation. The significant increase of the distribution for low r^2 and thus low momenta is due to the enhanced population of these states. For $r^2 > 1000\mu\text{m}^2$ the distribution evolves linearly up to $r^2 \sim 7000\mu\text{m}^2$. We related this linear range to the thermal or non-condensed part and fitted it with a Maxwell-Boltzmann distribution

$$n(r) = A_0 \cdot \exp\left(-\frac{m_{dimer}\omega_{mag}^2 r^2}{2k_B T}\right), \tag{6.2}$$

with the free fit parameter: amplitude A_0 and temperature T. In doing so, we obtain the temperature of the thermal part from the wing of the momentum distribution. Assuming that both parts of the cloud are in thermal equilibrium we achieve a good estimate of the temperature of the prepared sample. During the fit procedure we optimized the lower ($r_{lb}^2 = 1600\mu\text{m}^2$) and upper bound ($r_{ub}^2 = 9400\mu\text{m}^2$) of the fit range in a way that the linear part of the momentum distribution is described best. By fitting each single image and average the obtained temperature over the whole stack we determined a cloud temperature of $T = (68 \pm 5)$nK. In Figure 6.7 e) the averaged fit to the averaged data is presented (red line).

Further we heated the sample by the same procedure as described in Section 6.3.1. By radial averaging the obtained images and fitting the linear part of the radial averaged momentum distribution as described above, we determined the temperature of the sample for each heating step. Thus we are able to image the momentum distribution by the matter wave focusing technique at different temperatures T. We observed a significant decrease in the occupation of low momentum states and even a vanishing quasi-condensate part for $T > (127 \pm 9)$nK.
Figure 6.7 b) shows a single image of the measured momentum distribution at $T = (134 \pm 9)$nK. The depicted image is dominated by the shot noise of the imaging and the momentum distribution can only be descried by averaging over several images as

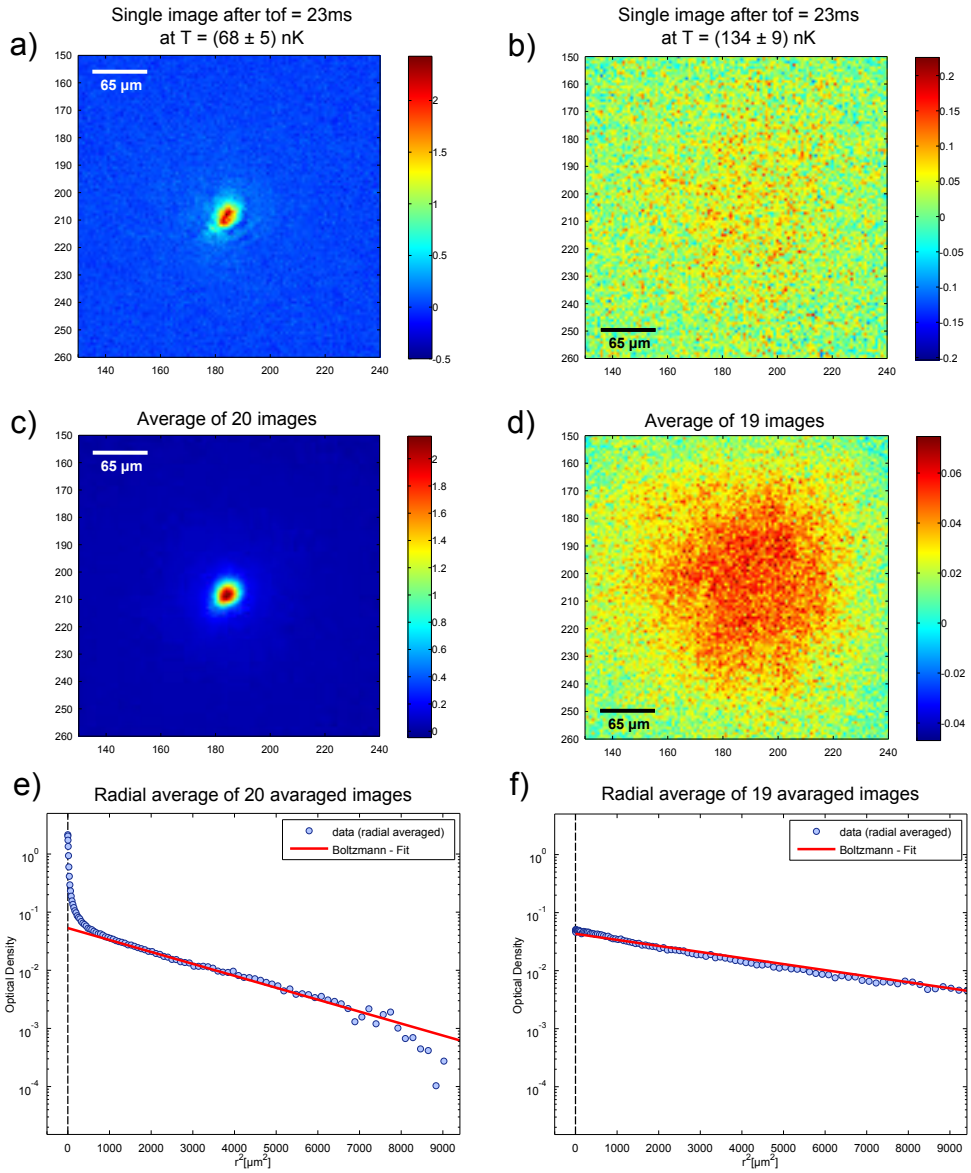

Figure 6.7.: **In-situ momentum distribution imaged by the matter wave focusing technique.** In the first row the single in-situ momentum distributions of the non-heated a) and heated b) sample are presented. The scale is in pixel and the color represents the optical density. In c) and d) the mean images over the whole data stack is shown. In c) the enhanced occupation of low momentum states is clearly visible whereas in the heated sample d) the whole momentum distribution is visible due to the absence of the enhanced population of low momenta. In e) and f) we perform radial averages of the 2d images and plotted the momentum distribution in a semi-logarithmic representation. The linear wing of the distribution was fitted by a Maxwell-Boltzmann distribution to determine the temperature. In e) the deviation from the Maxwell-Boltzmann fit for low momenta can be seen whereas in f) almost the whole data is linear.

shown in Figure 6.7 d). Due to the absence of an enhanced occupation of low momentum states the thermal momentum distribution becomes visible in the averaged raw data images. By comparing both the radial averaged data in Figure 6.7 e) and f) we observe on the one hand, that the low momentum occupation for the heated sample has vanished and on the other hand that the whole momentum distribution can be well described by a Maxwell-Boltzmann distribution. The less steep slope of the fit function reflects the increased temperature of the sample due to the heating process.
The temperature fits to the radially averaged data in the semi-logarithmic representation for each heating step can be found in the Appendix A.2. Figure 6.8 depicts the averaged temperatures determined for different heating steps from the Maxwell-Boltzmann fit to each single momentum distribution. We observed an almost linear increase in temperature which shows the effectiveness of the applied heating technique. Thus we can prepare the molecules in the quasi-2d regime at a temperature of (68±5)nK and are able to heat the cloud up to a temperature of about 130nK and beyond dependent on the heating.
In order to determine the critical temperature T_c at which the quasi-condensate part

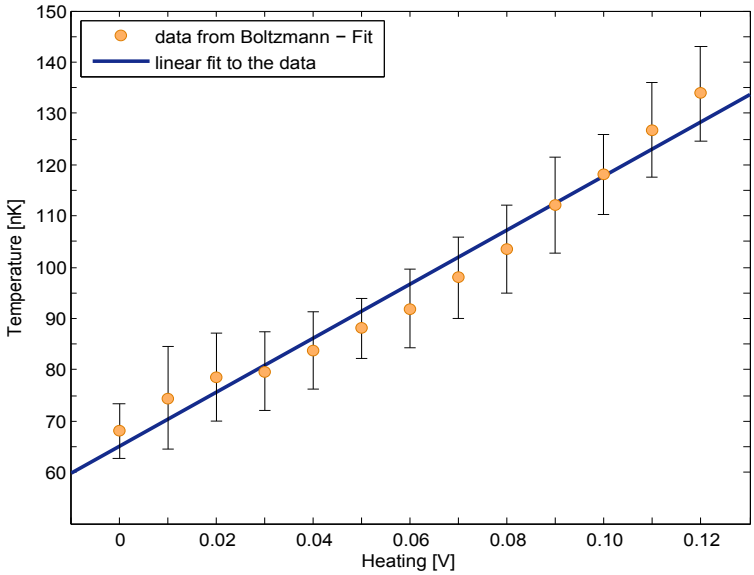

Figure 6.8.: **Temperature increase of the heated sample.** We heat the sample by modulating the trap depth of the single pancake trap by a sine function whose amplitude is given on the x-axis. The temperature obtained from a Maxwell-Boltzmann fit to the wing of the imaged in-situ momentum distribution was averaged over the whole data stack for each heating step. The almost linear increase was fitted by: $\mathrm{T}(\mathrm{A_{Heat}}) = 528.76\mathrm{nK/V} \cdot \mathrm{A_{Heat}} + 64.93\mathrm{nK}$.

vanishes, we extract for each temperature the quasi-condensate fraction N_c/N from the momentum distribution. To calculate the atom number of the quasi-condensate N_c we

subtracted the Maxwell-Boltzmann fit from the radial averaged momentum distribution of each single image. Then we numerically integrated the resultant distribution along r up to a cutoff estimated by the lower bound of the Maxwell-Boltzmann fit. The atom number of the thermal part was similarly obtained by numerically integrating the Maxwell-Boltzmann fit. Due to the radial averaging the quasi-condensate fraction is then given by

$$\frac{N_c}{N} = \frac{\sum_{i=1}^{lb} N_{i,c} r_i^2}{\sum_i N_{i,th} r_i^2 + \sum_{i=1}^{lb} N_{i,c} r_i^2}. \tag{6.3}$$

We further average the quasi-condensate fractions for each temperature T and assume that the systematical error due to the individual temperature fit is smaller than the statistical error. The result is presented in Figure 6.9 and a significant decrease of the quasi-condensate fraction for higher temperatures is visible.
From the BKT-theory we expect a jump in the superfluid density by crossing the critical temperature T_{BKT} from $n_s = 4/\lambda^2$ to zero due to the proliferation of free vortices. We observed a continuous decrease of N_c/N down to a finite value of about $N_c/N = 0.009 \pm 0.008$ at a critical temperature of $T_c = (127 \pm 9)$nK from Figure 6.8. The deviation from zero of about 0.007 can be explained by the small systematic error of the temperature fit as seen in the whole data set depicted in the Appendix A.2. This could be improved by fitting first the averaged radial averaged momentum distribution to obtain start parameter for the fit to the single image data.
To relate this temperature to the Fermi temperature of the trapped sample at 692G we assume that the superfluid will be formed first at the point of highest density thus in the center of the trap. The Fermi energy in the trap center is proportional to the in-situ peak density $E_{F,local}(T) \propto n_0(T)$ in two dimensions [7]. Thus, the Fermi energy at 692G can be written as $E_{F,692}(T) = c \cdot n_{0,692}(T)$. The proportionality constant c can be determined from the 2d-3d-transition measurement described in Section 5.5.
Since we always transfer about 50000 particles in the single pancake potential we are in the regime $E_F \approx \hbar\omega_z$ at 1400G. Due to the fact that we measured the in-situ peak density only up to a field of 900G we will assume in this calculation that $E_{F,900} \approx E_{F,1400} \approx \hbar\omega_z$. Thus we can write the proportionality constant as $c = \frac{\hbar\omega_z}{n_{0,900}}$ which leads to the following equation for the local Fermi energy at 692G

$$E_{F,692}(T) = \hbar\omega_z \frac{n_{0,692}(T)}{n_{0,900}}. \tag{6.4}$$

We obtained the corresponding temperature dependent in-situ peak densities $n_{0,692}(T)$ depicted in green in Figure 6.10 from the single shot in-situ density distribution at different temperatures T. With $\omega_z = 2\pi \cdot 5972$Hz the local Fermi temperature for 692G

[7] From LDA we know $E_F(r) = E_F - V(r)$ with $E_F(r) = \frac{(\hbar k(r))^2}{2m}$. The 2d density follows from the 2d analogue of the Fermi sphere, the Fermi circle $n(r) = \frac{\pi(\hbar k(r))^2}{(2\pi\hbar)^2}$. Substituting $E_F(r)$ and $k(r)$ leads to $n(r) = \frac{2m}{4\pi\hbar^2}(E_F - V(r))$ and since $V(r) = 0$ in the trap center we obtain $E_F \propto n_0$, $T_F \propto n_0$.

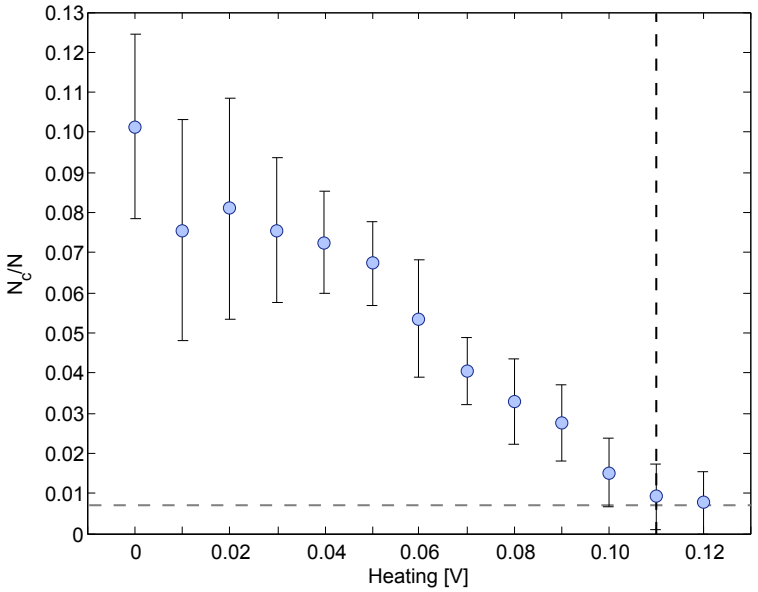

Figure 6.9.: **Quasi-condensate fraction of the heated sample.** We determined the quasi-condensate fraction N_c/N from each radially averaged momentum distribution at different temperatures as described in the text. The larger error for smaller heating is due to the enhanced shot-to-shot fluctuations of the low momentum occupation due to the radial averaging. The horizontal dashed line (gray) labels the offset of the distribution which can be related to the systematical error of the temperature fit. The vertical dashed line (black) marks the position we used to determine T_c.

can be calculated due to

$$T_F(T) = \omega_z \frac{\hbar}{k_B} \frac{n_{0,692}(T)}{0.11}, \tag{6.5}$$

for each cloud temperature T. The obtained values of T/T_F are plotted in blue in Figure 6.10 as well and one can see a clear linear increase in the dimensionless quantity. Since we only obtained in-situ densities up to a temperature of about 117nK we linear interpolated T/T_F to the regime of our critical temperature T_c. In doing so, we obtained the following linear fit function

$$\frac{T}{T_F} = -0.18455 + 0.00389\text{nK}^{-1} \cdot T. \tag{6.6}$$

which allows us now to compare the critical temperature $T_c = (127 \pm 9)$nK relative to the local Fermi temperature. This leads to

$$\frac{T_c}{T_F} = \frac{(127 \pm 9)\text{nK}}{438\text{nK}} = 0.29\ (3)\ (1)\ (stat.)^1\ (sys.)^2. \tag{6.7}$$

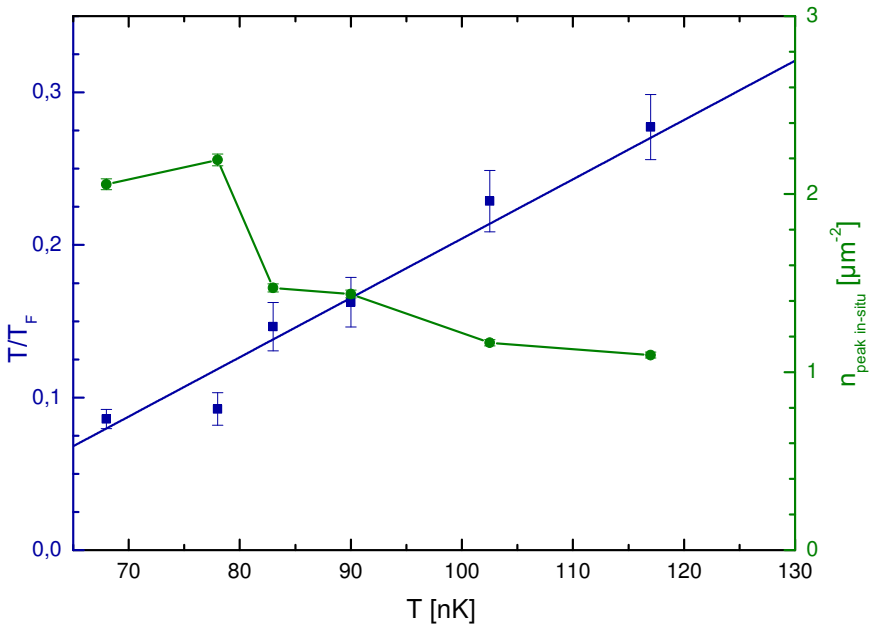

Figure 6.10.: **Temperature dependence of the in-situ peak density and calculated $\mathbf{T/T_F}$ for different temperatures of the cloud.** Green depicts the measured total in-situ peak density $n_{0,692}$ as a function of temperature. The errors corresponds to a reading error of about 1.5%. From this densities we determined the dimensionless parameter T/T_F where we estimated the error from the statistical error of the absolute temperature T. The data was further linear interpolated to the regime of our critical temperature T_c.

To compare our T_c/T_F[8] to the theoretically predicted values, we have to calculate first in which regime of interactions we probe the system. Therefore we calculate the interaction parameter $\ln(k_F a_{2D})$ at T_c with $k_F = \sqrt{\frac{2k_B T_F m}{\hbar^2}}$. This leads in case of the dimer mass to $k_{F,dimer} = 4.7\mu\text{m}^{-1}$ and for an atomic system to $k_{F,atomic} = 3.3\mu\text{m}^{-1}$ at 692G. Since the 2d scattering length $a_{2D} = 7.73 \cdot 10^{-2}\mu\text{m}$ corresponds to an atomic system we will use $k_{F,atomic}$ in the following calculation and obtain $\ln(k_F a_{2D}) \approx -1.37 \pm 0.03$[9].

[1]Statistical error was estimated from the 8% statistical error of T_c and 8% error of c due to the shot-to-shot fluctuation of the in-situ densities.

[2]Systematical error was estimated from the 5% error of the Fermi energy $E_F \sim \sqrt{N}$ due to the 10% uncertainty of the atom number in the regime $E_F \approx \hbar\omega_z$ and the assumption $E_{F,900} \approx E_{F,1400}$. Further we took into account a reading error of about 1.5%.

[8]Since we are in the bosonic regime T_F is used here as a label for the density n to make T/T_F a dimensionless quantity.

[9]Error was estimated by the systematical error of T_F.

Hence, we are close to the strongly interacting regime $|\ln(k_F a_{2D})| < 1$.
From a theoretical analysis of the weakly interacting Bose gas in 2d in the regime $\ln(k_F a_{2D}) < 0$ a critical temperature of the BKT-transition of $T_c/T_F \leq 0.12$ was determined using Monte Carlo data [Pet03]. The determined value of $T_c/T_F = 0.29$ deviates from the theoretical calculations due to the strong density dependence of T_F. Since the crossover between the weakly interacting regime and the strongly interacting regime in 2d is a field of current research in both theoretical and experimental physics, the exact BKT-transition temperature remains still an open question [Bau13].
We further rescaled the plot of the quasi-condensate fraction due to the linear connection to T/T_F. Thus, we obtained the dependence of the quasi-condensate fraction on the dimensionless quantity T/T_F which is plotted in Figure 6.11.

To summarize, we presented in this chapter the first measurements investigating a

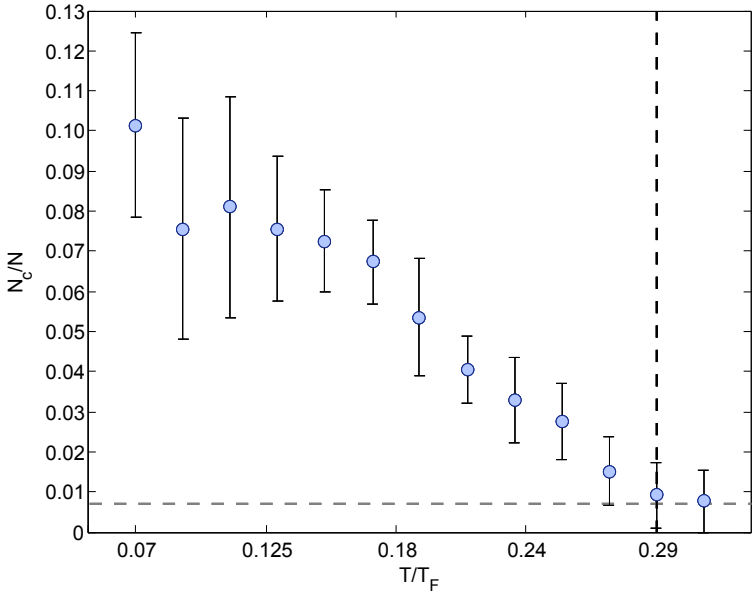

Figure 6.11.: **Quasi-condensate fraction $\mathbf{N_c/N}$ as a function of $\mathbf{T/T_F}$.** Due to the fact that T_F is a function of density n we rescaled the data from Figure 6.9.

strongly interacting quasi-2d Bose gas. We observed a separation of a normal and a quasi-condensed part in the density distribution and an enhanced occupation of low momentum states in the momentum distribution. Further we successfully probed a phase transition in the quasi-2d system. Due to the measured density fluctuations leading to a quasi long range order in the quasi-condensed part and the determined critical temperature T_c/T_F from the in-situ momentum distribution, we achieved significant evidences, that this phase transition corresponds in fact to the BKT-transition predicted in two dimensional quantum systems.

7. Conclusion and Outlook

Conclusion

In this thesis we successfully studied the phase transition from a normal gas phase to a condensed phase in a strongly interacting Bose gas in a quasi-2d environment. We obtained strong indications for the occurrence of a topological phase transition as predicted by the Berezinskii-Kosterlitz-Thouless (BKT) theory. For this we have succeeded in preparing and controlling the interaction strength of a two component Fermi gas in the 2d analogue of the 3d BEC-BCS crossover regime.
This was realized by using an already implemented standing wave optical dipole trap to produce a stack of highly anisotropic pancake shaped potentials. We prepared a BEC of Feshbach molecules in a crossed beam 3d optical dipole trap by evaporative cooling and transferred the molecular BEC directly from the 3d trap into the standing wave potentials. To probe the density distribution of the transferred particles in the several pancake potentials we applied a tomographic rf-spectroscopy technique. In the course of this thesis the resolution of this technique was further improved by implementing a larger magnetic field gradient of 72G/cm. In addition we obtained a long term stability of the magnetic offset field of 1mG, which enabled us to resolve the density distribution of the particles trapped in each pancake potential. Due to this achievements we realized to load a molecular BEC into only a single layer of the standing wave optical dipole trap.
Because of the high anisotropy of the trapping potential, with a large spacing of the energy levels along the vertical axis, we are able to 'freeze out' one motional degree of freedom. Therefore we set the Fermi energy of the sample $E_F \ll \hbar\omega_z$ by choosing a sufficiently small particle number and reduce the temperature $k_B T \ll \hbar\omega_z$. We optimized the cooling of the sample in the 3d trap by implementing quadratic evaporation ramps and minimized the intensity noise of the trapping beams. Furthermore we managed to precisely control the particle number in the 2d trap by spilling the particles out of the trap using a magnetic field gradient. By probing the Gaussian width of a weakly interacting Fermi gas in the direction of tight confinement after time-of-flight, we successfully determined the critical Fermi energy to enter the 2d regime.
We further noticed that during the absorption imaging process the imaged particles get Doppler shifted due to the recoil of a multiple of absorbed and randomly scattered photons. This leads to an underestimation of our detected atom number by a factor of 1.3. We compensated this shift by modulating directly the current of the imaging laser diode with a linear ramp to shift the frequency of the imaging laser during the absorption imaging pulse by approximately one linewidth. Since our imaging beam

intensity is on the order of the saturation intensity of the transition, we underestimate the number of particles when using the analysis for $I << I_{sat}$. We estimated experimentally a correction factor of 1.7 to correctly determine the particle number.
Investigating the quasi-2d sample in the bosonic limit of strong interactions by a time-of-flight measurement, we observed a clear bimodal density distribution with random density fluctuations in the quasi-condensed part. This was the first indication of observing a phase transition in a quasi-2d regime. We quantified the fluctuations by a density-density correlation function and related them to the existence of a quasi long range order in the quasi-condensate. To investigate the phase transition systematically we heated the trapped molecules and observed a decrease of the oscillatory behavior in the correlation function. Yet, a quantitative study of this behavior could not be obtained since the measured density-density correlation functions were correlated with the detuning of our imaging laser.
Another indication of quasi-long range order and a topological phase transition is the algebraic decay of the first order correlation function, which becomes accessible via the in-situ momentum distribution of the sample. We developed a method to map the in-situ momentum distribution of the quasi-2d sample onto the density distribution by using a matter wave focusing technique and observed a significant occupation of low momentum states which is a clear signature of degeneration in the cloud. From a Boltzmann fit to the high momentum wings of the momentum distribution we determined the temperature of the sample. Furthermore, we observed a significant decrease of the low momentum occupation of the quasi-condensed molecules while heating the sample. This disappearance of the quasi-condensate part is a strong indication of a phase transition in the system. We accomplished to estimate the critical temperature of the phase transition at 692G to be about $T_c/T_F = 0.29\ (3)\ (1)$ (stat.) (sys.) which deviates from the theoretical prediction. Since the difference between a transition to a BKT-phase and the transition to a BEC-phase is subtle, it is hard to clearly identify the regime we probe. However, the observation of density fluctuations in the quasi-condensate part is a strong indication that we have actually observed a BKT phase transition in a strongly interacting Bose gas.

Outlook

To clarify the nature of the phase transition quantitatively we want to characterize the decay of the momentum distribution at low momenta. From the critical exponent of this decay, the exponent of the algebraic decaying first order correlation function could be obtained. In the near future we plan to extend our investigations to the 2d analogue of the BEC-BCS crossover region. Using a rapid ramp technique to minimize the effect of strong interactions during the release of the atoms and optimizing the matter wave focusing technique to image the in-situ momentum distribution will allow to study the BKT phase transition in the BEC-BCS crossover. This will provide an important insight into the pairing mechanism of fermions in both the weakly interacting regime

$\ln(k_F a_{2D}) \to \pm\infty$ and the strongly interacting regime $|\ln(k_F a_{2D})| \ll 1$. A quantitative measurement of the critical temperature T_c/T_F for different magnetic offset fields will further allow to measure the phase diagram of a two component Fermi gas in 2d, which is so far only partially described by theory [Pet03, Bau13].
Moreover we plan to set up a simple square optical lattice to study the physics of systems described by the Fermi-Hubbard Hamiltonian. Therefore two additional lattice beams have already been implemented in the setup. Figure 7.1 a) shows a first impression of the effect of this 2d lattice on the atoms. Here we released a molecular BEC from the 3d trap and then switched on the lattice beams for a short time. The expanding cloud gets diffracted of the optical lattice potential which leads to the depicted density distribution. After implementing the lattice we plan to investigate the quantum phase transition between a superfluid and a fermionic Mott-insulator state by loading a two component Fermi gas into the optical lattice potential.

Furthermore, we plan to implement a new objective in the up-down imaging axis

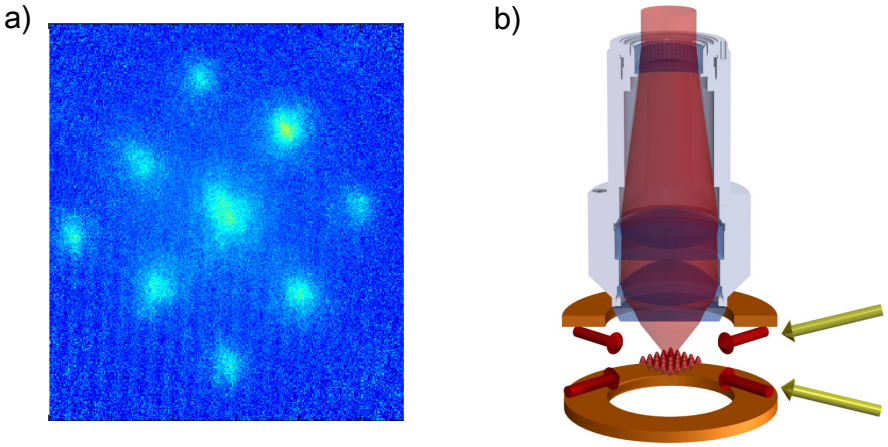

Figure 7.1.: **Kapitza-Dirac scattering of a 2d optical lattice and a schematic view of the high resolution objective.** a) shows a released mBEC which scattered on the optical potential provided by two lattice beams. The symmetric pattern of this so-called Kapitza-Dirac scattering shows, that the lattice beams are well aligned with respect to each other. Further details of the scattering procedure can be found in [Nei13, Bec13]. b) depicts the high resolution objective placed above the Feshbach coils. It was calibrated for two wavelength and built during a Bachelor thesis in our group [Kri13]. The pictures are taken from [Bec13] and [Rie10].

with a high numerical aperture and a small working distance depicted in Figure 7.1 b). Due to the fact that the objective has been designed for $\lambda = 671$nm imaging light and $\lambda = 1064$nm trapping light we want to use this objective in combination with a spatial light modulator to create arbitrary 2d optical potentials at the position of the 2d sample. Together with the increased resolution of the objective (1.08μm for $\lambda = 671$nm

and 0.68μm for $\lambda = 1064$nm) we should be able to achieve single site resolution of our lattice.

A. Appendix

A.1. Dispersion of a Gaussian wave packet

We start with a general ansatz for the wave function:

$$\Psi(x,0) = A \cdot \exp\left(-\frac{x^2}{2\sigma^2}\right) \exp\left(\frac{ip_0 x}{\hbar}\right), \tag{A.1}$$

where p_0 corresponds to the momentum. From the normalization condition we can calculate A

$$1 \stackrel{!}{=} \int |\Psi(x,0)|^2 dx = \int A^2 \exp\left(-\frac{x^2}{\sigma^2}\right) dx = A^2\sqrt{\pi}\sigma, \tag{A.2}$$

here we substituted $a = x/\sigma$ and $da = dx/\sigma$ and obtain $A = \frac{1}{\sqrt[4]{\pi}\sqrt{\sigma}}$ from $\int \exp(-\alpha x^2)dx = \frac{\sqrt{\pi}}{\alpha}$ for $\alpha > 0$.

Further it is useful to calculate the variance $(\Delta x)^2 = \langle \hat{x}^2 \rangle - \langle \hat{x} \rangle^2$. Therefore we need

$$\langle \hat{x} \rangle = \int x |\Psi(x,0)|^2 dx = 0, \tag{A.3}$$

where we used $\int x \exp(-a(x-b)^2)dx = b\frac{\sqrt{\pi}}{a}$ for $a > 0$ and

$$\langle \hat{x}^2 \rangle = \int x^2 |\Psi(x,0)|^2 dx = A^2 \int x^2 \exp\left(-\frac{x^2}{\sigma^2}\right) dx.$$

By substituting $a = x/\sigma$ and use $\int x^2 \exp(-ax^2)dx = \frac{1}{2}\sqrt{\frac{\pi}{a^3}}$ for $a > 0$ one gets

$$\langle \hat{x}^2 \rangle = \frac{A^2}{2}\sigma^3\sqrt{\pi} = \frac{\sigma^2}{2}. \tag{A.4}$$

Hence the standard deviation is given by $\Delta x = \frac{\sigma}{\sqrt{2}}$. Now we change to the momentum representation by Fourier transforming the wave function.

$$\Psi(p,0) = \frac{1}{\sqrt{2\pi\hbar}} \int \exp\left(-\frac{ipx}{\hbar}\right) \Psi(x,0) dx =$$

$$\frac{1}{\sqrt{2\pi\hbar}} A \int \exp\left(-\frac{x^2}{2\sigma^2}\right) \exp\left(-\frac{i(p_0 - p)x}{\hbar}\right) dx,$$

to solve the integral we use the following relation with $u = x, \alpha = 1/\sigma, y = (p_0 - p)/\hbar$

$$\int \exp\left(-\frac{u^2\alpha^2}{2} + iuy\right) du = \exp\left(-\frac{y^2}{2\alpha^2}\right) \int \exp(x^2)\frac{\sqrt{2}}{\alpha} dx =$$

$$\frac{\sqrt{2\pi}}{\alpha} \exp\left(-\frac{y^2}{2\alpha^2}\right).$$

The wave function in momentum representation is then given by

$$\Psi(p,0) = \frac{\sigma}{\sqrt{\hbar}} A \exp\left(-\frac{(p_0 - p)^2\sigma^2}{2\hbar^2}\right). \tag{A.5}$$

Further holds then

$$|\Psi(p,0)|^2 = \frac{A^2\sigma^2}{\hbar} \exp\left(-\frac{(p - p_0)^2\sigma^2}{\hbar^2}\right) \quad \text{and} \quad \Delta p = \frac{\hbar}{\sqrt{2}\sigma} \tag{A.6}$$

Now we introduce the time evolution by the time evolution operator

$$\Psi(p,t) = \exp\left(-\frac{iE(p)t}{\hbar}\right)\Psi(p,0) \quad \text{and} \quad \Psi(x,t) = \frac{1}{\sqrt{2\pi\hbar}} \int \exp\left(\frac{ipx}{\hbar}\right)\Psi(p,t)dp \tag{A.7}$$

and we obtain

$$\Psi(x,t) = \frac{1}{\sqrt{2\pi\hbar}} \int \exp\left(\frac{i(px - E(p)t)}{\hbar}\right)\Psi(p,0)dp =$$

$$\frac{\sigma A}{\sqrt{2\pi\hbar\sqrt{\hbar}}} \int \exp\left(\frac{i(px - E(p)t)}{\hbar}\right) \exp\left(-\frac{(p_0 - p)^2\sigma^2}{2\hbar^2}\right) dp,$$

by substituting $p' = p - p_0$ we can write the first exponent as

$$px - E(p)t = (p' + p_0)x - \frac{1}{2m}(p' + p_0)^2 t = -p'^2\frac{t}{2m} + p'\left(x - \frac{p_0 t}{m}\right) + p_0 x - E(p_0)t.$$

By separating the terms in powers of p' and one gets

$$\Psi(x,t) = \frac{\sigma A}{\sqrt{2\pi\hbar\sqrt{\hbar}}} \exp\left(\frac{i(p_0 x - E(p_0)t)}{\hbar}\right) \int \exp\left(-\frac{p'^2}{2\hbar^2}\left(\frac{it\hbar}{m} + \sigma^2\right) + \frac{ip'}{\hbar}\left(x - \frac{p_0 t}{m}\right)\right) dp'.$$

By defining the constant as C and the first exponential as D and further substitution $k = p'/\hbar$ and $\beta = 1 + i\frac{\hbar t}{m\sigma^2}$ the integral reduces to

$$C \cdot D \int \exp\left(-\frac{k^2\sigma^2\beta}{2} + ik\left(x - \frac{p_0 t}{m}\right)\right) dk$$

which can be solved with a last substitution $u = k, \alpha = \sigma\sqrt{\beta}$ and $y = \left(x - \frac{p_0 t}{m}\right)$ leading to

$$\Psi(x,t) = \frac{A}{\sqrt{\beta}} \exp\left(\frac{i(p_0 x - E(p_0)t)}{\hbar}\right) \exp\left(-\left(x - \frac{p_0 t}{m}\right)^2 \frac{1}{2\sigma^2\beta}\right) \tag{A.8}$$

Now we have to calculate the probability $|\Psi(x,t)|^2 = \Psi^*(x,t)\Psi(x,t)$ which can be obtained by introducing $z = \exp(-r/\beta)$ with r is real and β a complex number. From this follows

$$|z|^2 = z^* z = \exp(-r/\beta^*)\exp(-r/\beta) = \exp\left(-r\left(\frac{\beta + \beta^*}{\beta^*\beta}\right)\right) = \exp\left(-r\left(\frac{2\,\mathrm{Re}\,\beta}{|\beta|^2}\right)\right).$$

Applied to the latter exponential leads to

$$|\Psi(x,t)|^2 = \frac{A^2}{\sqrt{\beta^*\beta}} \exp\left(-\left(x - \frac{p_0 t}{m}\right)^2 \frac{1}{2\sigma^2}\left(\frac{2\,\mathrm{Re}\,\beta}{|\beta|^2}\right)\right),$$

and since $|\beta|^2 = 1 + \frac{\hbar^2 t^2}{m^2\sigma^4}$ and $\mathrm{Re}\,\beta = 1$ one finally obtains

$$|\Psi(x,t)|^2 = \frac{1}{\sqrt{\pi}\sigma|\beta|} \exp\left(-\left(x - \frac{p_0 t}{m}\right)^2 \frac{1}{\sigma^2|\beta|^2}\right). \tag{A.9}$$

If one compares the exponents with $|\Psi(x,0)|^2 = A^2 \exp\left(-\frac{x^2}{\sigma^2}\right)$ the following scaling can be obtained

$$x \to x - \frac{p_0 t}{m} \quad \text{and} \quad \sigma = \sigma|\beta|, \tag{A.10}$$

with $|\beta| = \sqrt{1 + \left(\frac{\hbar t}{m\sigma^2}\right)^2}$. Thus, the probability density is now centered around $\langle x \rangle = \frac{p_0 t}{m}$ and the width is given by

$$\Delta x\beta = \frac{\sigma}{\sqrt{2}}\sqrt{1 + \left(\frac{\hbar t}{m\sigma^2}\right)^2}, \tag{A.11}$$

The relation between the σ_{Gfit} we obtain from the Gaussian distribution fit is $2\sigma_{Gfit}^2 = (\sigma\beta)^2$ and thus $\sigma_{Gfit} = \Delta x\beta$. In our case we use the Gaussian ground state of the quantum harmonic oscillator given by

$$\Psi(x,0) = \left(\frac{m\omega}{\pi\hbar}\right)^{1/4} \exp\left(-\frac{x^2}{2a_{ho}}\right), \tag{A.12}$$

with the harmonic oscillator length $a_{ho} = \sqrt{\frac{\hbar}{m\omega}}$ and $\omega = \omega_z$. Since we are just interested in the scaling of $\sigma = a_{ho}$ we can follow if $\Psi(x,0) \to \Psi(x,t)$ then $a_{ho} \to a_{ho}|\beta|$ and we

achieve the relation given in Section 5.5

$$\Delta x\beta = \sqrt{\frac{\hbar}{2m}\left(\frac{1}{\omega_z} + \omega_z t^2\right)} = \sigma_{Gfit} \tag{A.13}$$

A.2. Radially averaged momentum distribution for all temperatures at 692G

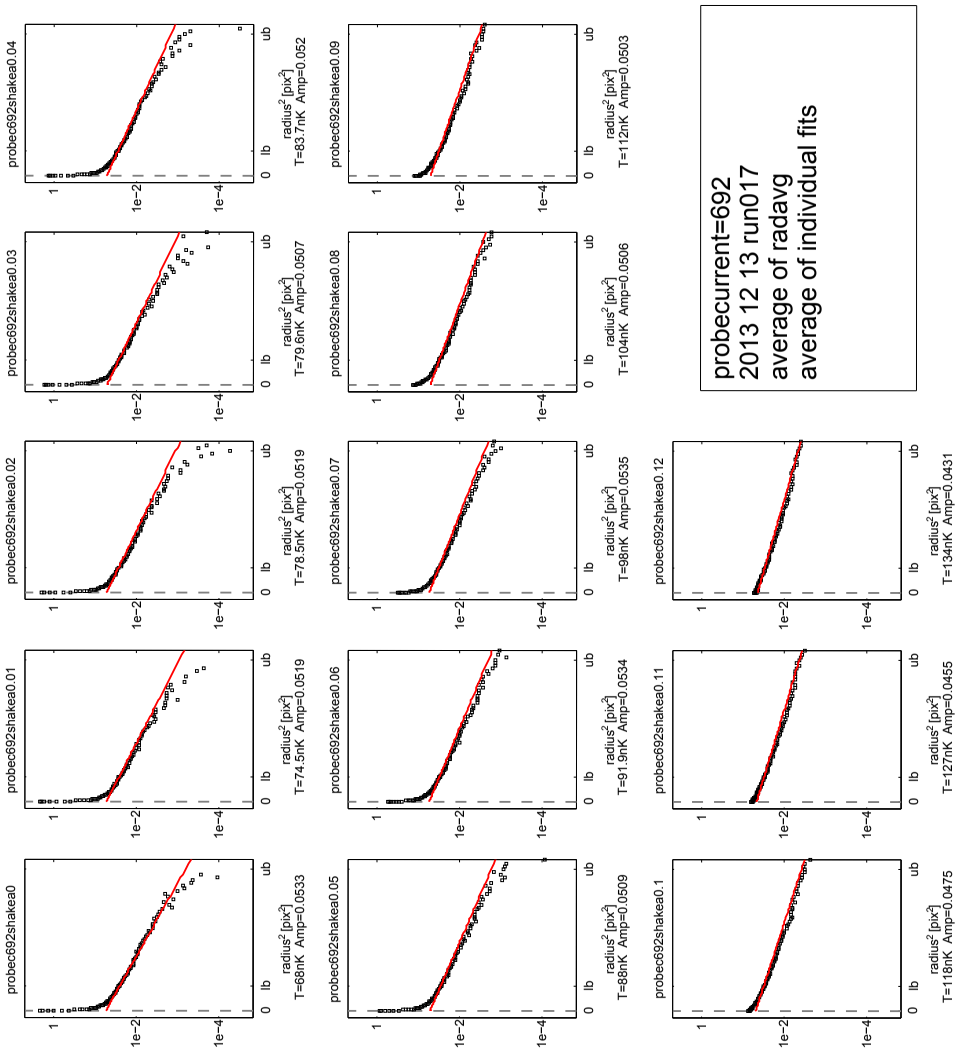

Figure A.1.: **Radially averaged momentum distribution in semi-logarithmic representation.** Here we plotted the averaged radial averages and the average of the individual Maxwell-Boltzmann fits.

Bibliography

[Adh86] S. K. Adhikari, *Quantum scattering in two dimensions*, Am. J. Phys. **54**, 362 (1986).

[And95] M. H. Anderson, J. R. Ensher, M. R. Matthews, C. E. Wieman, E. A. Cornell, *Observation of Bose-Einstein Condensation in a Dilute Atomic Vapor*, Science **269**, 198–201 (1995).

[Bar57] J. Bardeen, L. N. Cooper, J. R. Schrieffer, *Theory of Superconductivity*, Phys. Rev. **108**, 1175–1204 (1957).

[Bar05] M. Bartenstein, A. Altmeyer, S. Riedl, R. Geursen, S. Jochim, C. Chin, J. H. Denschlag, R. Grimm, A. Simoni, E. Tiesinga, C. J. Williams, P. S. Julienne, *Precise Determination of* ^{6}Li *Cold Collision Parameters by Radio-Frequency Spectroscopy on Weakly Bound Molecules*, Phys. Rev. Lett. **94**, 103201 (2005).

[Bau13] M. Bauer, M. Parish, T. Enss, *Universal equation of state and pseudogap in the two dimensional Fermi gas*, arXiv 1311.1000 (2013).

[Bec13] J. Becher, *A two dimensional optical lattice for ultracold fermions* (2013), Bachelor thesis, Ruprecht-Karls-Universität Heidelberg.

[Ber71] V. L. Berezinskii, *Destruction of long-range order in one-dimensional and two-dimensional systems possessing a continuous symmetry group. II. Quantum systems*, Sov. Phys. JETP **34**, 610 (1971).

[Ber13] A. Bergschneider, *Ultracold few-fermion systems in multiwell potentials*, Masters Thesis, Department of Physics and Astronomy, University of Heidelberg (2013), Master thesis, Ruprecht-Karls-Universität Heidelberg.

[Bis78] D. J. Bishop, J. D. Reppy, *Study of the Superfluid Transition in Two-Dimensional* ^{4}He *Films*, Phys. Rev. Lett. **40**, 1727–1730 (1978).

[Blo75] P. Bloom, *Two-dimensional Fermi gas*, Phys. Rev. B **12**, 125–129 (1975).

[Blo08] I. Bloch, J. Dalibard, W. Zwerger, *Many-body physics with ultracold gases*, Rev. Mod. Phys. **80**, 885 (2008).

[Bog60] N. N. Bogoliubov, Physica **26**, S1 (1960).

[Boh12] J. E. Bohn, *Towards an ultracold three-component Fermi Gas in a two-dimensional optical lattice* (2012), Diploma thesis, Ruprecht-Karls-Universität Heidelberg.

[Bon64] A. Bondi, *van der Waals Volumes and Radii*, J. Phys. Chem. **68**, 441–451 (1964).

[Bra03] B. Bransden, C. J. Joachain, *Physics of atoms and molecules* (Pearson Education, 2003).

[Bre31] G. Breit, I. I. Rabi, *Measurement of Nuclear Spin*, Phys. Rev. **38**, 2082–2083 (1931).

[Bro23] L. de Broglie, *Waves and Quanta*, Nature (London) **112**, 540 (1923).

[CCT11] D.-O. Claude Cohen-Tannoudji, *Advances in Atomic Physics* (World Scientific, 2011).

[Chi05] C. Chin, P. S. Julienne, *Radio-frequency transitions on weakly bound ultracold molecules*, Phys. Rev. A **71**, 012713 (2005).

[Chi10] C. Chin, R. Grimm, P. Julienne, E. Tiesinga, *Feshbach resonances in ultracold gases*, Rev. Mod. Phys. **82**(2), 1225 (2010).

[Cho13] J.-y. Choi, S. W. Seo, Y.-i. Shin, *Observation of Thermally Activated Vortex Pairs in a Quasi-2D Bose Gas*, Phys. Rev. Lett. **110**, 175302 (2013).

[Dal98] J. Dalibard, *Collisional dynamics of ultracold atomic gases*, in M. Inguscio, S. Stringari, C. Wieman (Ed.), *Bose-Einstein Condensation in Atomic Gases*, Vol. Course CXL of *Proceedings of the International School of Physics Enrico Fermi* (IOS Press, Varenna, 1998).

[Dal99] F. Dalfovo, S. Giorgini, L. P. Pitaevskii, S. Stringari, *Theory of Bose-Einstein condensation in trapped gases*, Rev. Mod. Phys. **71**(3), 463–512 (1999).

[Dav95] K. B. Davis, M.-O. Mewes, M. R. Andrews, N. J. van Druten, D. S. Durfee, D. M. Kurn, W. Ketterle, *Bose-Einstein condensation in a gas of sodium atoms*, Phys. Rev. Lett. **75**(22), 3969–3973 (1995).

[DeM99] B. DeMarco, D. S. Jin, *Onset of Fermi Degeneracy in a Trapped Atomic Gas*, Science **285**, 1703–1706 (1999).

[Des12] R. Desbuquois, L. Chomaz, T. Yefsah, J. Leonard, J. Beugnon, C. Weitenberg, J. Dalibard, *Superfluid behaviour of a two-dimensional Bose gas*, Nat Phys **8**(9), 645 (2012).

[Don01] E. Donley, N. Claussen, S. Cornish, J. Roberts, E. Cornell, C. Wieman, *Dynamics of collapsing and exploding Bose-Einstein condensates*, Nature **412**, 295–299 (2001).

[Dyk10] P. Dyke, *Quasi Two-Dimensional* ^{6}Li *Fermi gas*, Dissertation, Faculty of Engineering and Industrial Sciences Swinburne University of Technology Melbourne, Australia (2010).

[Dyk11] P. Dyke, E. D. Kuhnle, S. Whitlock, H. Hu, M. Mark, S. Hoinka, M. Lingham, P. Hannaford, C. J. Vale, *Crossover from 2D to 3D in a Weakly Interacting Fermi Gas*, Phys. Rev. Lett. **106**, 105304 (2011).

[Fel11] M. Feld, B. Fröhlich, E. Vogt, M. Koschorreck, M. Köhl, *Observation of a pairing pseudogap in a two-dimensional Fermi gas*, Nature **480**, 75 (2011).

[Fes58] H. Feshbach, *Unified theory of nuclear reactions*, Annals of Physics **5**(4), 357 – 390 (1958).

[Fis88] D. S. Fisher, P. C. Hohenberg, *Dilute Bose gas in two dimensions*, Phys. Rev. B **37**, 4936–4943 (1988).

[Frö11a] B. Fröhlich, *A Strongly Interacting Two-Dimensional Fermi Gas*, Dissertation, St Catharine's College, University of Cambridge (July 2011).

[Frö11b] B. Fröhlich, M. Feld, E. Vogt, M. Koschorreck, W. Zwerger, M. Köhl, *Radio-Frequency Spectroscopy of a Strongly Interacting Two-Dimensional Fermi Gas*, Phys. Rev. Lett. **106**, 105301 (2011).

[Frö12] B. Fröhlich, M. Feld, E. Vogt, M. Koschorreck, M. Köhl, C. Berthod, T. Giamarchi, *Two-Dimensional Fermi Liquid with Attractive Interactions*, Phys. Rev. Lett. **109**, 130403 (2012).

[Fuc09] J. Fuchs, *Molecular Bose-Einstein Condensates and p-wave Feshbach Molecules of* $^6Li_2$, Dissertation, Centre for Atom Optics and Ultrafast Spectroscopy and ARC Centre of Excellence for Quantum-Atom Optics Swinburne University of Technology, Melbourne (2009).

[Geh03] M. Gehm, *Properties of* 6*Li* (2003), http://www.physics.ncsu.edu/jet/ tech-docs/pdf/PropertiesOfLi.pdf.

[Gio08] S. Giorgini, L. P. Pitaevskii, S. Stringari, *Theory of ultracold atomic Fermi gases*, Rev. Mod. Phys. **80**, 1215–1274 (Oct 2008).

[Gre03] M. Greiner, C. A. Regal, D. S. Jin, *Emergence of a molecular Bose-Einstein condensate from a Fermi gas*, Nature **426**(6966), 537 (2003).

[Gri00] Rudolf Grimm, Matthias Weidemüller, Yurii B. Ovchinnikov, *Optical dipole traps for neutral atoms*, Adv. At. Mol. Opt. Phys. **Vol. 42**, 95–170 (2000).

[Gro61] E. Gross, *Structure of a quantized vortex in boson systems*, Nuovo Cimento **20**, 454 (1961).

[Had06] Z. Hadzibabic, P. Krüger, M. Cheneau, B. Battelier, J. Dalibard, *Berezinskii-Kosterlitz-Thouless crossover in a trapped atomic gas*, Nature **441**, 1118 (2006).

[Had11] Z. Hadzibabic, J. Dalibard, *Two-dimensional Bose fluids: An atomic physics perspective*, Rivista del Nuovo Cimento, vol. **34,**, pp.389–434 (2011).

[Hoh67] P. C. Hohenberg, *Existence of Long-Range Order in One and Two Dimensions*, Phys. Rev. **158**, 383 (1967).

[Hol08] M. Holzmann, M. Chevallier, W. Krauth, *Semiclassical theory of the quasi-two-dimensional trapped Bose gas*, EPL **82**, 30001 (2008).

[Hol10] M. Holzmann, M. Chevallier, W. Krauth, *Universal correlations and coherence in quasi-two-dimensional trapped Bose gases*, Phys. Rev. A **81**, 043622 (2010).

[Ino98] S. Inouye, M. R. Andrews, J. Stenger, H.-J. Miesner, D. M. Stamper Kurn, W. Ketterle, *Observation of Feshbach resonances in a Bose-Einstein condensate*, Nature **392**, 151–154 (1998).

[Jac75] J. Jackson, *Classical electrodynamics* (Wiley, 1975).

[Joc03] S. Jochim, M. Bartenstein, A. Altmeyer, G. Hendl, S. Riedl, C. Chin, J. Hecker Denschlag, R. Grimm, *Bose-Einstein Condensation of Molecules*, Science **302**(5653), 2101–2103 (2003).

[Joc04] S. Jochim, *Bose-Einstein Condensation of Molecules*, Dissertation, Leopold-Franzens-Universität Innsbruck (2004).

[Ket99] W. Ketterle, D. S. Durfee, D. M. Stamper Kurn, *Making, probing and understanding Bose-Einstein condensates*, in M. Inguscio, S. Stringari, C. Wieman (Ed.), *Bose-Einstein Condensation in Atomic Gases*, Vol. CXL of *Proceedings of the International School of Physics Enrico Fermi*, 67–176 (IOS Press, Amsterdam, 1999).

[Ket08] W. Ketterle, M. W. Zwierlein, *Proc. of the International School of Physics 'Enrico Fermi', Course CLXIV: Making, probing and understanding ultracold fermi gases* (2008).

[Kos73] J. M. Kosterlitz, D. J. Thouless, *Ordering, metastability and phase transitions in two-dimensional systems*, Journal of Physics C: Solid State Physics **6**(7), 1181 (1973).

[Kri13] S. Krippendorf, *An optical setup for high-resolution imaging and manipulating of ultracold atoms* (2013).

[Lan81] L. Landau, E. Lifshitz, *Quantum Mechanics: Non-Relativistic Theory*, Vol. 3 (Elsevier Science, 1981).

[Lom11] Thomas Lompe, *Efimov Physics in a three-component Fermi gas*, Dissertation, Ruprecht-Karls-Universität Heidelberg, http://www.mpi-hd.mpg.de/biblio/preprints/2011-023.pdf (2011).

[Mer66] N. D. Mermin, H. Wagner, *Absence of Ferromagnetism or Antiferromagnetism in One- or Two-Dimensional Isotropic Heisenberg Models*, Phys. Rev. Lett. **17**, 113 (1966).

[Met99] H. J. Metcalf, P. van der Straten, *Laser Cooling and Trapping* (Springer-Verlag, New York, 1999).

[Min87] P. Minnhagen, *The two-dimensional Coulomb gas, vortex unbinding, and superfluid-superconducting films*, Rev. Mod. Phys. **59**, 1001–1066 (1987).

[Moe95] A. J. Moerdijk, B. J. Verhaar, A. Axelsson, *Resonances in ultracold collisions of* ^{6}Li, ^{7}Li, *and* ^{23}Na, Phys. Rev. A **51**, 4852–4861 (1995).

[Nei13] M. Neidig, *A realization of a two-dimensional Fermi gas in a standing wave trap*, Masters Thesis, Department of Physics and Astronomy, University Heidelberg (2013).

[Nel77] D. R. Nelson, J. M. Kosterlitz, *Universal Jump in the Superfluid Density of Two Dimensional Superfluids*, Phys. Rev. Lett. **39**, 1201 (1977).

[Ott10] T. B. Ottenstein, *Few-body physics in ultracold Fermi gases*, Dissertation, Ruprecht-Karls-Universität Heidelberg, http://www.mpi-hd.mpg.de/biblio/preprints/2010-001.pdf (2010).

[Pau25] W. Pauli, *Über den Zusammenhang des Abschlusses der Elektronengruppen im Atom mit der Komplexstruktur der Spektren*, Zeitschrift für Physik **31**(1), 765–783 (1925).

[Pen56] O. Penrose, L. Onsager, *Bose-Einstein Condensation and Liquid Helium*, Phys. Rev. Lett. **104**, 576–584 (1956).

[Pet01] D. S. Petrov, G. V. Shlyapnikov, *Interatomic collisions in a tightly confined Bose gas*, Phys. Rev. A **64**(1), 012706–14 (2001).

[Pet02] C. J. Pethick, H. Smith, *Bose-Einstein Condensation in Dilute Gases* (Cambridge University Press, 2002).

[Pet03] D. S. Petrov, M. A. Baranov, G. V. Shlyapnikov, *Superfluid transition in quasi-two-dimensional Fermi gases*, Phys. Rev. A **67** (2003).

[Pet04a] D. Petrov, D. Gangardt, G. Shlyapnikov, *Low-dimensional trapped gases*, J. Phys. IV **116**, 5–44 (2004).

[Pet04b] D. S. Petrov, C. Salomon, G. V. Shlyapnikov, *Weakly Bound Dimers of Fermionic Atoms*, Phys. Rev. Lett. **93**, 090404 (2004).

[Pet05] D. S. Petrov, C. Salomon, G. V. Shlyapnikov, *Scattering properties of weakly bound dimers of fermionic atoms*, Phys. Rev. A **71**, 012708 (2005).

[Pit61] L. Pitaevskii, *Vortex lines in an imperfect Bose gas*, Sov. Phys. JETP **13**, 451 (1961).

[Pit03] L. Pitaevskii, S. Stringari, *Bose-Einstein Condensation*, International Series of Monographs on Physics - 116 (Oxford University Press, 2003).

[Pro01] N. Prokof'ev, O. Ruebenacker, B. Svistunov, *Critical Point of a Weakly Interacting Two-Dimensional Bose Gas*, Phys. Rev. Lett. **87**, 270402 (2001).

[Pro02] N. Prokof'ev, B. Svistunov, *Two-dimensional weakly interacting Bose gas in the fluctuation region*, Phys. Rev. A **66**, 043608 (2002).

[Rie10] M. G. Ries, *A magneto-optical trap for the preparation of a three-component Fermi gas in an optical lattice* (2010), Diploma thesis, Ruprecht-Karls-Universität Heidelberg.

[Sak94] J. J. Sakurai, *Modern Quantum Mechanics* (Addison-Wesley Publishing Company, Inc., 1994).

[Sal91] B. E. A. Saleh, M. C. Teich, *Fundamentals of photonics* (Wiley, 1991).

[Ser11] F. Serwane, *Deterministic preparation of a tunable few-fermion system*, Dissertation, Ruprecht-Karls-Universität Heidelberg, http://www.mpi-hd.mpg.de/biblio/preprints/2011-048.pdf (2011).

[Sim10] P. Simon, *Apparatus for the preparation of ultracold Fermi gases* (2010), Diploma thesis, Ruprecht-Karls-Universität Heidelberg.

[Sin13] V. Singh, L. Mathey, *Noise correlations of two-dimensional Bose gases*, In preparation (2013).

[Squ11] R. H. Squire, N. H. March, *High-Temperature Superconductivity Mechanism for Cuprates*, arXiv **1111.2560** (2011).

[Vog13] E. Vogt, *Collective Modes and Polarons in two-dimensional Fermi Gases*, Dissertation, Department of Physics, Cavendish Laboratory, University of Cambridge (2013).

[Wei09] M. Weidemüller, C. Zimmermann, *Cold Atoms and Molecules: Concepts, Experiments and Applications to Fundamental Physics* (Wiley-VCH Verlag GmbH & Co, 2009).

[Wen08] A. Wenz, *Few-Body Physics in a Three-Component Fermi Gas*, http://www.mpi-hd.mpg.de/biblio/preprints/2008-023.pdf (2008), Diploma thesis, Ruprecht-Karls-Universität Heidelberg.

[Wen13] A. N. Wenz, *From Few to Many: Ultracold Atoms in Reduced Dimensions*, Dissertation, Combined Faculties of the Natural Sciences and Mathematics of the Ruperto-Carola-University of Heidelberg, Germany (2013).

[Zür12] G. Zürn, *Few-fermion systems in one dimension*, Dissertation, Ruprecht-Karls-Universität Heidelberg (2012).

[Zür13] G. Zürn, T. Lompe, A. N. Wenz, S. Jochim, P. S. Julienne, J. M. Hutson, *Precise Characterization of* ^{6}Li *Feshbach Resonances Using Trap-Sideband-Resolved RF Spectroscopy of Weakly Bound Molecules*, Phys. Rev. Lett. **110**, 135301 (Mar 2013).

[Zwi03] M. W. Zwierlein, C. A. Stan, C. H. Schunck, S. M. F. Raupach, S. Gupta, Z. Hadzibabic, W. Ketterle, *Observation of Bose-Einstein Condensation of Molecules*, Phys. Rev. Lett. **91**, 250401 (Dec 2003).

[Zwi05] M. W. Zwierlein, J. R. Abo Shaeer, A. Schirotzek, C. H. Schunck, W. Ketterle, *Vortices and superfluidity in a strongly interacting Fermi gas*, Nature **435**, 1047–1051 (2005).

[Zwi06] M. W. Zwierlein, *High-Temperature Superfluidity in an Ultracold Fermi Gas*, Dissertation, Massachusetts Institute of Technology (2006).

Danksagung

An dieser Stelle möchte ich mich bei Allen bedanken, die das Gelingen dieser Arbeit erst möglich gemacht haben. Insbesondere möchte ich mich bedanken bei:

- Selim, für die hervorragende Betreuung dieser Arbeit und dafür, dass du mir die Möglichkeit gegeben hast meine Masterarbeit im Bereich Ultrakalter Quantengase zu schreiben. Dein Enthusiasmus und die vielen physikalischen Diskussionen haben mich sehr motiviert.
- der ganzen Arbeitsgruppe vor allem bei Martin, Gerhard, Thomas, Andre, Mathias und Puneet für eure Geduld, die vielen Erklärungen und die Zeit im Labor, die es mir ermöglicht haben das 'Neue' Experiment kennen zu lernen. Vielen Dank auch an das Team vom 'Alten' Experiment Simon, Andrea, Vincent und unseren Gaststudenten Dhruv, für die lustige Zeit, die wir gemeinsam beim After-Lunch-Kickern, Kuchen-essen, Glühwein-trinken, Doktorhut-bauen und Kässpätzle verputzen verbracht haben. Speziellen Dank gilt Martin, Gerhard, Mathias und Puneet, die sich todesmutig der Aufgabe des Korrekturlesens dieser Arbeit gestellt haben.
- den ehemaligen Bachelorstudenten Jan-Hendrik, Sven und Nils, für die Tage in Innsbruck.
- der PI Elektronik-Werkstatt für den Bau der ODA-Box zur Magnetfeldstabilisierung.
- Prof. Markus Oberthaler für die Übernahme der Zweitkorrektur dieser Arbeit.
- Daniel, Lars, Marcus, Peer, Tim und Christoph, für eure Freundschaft und die vielen Stunden, die wir gemeinsam während unseres Studiums verbracht haben.
- meinen Freunden, insbesondere Ruben, Tuncay, Julia, Julian und Barbara.
- meinen Mathe- und Physiklehrern A. Asel und H. Müller, die durch Ihre Persönlichkeit und Ihren Unterricht in mir die Neugier und die Faszination für die Physik geweckt haben.
- meinen Eltern und meiner Schwester für eure unermüdliche Unterstützung während meines Studiums.
- und natürlich meiner Freundin Viktoria einfach nur dafür, dass es Dich gibt, wir uns gefunden haben und Du mir immer zur Seite stehst.

Erklärung

Ich versichere, dass ich diese Arbeit selbstständig verfasst und keine anderen als die angegebenen Quellen und Hilfsmittel benutzt habe.

Heidelberg, den 11.02.2014

.....
(Unterschrift)